Master's thesis

NTNU
Norwegian University of Science and Technology
Faculty of Engineering
Department of Energy and Process Engineering

Johannes Djupesland

Experimental study of the impact of surface waves on turbulent flows

Master's thesis in Mechanical Engineering
Supervisor: Simen Å. Ellingsen
Co-supervisor: Olav Rømcke
June 2023

NTNU
Norwegian University of
Science and Technology

Johannes Djupesland

Experimental study of the impact of surface waves on turbulent flows

Master's thesis in Mechanical Engineering
Supervisor: Simen Å. Ellingsen
Co-supervisor: Olav Rømcke
June 2023

Norwegian University of Science and Technology
Faculty of Engineering
Department of Energy and Process Engineering

NTNU
Norwegian University of
Science and Technology

Abstract

This thesis is an experimental study that investigates the interaction between surface waves and turbulence, and it is a proof-of-concept study to test the possibilities of this sort of experiments in this lab. The research question that is addressed is: "How do surface waves impact turbulence intensity and integral length scale in a shallow, turbulent, open-channel flow?" This is crucial to better understand the vertical turbulent mixing in the upper boundary layer of the ocean and the resulting flux of gas, heat, and momentum between ocean and atmosphere.

The experiments were conducted in a shallow water channel where the turbulence was generated using an active grid and the waves were generated mechanically using a wavemaker. Three different modes of the active gird were designed to generate turbulence with varying intensity and integral length scale. The three modes were spinning, flapping, and static. Instantaneous velocities in streamwise direction were measured by the use of a laser Doppler velocimetry (LDV) system, and the data was used to calculate turbulence properties.

Measurements were done for turbulent flows without waves across the width of the channel, both upstream and downstream, to check that the grid modes yielded appropriate flows to investigate the research question, and to create a benchmark to compare the results with surface waves to. Following from this, measurements were done for turbulent flows with continuous, regular waves, to investigate the research question. The signal from the measurements with waves was decomposed and separated into turbulent and wave motion so that only the turbulent motion was investigated. This was done by the use of empirical mode decomposition (EMD).

The results from the experiments without waves showed that the three grid modes gave differing turbulent flows in terms of turbulence intensity and integral length scale. However, the flapping and static modes gave non-uniform velocity profiles. They were still deemed sufficiently uniform for the purposes of this study. The results downstream also showed that the turbulence intensity had mostly dissipated at that point in the flow, resulting in that the three grid modes were almost identical in terms of intensity here.

The results from the experiments with waves showed a slight increase in turbulence intensity for the static mode, which is in agreement with the literature. However, the small amount of experiments conducted, due to time constraints, and the imperfect separation of the turbulent and wave motion means that the results are too uncertain to really conclude anything from. The answer to the research question was therefore inconclusive, but the study as a proof-of-concept has shown potential for this sort of experiments in the future. Suggestions based on these results were made to improve this experimental setup.

Sammendrag

Denne avhandlingen er en eksperimentell studie som undersøker samspillet mellom overflatebølger og turbulens, og det er en konseptbevis-studie som tester mulighetene for denne typen eksperimenter i dette laboratoriet. Forskningsspørsmålet som blir undersøkt er: "Hvordan påvirker overflatebølger turbulensintensitet og integral lengdeskala i en grunn og turbulent strømning?" Dette er avgjørende for å bedre forstå den vertikale turbulente miksingen i det øvre grensesjiktet i havet og den resulterende transporten av gass, varme og momentum mellom hav og atmosfære.

Eksperimentene ble utført i en grunn vannkanal hvor turbulens ble generert ved bruk av et aktiv gitter, og bølgene ble generert mekanisk ved hjelp av en bølgemaker. Tre forskjellige moduser av det aktive gitteret ble designet for å generere turbulens med varierende intensitet og integral lengdeskala. De tre modusene var en spinne modus, en flappe modus, og en statisk modus. Hastigheter i strømretning ble målt ved hjelp av et laser-Doppler-velocimetry (LDV) system, og dataene ble brukt til å beregne turbulensegenskaper.

Målinger ble utført for turbulente strømmer uten bølger over kanalens bredde, både oppstrøms og nedstrøms, for å sjekke at gittermodusene ga passende strømmer for å undersøke forskningsspørsmålet, og for å skape en referanse for å sammenligne resultatene med overflatebølger. Deretter ble målinger utført for turbulente strømmer med kontinuerlige, regelmessige bølger for å undersøke forskningsspørsmålet. Signalet fra målingene med bølger ble dekomponert og separert til turbulent og bølgebevegelse slik at bare den turbulente bevegelsen ble undersøkt. Dette ble gjort ved hjelp av empirisk modedekomponering (EMD).

Resultatene fra eksperimentene uten bølger viste at de tre gittermodusene ga forskjellige turbulente strømmer når det gjaldt turbulensintensitet og integral lengdeskala. Det ble derimot vist at flappemodusen og den statiske modusen ga ikke-uniforme hastighetsprofiler. De ble likevel vurdert som tilstrekkelig uniforme for formålet med denne studien. Resultatene nedstrøms viste også at turbulensintensiteten hadde dissipert i stor grad på dette punktet i strømmen, noe som resulterte i at de tre gittermodusene var nesten identiske når det gjaldt intensitet her.

Resultatene fra eksperimentene med bølger viste en liten økning i turbulensintensiteten for den statiske modusen, som er i samsvar med litteraturen. Imidlertid betyr det lille antallet eksperimenter som ble utført, på grunn av tidsbegrensninger, og den ufullstendige separasjonen av turbulensen og bølgebevegelsen, at resultatene er for usikre til virkelig å konkludere noe fra dem. Svaret på forskningsspørsmålet var derfor ikke-konkluderende, men studien som en konseptbevis har vist potensial for at denne type eksperimenter kan utføres i denne labben i fremtiden. Forslag basert på disse resultatene er blitt gjort for å forbedre denne eksperimentelle oppsettet.

Acknowledgement

I want to give a special thanks to my supervisor, professor Simen Ådnøy Ellingsen, who facilitated the work in this thesis, and who supported me by giving valuable tips and feedback throughout the year. I would also give a special thanks to postdoctoral Olav Rømcke, who has spent countless hours with me in the lab planning, advising, and helping me set up the experimental setup. His help has been absolutely essential for the completion of the work done in this thesis, and the experiments conducted would have been far more limited without it. The Ellingsen Research Group has also been great support by giving feedback and advise in our biweekly meetings.

A special thanks is also owed to Inger Skundberg Løvvig, a master's student who has been working in the same lab, for great company in the lab, and for being a good discussion partner.

Ultimately, I would thank my friends at the Hydropower lab for making this year as fun as it has been, and my family and other friends for being constant support in my life.

Nomenclature

Acronyms

DFT	Discrete Fourier transform
EMD	Empirical mode decomposition
FFT	Fast Fourier transform
IMF	Intrinsic mode functions
LDV	Laser Doppler velocimetry
PIV	Particle image velocimetry
PSD	Power spectral density
S+H	Sample-and-hold

Dimensionless numbers

Fr	Froude number
Re	Reynolds number
We	Weber number

Symbols

$\bar{\ell}$	Integral length scale	(s)
$\bar{\tau}$	Integral time scale	(s)
$\dot{N}$	Data rate	(s^{-1})
ℓ	Lengthscale of an eddy	(m)
κ	Wavenumber	
$\mathbf{U}$	Velocity field	(ms^{-1})
$\mathcal{L}$	Characteristic length	(m)
$\mathcal{U}$	Characteristic velocity	(ms^{-1})
ν	Kinematic viscosity	(m^2s^{-1})
ω	Angular frequency	
ϕ	Intrinsic mode function	(ms^{-1})
ρ	Autocorrelation function	
τ	Timescale of an eddy	(s)
τ_i	Residence time	(s)

$\tilde{u}$	Wave component	(ms^{-1})
ε	Dissipation rate	$(\mathrm{m}^2\mathrm{s}^{-3})$
E	Energy spectrum function	$(\mathrm{m}^2\mathrm{s}^{-3}$
e	Euler's number	
g	Gravitational acceleration	(ms^{-2})
g_i	Weighting factor	
i	Index value	
k	Turbulent kinetic energy	$(\mathrm{m}^2\mathrm{s}^{-2})$
M	Local maxima	
m	Local minima	
N	Number of samples	
N_B	Number of blocks	
R	Autocovariance function	
r	Displacement in space	(m)
S	Specific surface energy	$(\mathrm{m}^3\mathrm{s}^{-2})$
s	Displacement in time, or time lag	(s)
T	Length of time series	(s)
t	Time	(s)
U	Instant velocity	(ms^{-1})
u	Root mean square of velocity fluctuations	(ms^{-1})
V	Independent velocity variable	(ms^{-1})
w	Width of wing and rod combined	(m)
x	Distance from start of the channel	(m)
Z	Distance between zero crossings	(m)

Superscripts and Subscripts

0	Characteristic scales of the largest eddies
1	Streamwise direction
η	Kolmogorov scales
∞	Free stream
crit	Critical values
DI	Bordering the dissipation range and inertial subrange
EI	Bordering the energy-containing range and inertial subrange
D	Diameter of cylinder as characteristic length
i	Index value
McF	Calculated using method from Mora and Obligado, 2020
x	Streamwise length from start of channel as characteristic length

Contents

Chapter 1

Introduction

This thesis is an experimental study on the interaction between surface waves and turbulent flow in a shallow, open-channel flow. It is a proof-of-concept study to test the possibilities of this sort of experiments in this lab. Therefore, the priority has been to get a functioning set-up and diagnose it rather than fine-tuning the flow.

The research question that will be answered in this thesis is:

How do surface waves impact the turbulence intensity and integral length scale of a shallow, turbulent, open-channel flow?

1.1 Background

1.1.1 Motivation

The turbulence in the upper boundary layer of the ocean plays an important role in the Earth's climate and ecology because it is the vertical turbulent mixing in this layer that ultimately governs the flux of gas, heat, and momentum between the ocean and the atmosphere (D'Asaro, 2014). Getting a better understanding of this turbulence is therefore integral when creating climate and ocean models.

There is a constant triple interaction between surface waves, turbulence, and shear currents in the upper layer of the ocean, and it is these interactions that are driving the turbulent mixing. A closer study of these interactions are therefore needed to get an understanding of the turbulence in the upper layer of the ocean. In this thesis it is the interaction between surface waves and turbulence that is investigated, more specifically, how the surface waves affect parameters of the turbulent flow.

1.1.2 State of the art

Thais and Magnaudet, 1996 carried out experiments in a large laboratory channel to explore the structure of turbulent motion in the water layer beneath surface gravity waves. The experiments involved pure wind waves as well as wind-ruffled mechanically generated waves. They used a two-component LDV system to obtain the three components of the instantaneous velocity field. They also used wave gauges to simultaneously determine the displacement of the free surface at the same location as where they measured the velocities. The most prominent features revealed by the experiments were the enhancement of both the turbulent kinetic energy and its dissipation rate with respect to values found near solid walls. Spectral analysis provided clear indications that wave-turbulence interactions greatly affect energy transfers over a significant frequency range. The

experiments with the mechanical waves showed that the turbulence that was observed was deeply affected at both large and small scales by the wave motion.

Brocchini and Peregrine, 2001, describe the wide range of free-surface deformations that occur when there is turbulence at a free surface. They structure their discussion by consideration of the stabilizing influences of gravity and surface tension against the disrupting effect of the turbulent kinetic energy. This leads to a two-parameter description of the surface behaviour which gives the framework for the two-parameter experimental study conducted in this thesis. Much of their discussion is heuristic and limited by appropriate experimental observations, and it is intended by them that such experiments be stimulated to test their two-parameter description.

Savelsberg and van de Water, 2009, study the free surface of a turbulent flow, in particular the relation between the statistical properties of the wrinkled surface and those of the velocity field beneath. It is an experimental study where they generate turbulence in an open water channel flow by the use of both active and static grid, similar to the experiments in this thesis. They measure the surface gradient field using a laser-scanning device, the velocity field in planes just below the surface using Particle Image Velocimetry (PIV), and properties of the turbulence using a two-component Laser Doppler Velocimetry (LDV). They find that for an irregular flow shed off a vertical cylinder, the surface indentations are strongly correlated with both vortical and strain events in the velocity field. For fully developed turbulence this correlation is dramatically reduced. They conclude that the turbulent surface has dynamics of its own, but that it does inherit both the integral scale, which determines the predominant wavelength of the capillary-gravity surface waves, and the anisotropy from the subsurface turbulence.

Savelyev et al., 2012, investigate the effect of wave motion on the turbulence in close proximity to the surface. Their investigations rely on both experimental and numerical approaches. Turbulent velocities at the water surface were measured in a laboratory wave tank with high precision using the thermal-marking velocimetry technique. Numerically, a fully nonlinear model for the wave motion was coupled with Large Eddy Simulation for the turbulent motion. Their results confirmed the turbulence production due to wave motion. The turbulent kinetic energy was found to be a function of time, wave steepness, wave phase, and initial turbulent conditions. Additionally, the turbulent motion near the surface was found to be horizontally anisotropic due to the formation of near-surface eddies, elongated in the direction of wave propagation.

Guo and L. Shen, 2013, is a numerical study of the effect of surface waves on turbulence underneath. They study cases with various moderate-to-large turbulence-to-wave time ratios and wave steepnesses. The turbulence velocity spectrum shows that the turbulence is dynamically forced by the surface wave.

Tsai et al., 2015, did numerical simulations of monochromatic surface waves propagating over a turbulent field to reveal the mechanism of turbulence production by nonbreaking waves. Their results predicts growth rates of turbulent kinetic energy consistent with previous measurements and modeling. It also validates the observed horizontal anisotropy of the near-surface turbulence that the spanwise turbulent intensity exceeds the streamwise component. Such a flow structure is found to be attributed to the formation of streamwise vortices near the water surface, which also induces elongated surface streaks. The averaged spacing between the streaks and the depth of the vortical cells approximates that of Langmuir turbulence, which arises from the interaction between surface waves and turbulent shear flow. A similar observation to this was made recently by Peruzzi et al., 2021. The strength of the vortices arising from the wave-turbulence interaction is, however, of one order of magnitude less than that of Langmuir cells. The dominant production of turbulent kinetic energy is the advection of turbulence by the velocity straining of waves, in contrast to Langmuir turbulence, where production from the Stokes shear dominates.

1.1.3 Research gap

As shown in subsection 1.1.2, there have been conducted extensive studies on turbulence close to a free surface, and the interaction between surface waves and turbulence. This thesis is contributing to this by being a proof-of-concept-study in generating different types of turbulence, in terms of

turbulence intensity and integral scale, in a shallow water channel. Shallow water channels, like the one used in this thesis, can be used to conduct further studies on wave-turbulence interaction, such as investigating the scattering of waves interacting with turbulence, which is done by Løvvig, 2023.

1.2 Research objectives

To answer the research question of this thesis, certain objectives needs to be set and completed. Experiments without surface waves should be conducted to assure that the channel flow is appropriate, and to set a benchmark to compare the experiments with waves against. Then there should naturally be conducted experiments with surface waves so that the effects of the waves on turbulence intensity and integral length scale can be investigated. After the experiments have been conducted, the data from them needs to be processed appropriately, and the results from the processed data needs to be presented in a way which makes it possible to answer the research question. The research objectives can then be listed as:

1. Conduct experiments with turbulent flows without surface waves.
2. Conduct experiments with turbulent flows with surface waves.
3. Process data from experiments to analyze the impact of surface waves on turbulence.

I will go into further details about each research objective below.

1.2.1 Conduct experiments with turbulent flows without surface waves

As mentioned above, one part of conducting experiments without waves is to see that the flow is appropriate for investigating the wave-turbulence interaction. What it means that the flow is appropriate is that it is *uniform*, *statistically stationary*, and *reproducible*. Considerations are done in the experimental setup, such as implementing a honeycomb grid and putting in smooth sidewalls, to make the flow appropriate. The appropriateness of the flow is checked by doing spanwise measurements to see the uniformity of the flow, doing convergence testing to see that the flow is statistically stationary, and doing multiple similar experiments to see that it is reproducible.

Since we are investigating the surface wave impact on the turbulence intensity and integral length scale, the different turbulent flows generated needs to be clearly different in both parameters from one another. Various modes are designed and tested to ensure this, and the most appropriate modes are selected for the final experiments.

When the flows are appropriate, experiments without waves are conducted to set a benchmark to compare the experiments with waves to. The experiments are done by doing spanwise measurements to get representative values for the flow parameters for the whole span of the channel. This is done both upstream and downstream to see how the flow and flow parameters evolve downstream.

1.2.2 Conduct experiments with turbulent flows with surface waves

To experimentally investigate the wave-turbulence interaction there naturally needs to be conducted experiments of turbulent flows with surface waves. For this to be done, it needs to be decided which type of surface waves that should be investigated, and ensure that these are the only surface waves present during the experiments.

In this thesis it is monochromatic plane waves propagating upstream that is being investigated. A plastic cover has been placed on the water surface right downstream of the active grid to dampen the waves generated by the motion of the active grid, so that they do not interfere with the waves in the experiments.

1.2.3 Process data from experiments

The chosen method for measuring the turbulence in the water channel in this thesis is LDV. LDV is a non interfering way of measuring the velocities in a flow, further explained in section 3.2. The data you get from LDV is the arrival time of particles passing by, their transit time, and one velocity component.

Since the arrival time of the particles passing is random, that means that the LDV-data is not equidistant. Equidistant data is required for doing spectral analysis of the flow, and finding the autocorrelation, which is used to calculate the integral length scale. This means that the data needs to be reconstructed and re-sampled to get some parameters of the turbulent flows.

LDV-data does also contain some bias related to particle-rate/velocity correlation, which is discussed in subsection 3.2.1. This means that to get correct estimations of the statistical moments of the data, a weighting of the data is needed.

For the LDV-data from the experiments with surface waves, the velocity signal contains contribution from the wave motion, as well as from the mean flow and the turbulence. A decomposition of the signal is therefore needed to remove the wave motion, so that the results can be compared with the experiments without waves.

Chapter 2

Theory

This chapter provides the necessary background theory to understand the physical meaning of turbulence intensity and integral length scale, which are the parameters investigated in this thesis. It also provides knowledge on how these parameters are investigated, and why they are important for turbulence interacting with surface waves.

Firstly, a general description of turbulent flows and how they are characterized are given, and there are short descriptions of two of the characteristic flows present in the experiments in this thesis. These descriptions give grounds for discussion in chapter 5. The energy cascade and Kolmogorov's hypotheses are briefly explained to provide insight to how the energy put into the turbulence at integral scale distributes to eddies of smaller scales, and the energy spectrum is introduced as a tool to investigate this. Some theory on how turbulence interacts with a free surface is given, leading to a two-parameter description of the surface behaviour which is the framework of the two-parameter experiments in this thesis. At last a statistical description of turbulence is given to show how the parameters used in this thesis are calculated, and why they are used to describe turbulent flows.

The work in this thesis is a continuation of the work done in Djupesland, 2022, and some of the theory will therefore be similar to the theory in that report.

2.1 Turbulent flows

2.1.1 Nature of turbulence

When looking at turbulent flows in real life, like a waterfall or smoke from a chimney, you can observe that the flow looks irregular and chaotic. From this, Pope, 2000, states that an essential feature of turbulent flows is that the velocity field varies significantly and irregularly in both position and time. In this thesis the velocity field is denoted by $\mathbf{U}(\mathbf{x}, t)$, where $\mathbf{x}$ is position and t is time.

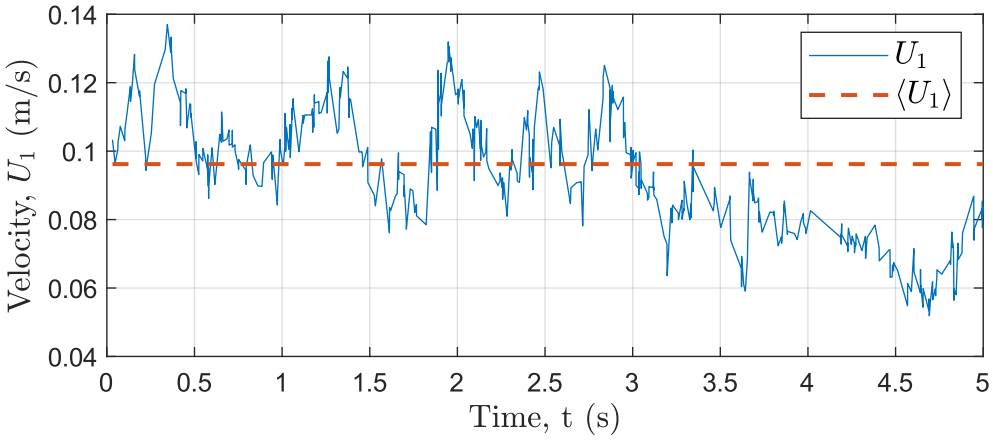

Figure 2.1: The first 5 seconds of one of the turbulent time series from the experiments in this thesis. This time series is from 1st measurement of the flapping mode at 40% pump power, upstream, 3cm left of the center of the channel looking from the active grid. The dashed line is the mean velocity $\langle U_1 \rangle$ calculated using the complete time series. The solid line is the LDV-data.

Figure 2.1 shows the time series for one of the velocity components, U_1, from one of the experiments done in this thesis. U_1 is the streamwise velocity component , and the dashed line shows the mean value of this component, $\langle U_1 \rangle$. The figure shows that the velocity fluctuates significantly from the mean velocity, and the fluctuations are nonperiodic. Pope, 2000, also observes for his example that both U_1 and it's mean $\langle U_1 \rangle$ seems in some sense stable, meaning that there are no huge variations observed, and that U_1 does not spend long periods near values different than $\langle U_1 \rangle$. The same observations can be made for Figure 2.1.

Osborne Reynolds demonstrated with an experiment in 1883, that turbulent flows transport and mix fluid much more effectively than laminar flow (O. Reynolds, 1883). He later established that the flow he was observing, which was flow in a long pipe, was characterized by a single non-dimensional parameter, the Reynolds number Re, (O. Reynolds, 1894). It is the ratio of inertial forces to viscous forces, and is defined as

$$\mathrm{Re} = \frac{\mathcal{U}\mathcal{L}}{\nu} \tag{2.1}$$

where $\mathcal{U}$ is the characteristic velocity of the flow, $\mathcal{L}$ is the characteristic length of the flow, and ν is the kinematic viscosity of the fluid. The Reynolds number is a valid way of characterizing other flows than pipe flow as well, and it will be used in this thesis to characterize types of flows that are present in the experiments.

2.1.2 Boundary layer

All flows have a critical range of the Reynolds number where the flow transitions from laminar to turbulent. This range varies with what type of characteristic flow you are looking at. One of the characteristic flows in the experiments in this thesis is flow over a flat plate, where the Reynolds number is defined as $\mathrm{Re}_x = U_\infty x/\nu$. The characteristic length in this type of flow is the length, x, from the start of the boundary layer, and the characteristic velocity is the free-stream velocity, U_∞, which in this thesis is the mean velocity, $\langle U_1 \rangle$. The critical Reynolds number for this flow is $\mathrm{Re}_{x,crit} \approx 10^5$, (Cengel and Cimbala, 2017). This is when the boundary layer transitions from laminar to turbulent, as seen in Figure 2.2. The kinematic viscosity of water is $\nu \approx 1 \times 10^{-6}\mathrm{m}^2\mathrm{s}^{-1}$ (Rumble et al., 2018), and the mean velocity is $\langle U_1 \rangle = 0.1\mathrm{ms}^{-1}$, as shown in chapter 5. This means that the critical length is $x_{crit} \approx 1\mathrm{m}$.

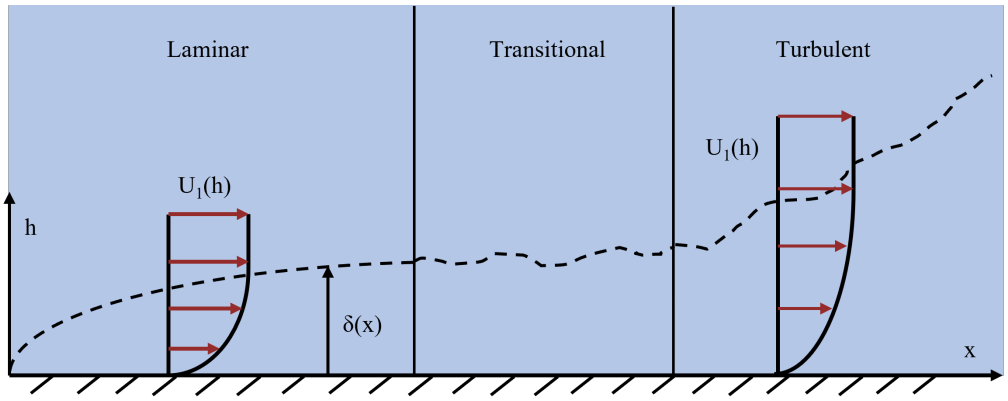

Figure 2.2: An illustration showing the development of a boundary layer.

2.1.3 Plane wake

For the static mode of the active grid (see chapter 3 and chapter 4 for further explanation), there could be wake effects behind the wings. The Reynolds number behind a cylinder is defined as $\mathrm{Re}_D = U_\infty D/\nu$, where the characteristic length D is the diameter of the cylinder, as shown in Figure 2.3. Vortex shedding behind cylinders start happening at $80 < \mathrm{Re}_D < 300$, and turbulent wakes start forming for $\mathrm{Re}_D > 300$ (Schlichting and Gersten, 2017). Figure 2.3 shows an illustration of a wake behind a cylinder. The width of the wing and the rod in the static mode is $w = 1.4$cm, which gives a Reynolds number of $\mathrm{Re}_w = \langle U_1 \rangle w/\nu \approx 1400$.

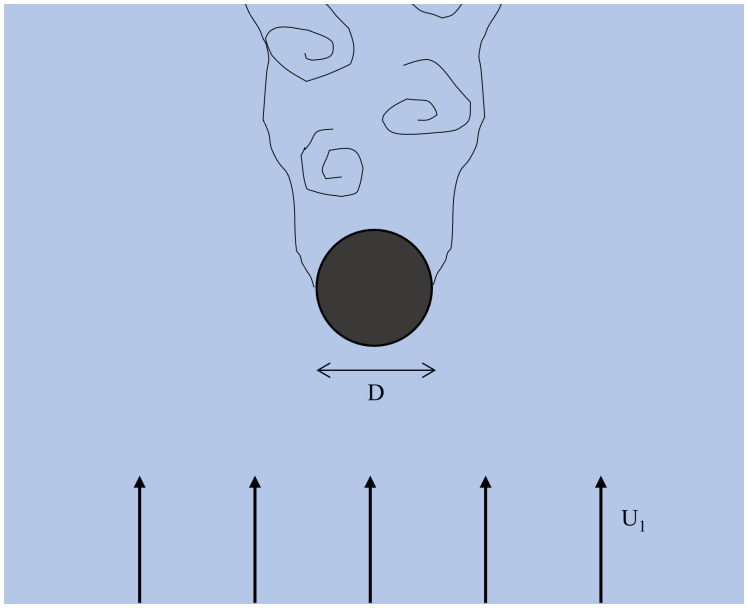

Figure 2.3: An illustration showing a wake behind a cylinder.

2.2 The scales of turbulent motion

When examining free shear flows, there have been observed that turbulent motions range in size from the width of the flow to sizes progressively smaller as the Reynolds number increases, (Pope, 2000). As seen in chapter 5, the different scales of motion play an important role when characterizing turbulence, and we will therefore look into how energy is distributed among the various scales, and examine the physical processes occurring.

2.2.1 Energy cascade

An important theme when looking into the distribution of energy among the various turbulent scales of motion is the *energy cascade*. The idea of the energy cascade was first introduced by Richardson, 1922, and is briefly summarized by Pope, 2000, as kinetic energy entering the turbulence (through the production mechanism) at the largest scales of motion. This energy is then transferred (by inviscid processes) to smaller and smaller scales until, at the smallest scales, the energy is dissipated by viscous action.

When further explaining the energy cascade, Pope, 2000, emphasizes that he is considering a turbulent flow at a *very* high Reynolds number with characteristic velocity $\mathcal{U}$ and lengthscale $\mathcal{L}$, as the concepts are easiest to grasp then. The characteristic length $\mathcal{L}$ is comparable to size of the largest scales of turbulent motion, which are described by integral length scale (see section 2.4 for explanation). The characteristic velocity of the flow $\mathcal{U}$ is the mean velocity in the channel direction, $\langle U_1 \rangle$. From the results in chapter 5 we see that for the flows considered in this thesis $\mathcal{L} \approx 0.1\text{m}$ and $\mathcal{U} \approx 0.1\text{ms}^{-1}$, which gives $\text{Re} \approx 10^4$.

Pope, 2000, writes that the first concept in Richardson's view of the energy cascade is that the turbulence can be considered to be composed of *eddies* of different size. There are no precise definition of an eddy, but it is conceived to be a turbulent motion, localized within a region of size ℓ, that is at least moderately coherent over this region. A region occupied by a large eddy can also contain smaller eddies (Pope, 2000).

An eddy has the characteristic length ℓ and the characteristic velocity $u(\ell)$. Pope, 2000 defines the characteristic length of the largest eddies as ℓ_0, which is comparable to the flow scale $\mathcal{L}$, and their characteristic velocity as $u_0 \equiv u(\ell_0)$, which is on the order of the root-mean-square turbulence intensity u which is comparable to $\mathcal{U}$. The Reynolds number of the largest eddies, $\text{Re}_0 \equiv u_0 \ell_0 / \nu$, is therefore comparable to the Reynolds number of the flow, and the direct effects of viscosity are negligibly small (Pope, 2000).

Pope, 2000 states that Richardson's notion is that the larger eddies are unstable and break up into smaller eddies, hence transferring their energy to these smaller eddies, which then again breaks up even more. This transfer of energy to smaller and smaller eddies is what is called the *energy cascade*, and it continues until the Reynolds number $\text{Re}_\ell(\ell) \equiv u(\ell)\ell/\nu$ is small enough that the eddy motion is stable and molecular viscosity is effective at dissipating the kinetic energy.

This places the dissipation at the end of the sequence, which means the *rate* of dissipation ε is determined by the first process in the sequence, which is the energy transfer from the largest eddies (Pope, 2000). The energy of the largest eddies are of the order u_0^2, and their timescales are $\tau_0 = \ell_0/u_0$. This means that the rate of transfer of energy can be supposed to scale as $u_0^2/\tau_0 = u_0^3/\ell_0$ (Pope, 2000). This indicates that for flows with high Reynolds number, the dissipation rate ε should scale as u_0^3/ℓ_0, independent of ν, which is consistent with experiments done in free shear flows (Pope, 2000).

2.2.2 Kolmogorov's hypotheses

The energy cascade does not in itself give an answer to the development of the characteristic velocity and timescales $u(\ell)$ and $\tau(\ell)$ as ℓ decrease. Kolmogorov, 1941, advanced a theory, stated in the form of three hypotheses, that gives an answer to this and more.

The first hypothesis is as follows:

Kolmogorov's hypothesis of local isotropy. At sufficiently high Reynolds number, the small-scale turbulent motions ($\ell \ll \ell_0$) are statistically isotropic (as restated by Pope, 2000).

The larger eddies are generally anisotropic and affected by the boundary conditions of the flow (Pope, 2000). Kolmogorov does however argue that the directional bias in the larger eddies dissapear in the chaotic scale-reduction process. Pope, 2000, introduce the length scale ℓ_{EI} as the divi-

sion point between the anisotropic larger eddies and the isotropic smaller eddies (with $\ell_{EI} \approx \frac{1}{6}\ell_0$). Kolmogorov, 1941, also argues that all information about the larger eddies disappears in the scale-reduction process, which as a consequence means that the smaller scale eddies are similar for all high-Reynolds number flows.

The two dominant processes in the energy cascade for eddies in the isotropic region ($\ell < \ell_{\mathrm{EI}}$) are the transfer of energy to successively smaller scales, and viscous dissipation (Pope, 2000). The rate at which smaller eddies receive energy from larger eddies is denoted by Pope, 2000 as $\mathcal{T}_{\mathrm{EI}}$. He shows that the dissipation rate ε is determined by the energy transfer $\mathcal{T}_{\mathrm{EI}}$, so that these two rates are nearly equal ($\varepsilon \approx \mathcal{T}_{\mathrm{EI}}$). This is the basis for Kolmogorov's second hypothesis, which is stated by Pope, 2000 as:

Kolmogorov's first similarity hypothesis. In every turbulent flow at sufficiently high Reynolds number, the statistics of the small-scale motions ($\ell < \ell_0$) have a universal form that is uniquely determined by ν and ε.

Given the two parameters ν and ε, there unique length, velocity, and time scales called the Kolmogorov scales:

$$\eta \equiv (\nu^3/\varepsilon)^{1/4}, \tag{2.2}$$

$$u_\eta \equiv (\nu\varepsilon)^{1/4}, \tag{2.3}$$

$$\tau_\eta \equiv (\nu/\varepsilon)^{1/2}. \tag{2.4}$$

There are two identities stemming from these three definitions that indicates that these are the scales for the smallest dissipative eddies. The first is that the Reynolds number is in unity (i.e., $\mathrm{Re}_\eta = \eta u_\eta/\nu = 1$). This is consistent with the notion that the cascade proceeds to smaller scales until the Reynolds number $u(\ell)\ell/\nu$ is small enough that dissipation is effective (Pope, 2000). The second identity is that the dissipation rate ε is given by

$$\varepsilon = \nu(u_\eta/\eta)^2 = \nu/\tau_\eta^2, \tag{2.5}$$

showing that $(u_\eta/\eta) = 1/\tau_\eta$ provides a consistent characterization of the velocity gradients of the dissipative eddies (Pope, 2000).

Pope, 2000 determine the ratios of the smallest to largest scales from the definitions of the Kolmogorov scales and from the scaling $\varepsilon \sim u_0^3/\ell_0$. The results are

$$\eta/\ell_0 \sim \mathrm{Re}^{-3/4}, \tag{2.6}$$

$$u_\eta/u_0 \sim \mathrm{Re}^{-1/4}, \tag{2.7}$$

$$\tau_\eta/\tau_0 \sim \mathrm{Re}^{-1/2}\,. \tag{2.8}$$

This shows that at high Reynolds number, the velocity scales and timescales of the smallest eddies (u_η and τ_η) are small compared to those of the largest eddies (u_0 and τ_0).

From Equation 2.6 we see that the ratio between the length scale of the smallest and the largest eddies η/ℓ_0 is decreasing with increasing Reynolds number. As a consequence of this, at sufficiently large Reynolds number , there is a range of scales ℓ which are very small compared to the largest

scales ℓ_0 and very large compared to the smallest scales η (i.e., $\ell_0 \gg \ell \gg \eta$). Since the Reynolds number for this range $u(\ell)\ell/\nu$ is much larger than for the dissipative range their motion is little affected by viscosity. Hence, following from this we have Kolmogorov's third statement, stated by Pope, 2000, as

Kolmogorov's second similarity hypothesis. In every turbulent flow at sufficiently high Reynolds number, the statistics of the motions of scale ℓ in the range $\ell_0 \gg \ell \gg \eta$ have a universal form that is uniquely determined by ε, independent of ν.

Pope, 2000 introduce the lengthscale ℓ_{DI} (with $\ell_{\mathrm{DI}} = 60\eta$), so the range in the hypothesis can be written as $\ell_{\mathrm{EI}} > \ell > \ell_{\mathrm{DI}}$. This lengthscale splits the universal equilibrium range into two subranges: *dissipation range*, which is $\ell < \ell_{\mathrm{DI}}$, and the *inertial subrange*, which is $\ell_{\mathrm{EI}} < \ell < \ell_{\mathrm{DI}}$. As the names suggest, the inertial subrange is determined by inertial effects, whereas only motions in the dissipation range experience significant viscous effects, meaning that almost all of the dissipation happens in this range.

Pope, 2000 notes that lengthscales, velocity scales, and timescales cannot be formed from ε alone. However, in the inertial subrange, give the lengthscale ℓ, the characteristic velocity scales and timescales for the eddy are those formed from ε and ℓ:

$$u(\ell) = (\varepsilon\ell)^{1/3} = u_\eta(\ell/\eta)^{1/3} \sim u_0(\ell/\ell_0)^{1/3}, \tag{2.9}$$

$$\tau(\ell) = (\ell^2/\varepsilon)^{1/3} = \tau_\eta(\ell/\eta)^{2/3} \sim \tau_0(\ell/\ell_0)^{2/3}. \tag{2.10}$$

These equations show that the velocity scale $u(\ell)$ and timescale $\tau(\ell)$ decrease with decreasing ℓ, which partly answers the question at the start of the subsection.

An important quantity in the energy cascade is the rate of which energy is transferred from eddies larger than ℓ to eddies smaller than ℓ. Pope, 2000 denotes this by $\mathcal{T}(\ell)$. If this process is accomplished by eddies of comparable size to ℓ, then the energy transfer rate $\mathcal{T}(\ell)$ should be expected to be in the order of $u(\ell)^2/\tau(\ell)$ (Pope, 2000). The identity

$$u(\ell)^2/\tau(\ell) = \varepsilon, \tag{2.11}$$

stemming from Equation 2.9 and Equation 2.10, shows that the energy transfer rate $\mathcal{T}(\ell)$ is independent of ℓ in the inertial subrange.

2.2.3 The energy spectrum

From these hypotheses we can look further into how the turbulent kinetic energy is distributed among the eddies of different size. The energy spectrum function $E(\kappa)$ (further explained in subsection 2.4.4) is a good tool to determine the energy distribution for homogeneous turbulence. κ is the wavenumber, which Pope, 2000 shows that when looking at the energy spectrum function, motions of lengthscale ℓ corresponds to the wavenumber $\kappa = 2\pi/\ell$. The energy in the wavenumber range (κ_a,κ_b) is

$$k_{(\kappa_a,\kappa_b)} = \int_{\kappa_a}^{\kappa_b} E(\kappa)\, d\kappa. \tag{2.12}$$

It follows from Kolmogorov's first similarity hypothesis that, in the universal equilibrium range ($\kappa > \kappa_{\mathrm{EI}} \equiv 2\pi/\ell_{\mathrm{EI}}$) the spectrum is a universal function of ε and ν (Pope, 2000). From the second hypothesis it follows that, in the inertial subrange ($\kappa_{\mathrm{EI}} < \kappa < \kappa_{\mathrm{DI}} \equiv 2\pi/\ell_{\mathrm{DI}}$), the spectrum is

$$E(\kappa) = C\varepsilon^{2/3}\kappa^{-5/3}, \tag{2.13}$$

where C is a universal constant (Pope, 2000). Figure 2.4 shows the empirical energy spectrum function from one of the measurements in this thesis, and an illustrative line that shows Equation 2.13.

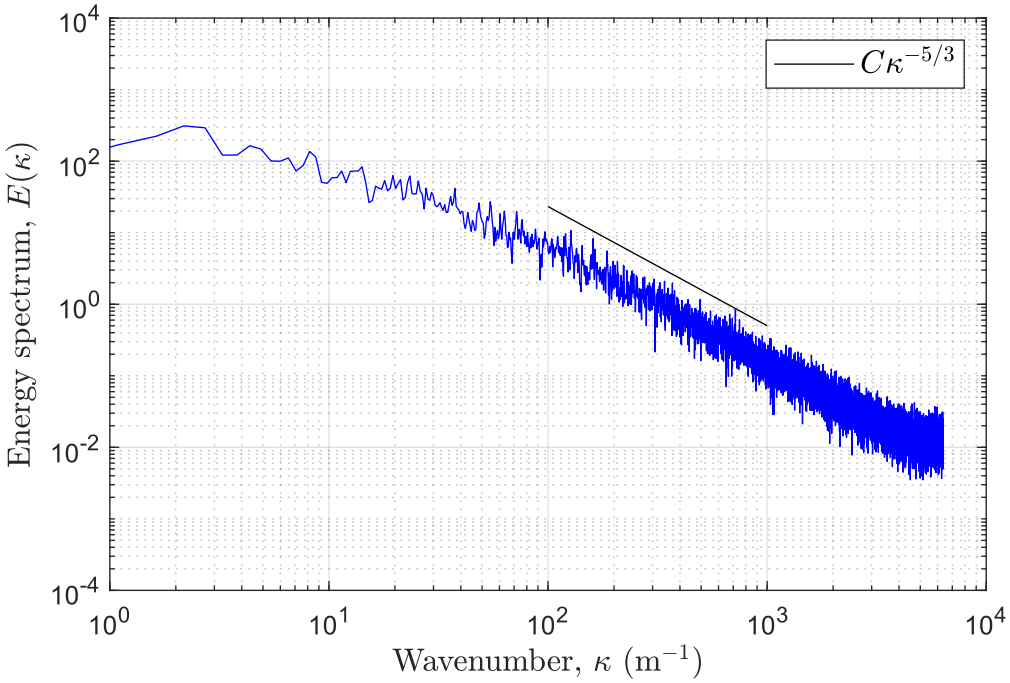

Figure 2.4: The energy spectrum for one of the turbulent time series from the experiments in this thesis. This time series is from 1st measurement of the spin mode at 40% pump power, upstream, 3cm left of the center of the channel looking from the active grid. The black straight line illustrates the Kolmogorov $-5/3$ spectrum.

Pope, 2000 uses the general power-law spectrum

$$E(\kappa) = A\kappa^p, \tag{2.14}$$

to better understand some basic features of the Kolmogorov $-5/3$ spectrum. Here, A and p are constants. The energy contained in wavenumbers greater than κ is

$$k_{(\kappa,\infty)} \equiv \int_\kappa^\infty E(\kappa')\, d\kappa' = \frac{A}{p-1}\kappa^{-(p-1)}, \tag{2.15}$$

for $p > 1$, while the integral diverges for $p \leq 1$ (Pope, 2000). Similarly the dissipation in wavenumbers less than κ is

$$\varepsilon_{(0,\kappa)} \equiv \int_0^\kappa 2\nu\kappa'^2 E(\kappa')\, d\kappa' = \frac{2\nu A}{3-p}\kappa^{3-p}, \tag{2.16}$$

for $p < 3$, while the integral diverges for $p \geq 3$ (Pope, 2000). $p = 5/3$, which corresponds with the Kolmogorov spectrum, is in the middle of the range $(1, 3)$ for which the integrals $k_{(\kappa,\infty)}$ and $\varepsilon_{(0,\kappa)}$ converge. From this we have that the amount of energy in high wavenumbers decrease as $k_{(\kappa,\infty)} \sim \kappa^{-2/3}$ as κ increases, whereas the dissipation in the low wavenumbers decreases as $\varepsilon_{(0,\kappa)} \sim \kappa^{4/3}$ as κ decreases towards zero.

2.3 Turbulent flows close to free surface

The concept of *eddies* were introduced in section 2.2 as turbulent motion at least moderately coherent over a region of size ℓ. Brocchini and Peregrine, 2001 state that the major influence of turbulence on the free surface comes from these eddies moving upward to the surface or moving parallel to it and, hence, disturbing it. Figure 2.5 illustrates an eddy moving upwards towards the surface and an eddy moving parallel to it.

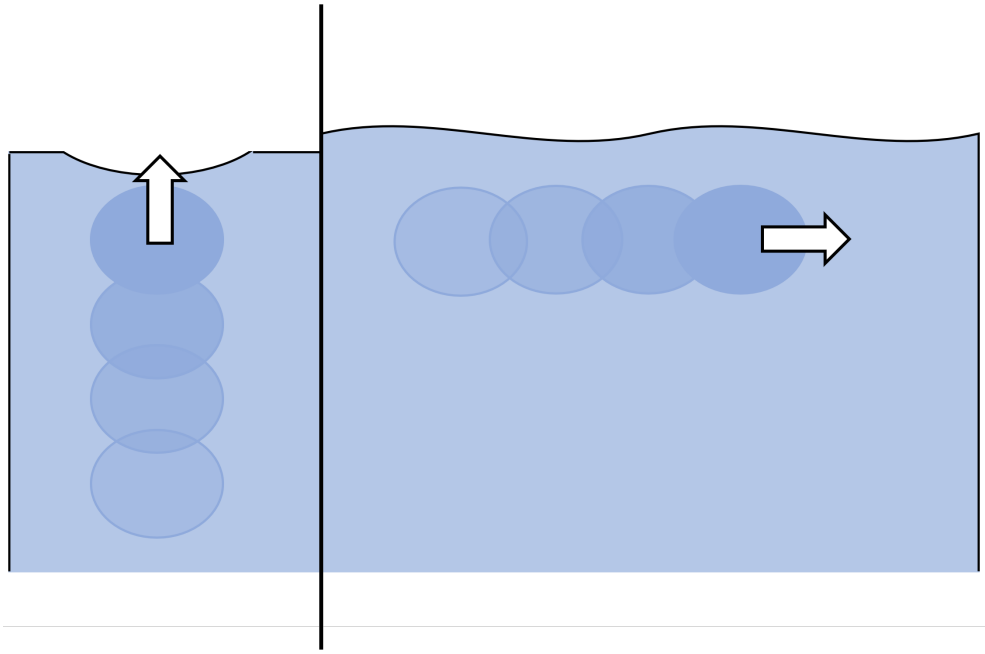

Figure 2.5: An illustration of eddies disturbing the surface by moving towards the surface, as shown on the left, or moving parallel to the surface, as shown on the right.

2.3.1 Terminology and quantification

Brocchini and Peregrine, 2001, choose to call the eddies for *blobs*, as it better conveys the behaviour of the liquid than the term eddy used with single-phase turbulent flow. The length scale of the blobs ℓ corresponds often with the most energetic turbulent scales, which we from section 2.2 know are the largest scales, which are quantified by the integral length scale $\bar{\ell}$ (see subsection 2.4.3). The velocity scale of the blobs $u(\ell)$ of this length scale is the turbulent velocity u. From chapter 5 we see that the length scale in the experiments in this thesis is $\ell \approx 0.1\text{m}$ and the velocity scale is $u(\ell) \approx 0.01\text{ms}^{-1}$. The blobs have a representative kinetic energy $k = \frac{1}{2}u(\ell)^2 \approx 5 \times 10^{-5}\text{m}^2\text{s}^{-2}$.

Brocchini and Peregrine, 2001 note that there are also other features on the surface to consider, such as downwelling lines of scars around blobs or more point-like depressions terminating strong vortices. These are features that usually occur at more turbulent flows than in the experiments in this thesis, such as wakes. We therefore focus on the disturbances directly caused by the blobs.

Just like Brocchini and Peregrine, 2001, we introduce the two stabilizing factors of gravity and surface tension to chart the discussion of the water surface. Viscous effects are given less attention here as the Reynolds number is high enough ($\text{Re}_\ell = u(\ell)\ell/\nu \approx 10^3$) so that viscous forces are small compared to the inertial forces.

For gravity the corresponding specific energy densities $g\ell$, where g is the gravitational acceleration ($g \approx 9.81\text{ms}^{-2}$), and $\frac{1}{2}u(\ell)^2$ are compared. Brocchini and Peregrine, 2001, introduce the turbulent Froude number $\text{Fr} = u(\ell)/(2g\ell)^{1/2}$ which is a ratio between these two specific energy densities. Low Froude number ($\text{Fr} \ll 1$) means that the kinetic energy in the turbulent blobs is insufficient

to overcome the gravitational forces and disturb the surface. This leads to a nearly flat surface. At high Froude number ($\mathrm{Fr} \gg 1$), the gravitational forces are not strong enough to counteract the turbulent blobs, and there will be average excursions of the free surface that will be of the order $O(u(\ell)^2/2g)$ (Brocchini and Peregrine, 2001). At $\mathrm{Fr} \sim O(1)$ is the most varied behaviour, as the inertial forces and gravitational forces are constantly trying to dominate. The turbulent Froude number Fr in the experiments in this thesis are $\mathrm{Fr} \approx 0.01$, meaning that gravity is dominating the surface, and the surface should be expected to be nearly flat. This is also what was observed when conducting the experiments.

For surface tension we compare the specific surface energy $S = T/\rho_{\mathrm{water}}$ and $\frac{1}{2}u(\ell)^2\ell$. T here is the surface energy density ($T \approx 7.4 \times 10^2 \mathrm{Nm}^{-1}$ for water-air surface) and ρ_{water} is the density of water ($\rho_{\mathrm{water}} \approx 10^3 \mathrm{kgm}^{-3}$). Brocchini and Peregrine, 2001 introduce the Weber number $\mathrm{We} = u(\ell)^2\ell/2S$ which is the ratio between the surface tension energy and the kinetic energy of the blobs. As for the Froude number Fr, a low Weber number ($\mathrm{We} \ll 1$) means that the surface tension dominates the kinetic energy of the blobs, which means there are little to no disturbance to the surface. A high Weber number ($\mathrm{We} \gg 1$) means that the kinetic energy of the blobs is high enough to overcome the surface tension which indicates that the surface could disintegrate into drops. $\mathrm{We} \sim O(1)$ leads to surface features that might involve wave-like behaviour (Brocchini and Peregrine, 2001). The Weber number We in the experiments in this thesis is $\mathrm{We} \approx 0.1$, which is an order of magnitude larger than the Froude number, indicating that gravity is more important than surface tension, and it would be expected that the surface is relatively flat and only wrinkled by the sub-surface turbulence. This also corresponds well with what was observed during the experiments.

Some of the implications of sub- and supercritical values of the Froude number Fr and the Weber number We are described in the previous paragraphs. However, both gravity and surface tension act on the water surface simultaneously, thus both Fr and We must be considered together. Brocchini and Peregrine, 2001 seek to delineate a critical region of parameter space between quiescent surfaces and surfaces that break up completely. This region is loosely illustrated in Figure 2.6 as the region between the two black curved lines.

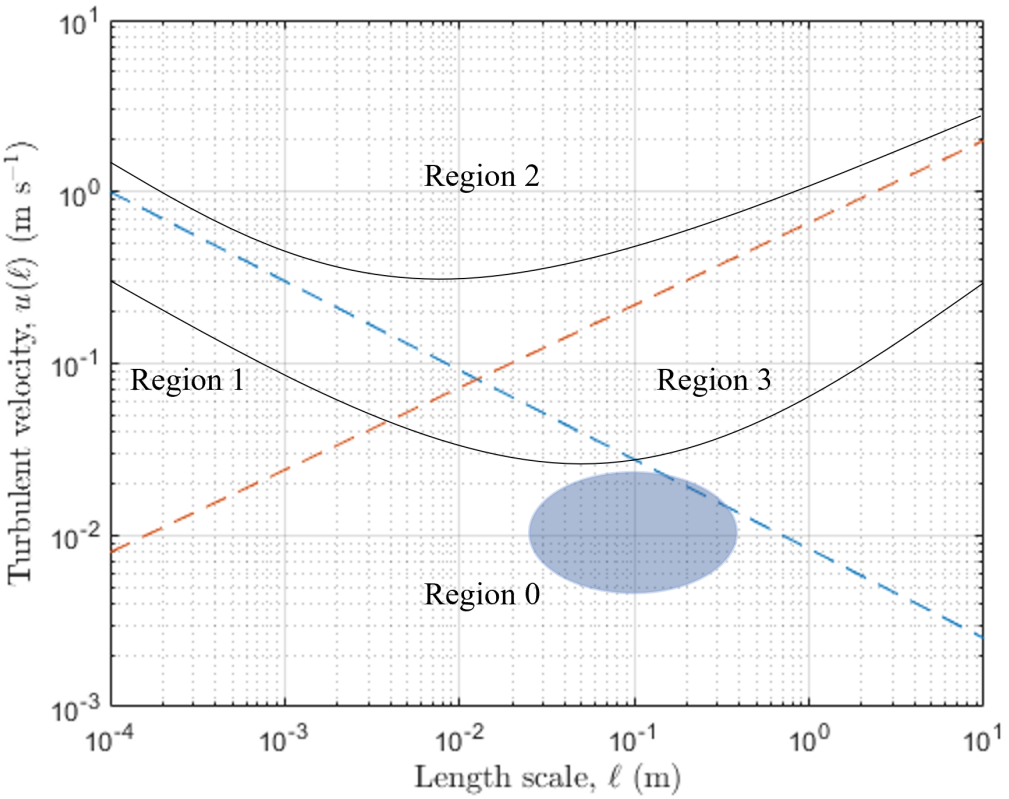

Figure 2.6: A diagram of the $(u(\ell), \ell)$-plane for water. The two black curved lines loosely shows the top and bottom of the critical region where the surface starts to break up completely. The blue dashed line indicates the critical Weber number $\mathrm{We}_{\mathrm{crit}}$, and the orange dashed line indicates the critical Froude number $\mathrm{Fr}_{\mathrm{crit}}$. The blue region shows where the experiments in this thesis lie in this diagram. This figure is inspired by Figure 4 in Brocchini and Peregrine, 2001.

The dashed lines in Figure 2.6 represent the critical Froude number $\mathrm{Fr}_{\mathrm{crit}}$ and Weber number $\mathrm{We}_{\mathrm{crit}}$, and they divide the plane into four different regions. These four regions represent four different characteristics of free-surface turbulence. The blue shaded area shows where the turbulent flows in the experiments in this thesis lie in this diagram, and it shows that it lies in Region 0, bordering towards Region 3. The observations made from the experiments does however only correspond with the descriptions of Region 0, and we will therefore only look further into the characteristics of this region.

2.3.2 Weak turbulence

Turbulence in Region 0 indicates that both the Froude number and the Weber number of the turbulence are small. This is characterized by Brocchini and Peregrine, 2001, as weak turbulence, and it is a state where there is little or no surface disturbance. This state corresponds to the rigid-lid free-slip studies of free-surface turbulence, and there have been made numerous studies on the interaction between turbulence and such free surface. Brocchini and Peregrine, 2001, mentions some important ones, such as Gibson and Rodi, 1989, Rashidi et al., 1992, Handler et al., 1993, Borue et al., 1995, Walker, Chen et al., 1995, Walker, Leighton et al., 1996 and L. Shen et al., 1999.

Brocchini and Peregrine, 2001 draws attention to that the single velocity and length scales are inadequate to represent the multitude of length, time and velocity scales that occur in a turbulent flow, as discussed in section 2.2. For example, even in a weak turbulent flow there is likely to be disturbances matching the length scales satisfying the linear surface wave dispersion relation. This

is apparent in the results without generated waves from Løvvig, 2023.

Brocchini and Peregrine, 2001 state that if waves exist on the water surface, then the weak turbulence with a greater length scale than the waves has an effect on their propagation. This can be significant if the resulting wave refraction leads to wave focusing.

2.4 Statistical description of turbulent flows

2.4.1 The random nature of turbulence

In subsection 2.1.1 it is stated that the velocity field $\mathbf{U}(\mathbf{x}, t)$ varies significantly and irregularly in both position and time. This tells us that the velocity field is *random*. Pope, 2000, gives an explanation to what the word 'random' means when talking about velocity fields:

"Consider a fluid-flow experiment that can be repeated many times under a specified set of conditions, $\mathcal{C}$, and consider an event A, such as $A \equiv U < 10\text{ms}^{-1}$, where U is a specified component of velocity at a specified position and time (measured from the initiation of the experiment). If the event A inevitably occurs, then A is *certain* or *sure*. If the event A cannot occur, then it is *impossible*. The third possibility is that A may occur but it need not occur. In this case the event A is *random*. Then, in the example $A \equiv U < 10\text{ms}^{-1}$, U is a *random variable*."

Pope also emphasizes that the word 'random' only means that an event A is neither impossible nor certain, and that is says nothing about how likely it is.

This random nature of turbulent flows does give some consistency issues with the deterministic nature of classical mechanics, embodied in the Navier-Stokes equations. Why is the velocity field random if the mechanics governing it are completely deterministic? Pope, 2000 answers this with the combination of two observations.

1. In any turbulent flow there are, unavoidably, perturbations in initial conditions, boundary conditions, and material properties.
2. Turbulent flow fields display an acute sensitivity to such perturbations.

This means that the specified set of conditions $\mathcal{C}$ will always have small perturbations, such as inhomogeneties in the fluid, or small vibrations in the apparatus. In laminar flow these small perturbations would not have a significant effect on the flow, as it is stable. In a turbulent flow however, these perturbations could change the velocity field drastically after just a short amount of time or a small displacement in space. An example of how small perturbations in initial conditions can drastically change the evolution of an unstable system is shown by Lorenz, 1963.

2.4.2 Statistical quantities

As mentioned in subsection 2.4.1, the velocity U is a random variable, which means it is inherently unpredictable. This means that a theory predicting a certain value of U would most likely be wrong. It is however possible to create theories that aims at predicting the *probability* of a certain event A, such as $A \equiv U < 10\text{ms}^{-1}$, (Pope, 2000).

It is emphasized by Pope, 2000 that the random variable U is fully characterized by the *probability density function* (PDF), or equally by the *cumulative distribution function* (CDF). This means that two or more random variables that have the same PDF are *identically distributed*, or *statistically identical*.

Pope, 2000 introduce the the independent velocity variable V to explain the CDF and PDF. CDF is the probability that the random variable U is less than V:

$$F(V) \equiv P\{U < V\} \tag{2.17}$$

It has three basic properties, which are

$$F(-\infty) = 0 \tag{2.18}$$

because $\{U < -\infty\}$ is impossible;

$$F(\infty) = 1 \tag{2.19}$$

because $\{U < \infty\}$ is certain; and,

$$F(V_b) \geq F(V_a), \quad \text{for} \quad V_b > V_a \tag{2.20}$$

since the probability of every event is non-negative, (Pope, 2000).

The PDF is defined as the derivative of the CDF:

$$f(V) \equiv \frac{\mathrm{d}F(V)}{\mathrm{d}V} \tag{2.21}$$

An example of the empirical found CDF of one of the velocity measurements done in this thesis and its corresponding PDF is shown in Figure 2.7.

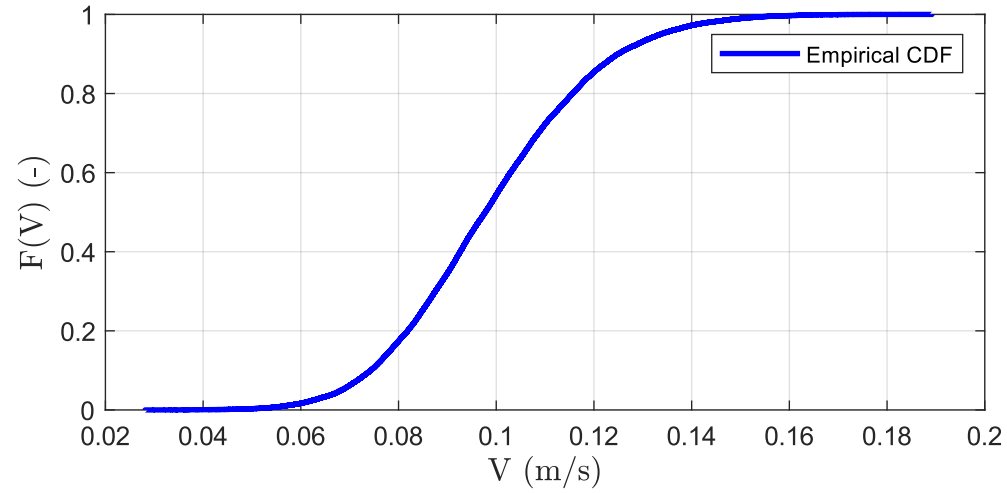

(a) Empirical CDF

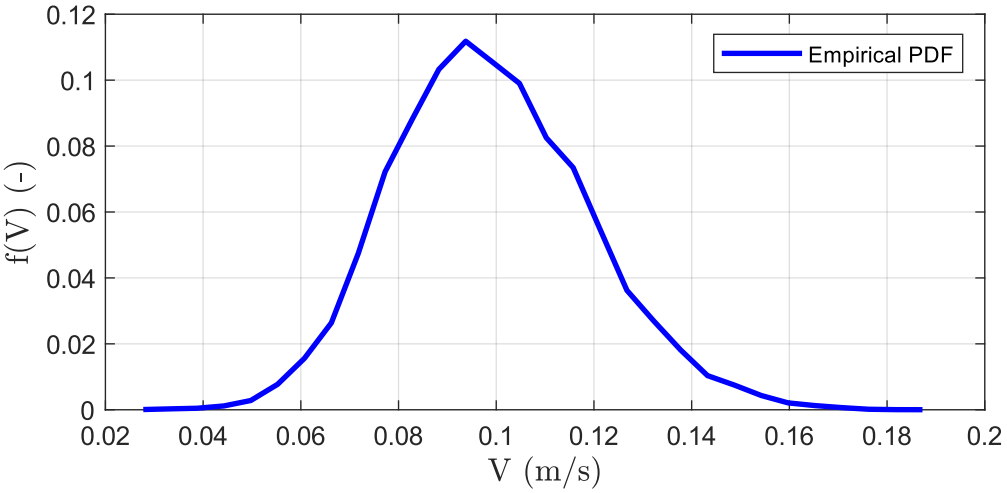

(b) Empirical PDF

Figure 2.7: These show the empirical CDF and PDF of one of the turbulent time series from the experiments in this thesis. This is from the 1st measurement of the spin mode at 40% pump power, upstream, 3cm left of the center of the channel looking from the active grid. The PDF is a probability normalized histogram, represented by a curve, so the values on the y-axis is not representative for the actual PDF, but the shape is.

From the PDF, Pope, 2000, derives statistical quantities that are used in this thesis to characterize and quantify the flow. The first one is the *mean* velocity $\langle U \rangle$, which is defined by:

$$\langle U \rangle \equiv \int_{-\infty}^{\infty} V f(V)\, dV. \tag{2.22}$$

Since the PDF is unknown for the flows in these experiments, the mean velocity is calculated by averaging all the measured velocities:

$$\langle U \rangle = \frac{\sum_{i=1}^{N} U_i g_i}{\sum_{i=1}^{N} g_i}. \tag{2.23}$$

Here U_i is a single velocity measurement, N is the number of measurements, and g_i is a weighting

factor which is added due to some properties of LDV data. This is further explained in section 3.2.

Higher order *moments* are also used to characterize turbulent flows. The higher order moments are calculated by averaging higher orders of the *fluctuation* in U, which is defined by

$$u' \equiv U - \langle U \rangle \,. \tag{2.24}$$

The second central moment, or the *variance*, is defined to be the mean-square fluctuation:

$$\mathrm{var}(U) \equiv \left\langle u^2 \right\rangle = \int_{-\infty}^{\infty} (V - \langle U \rangle)^2 f(V)\, dV. \tag{2.25}$$

This is in this thesis, like with the mean velocity $\langle U \rangle$, calculated by averaging the square fluctuation

$$\left\langle u^2 \right\rangle = \frac{\sum_{i=1}^{N} (U_i - \langle U \rangle)^2 g_i}{\sum_{i=1}^{N} g_i}. \tag{2.26}$$

The variance gives a value to how much the flow fluctuates from the mean velocity, which indicates how *intense* the turbulence is.

2.4.3 Autocorrelation and Integral length scale

The random variable U was introduced in subsection 2.4.1 and it was stated that it is completely characterized by its PDF. If the same velocity is a function of time $U(t)$, then the variable would be what is called a *random process*, (Pope, 2000). To completely characterize a random process it is necessary to know the joint PDF for all instances of time, which is impossible. If the random process is *statistically stationary* however, then considerable simplifications can be made. A turbulent flow can reach a statistical stationary state after an initial time, where even though the flow variable $U(t)$ varies with the time, the statistics are independent of time (Pope, 2000). That is shown with the case in Figure 2.8, where the mean velocity $\langle U \rangle$ and the variance $\left\langle u^2 \right\rangle$ converge to single values after enough time.

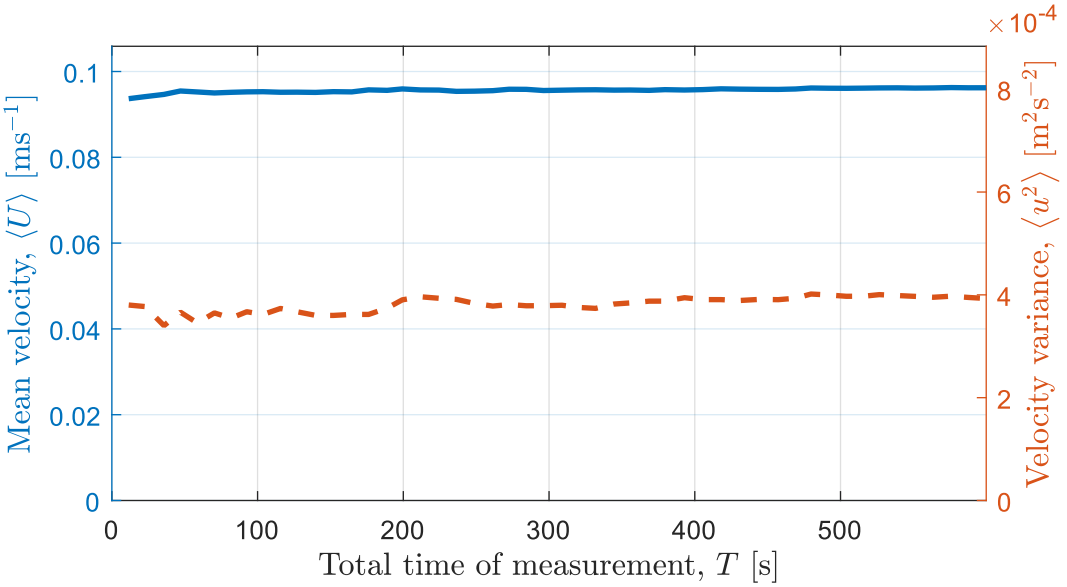

Figure 2.8: This shows calculated values of mean velocity $\langle U \rangle$ and variance $\langle u^2 \rangle$ for different fractions of a time series. It is used to show that the values converge as the time series grow larger. This is from the 1st measurement of the flapping mode at 40% pump power, upstream, 3cm left of the center of the channel looking from the active grid. The orange dashed line shows the variance $\langle u^2 \rangle$, and the solid blue line shows the mean velocity $\langle U \rangle$.

Pope, 2000, states that for a statistically stationary process, the simplest multi-time statistic that can be considered is the *autocovariance*

$$R(s) \equiv \langle u(t)u(t+s) \rangle \,, \tag{2.27}$$

where s is time lag. In normalized form it is called the *autocorrelation function*

$$\rho(s) \equiv \frac{\langle u(t)u(t+s) \rangle}{\langle u(t)^2 \rangle}. \tag{2.28}$$

It should be noted here that $u(t)$ is the time-dependent velocity fluctuation $u(t) \equiv U(t) - \langle U \rangle$. The autocorrelation function $\rho(s)$ is the correlation coefficient between the process at times t and $t+s$ (Pope, 2000).

If the time-dependent variable, in this case $U(t)$, is periodic with a period T, then the autocorrelation function $\rho(s)$ is also periodic with a period T (i.e., $\rho(s+T) = \rho(s)$), (Pope, 2000). Pope, 2000, states, however, that for processes arising in turbulent flows, it is expected that the correlation diminish as the lag time s increases. Normally the autocorrelation $\rho(s)$ decrease sufficiently rapidly with increasing s so that the integral

$$\bar{\tau} \equiv \int_0^\infty \rho(s)\, ds \tag{2.29}$$

converges (Pope, 2000). If so, then $\bar{\tau}$ is the *integral timescale* of the process.

In subsection 2.2.1 the concept of *eddies* is introduced as a turbulent motion, localized within a region, that is at least moderately coherent over this region. The integral timescale $\bar{\tau}$ gives a timescale of how far the process $U(t)$ can be shifted in time before the correlation is insignificantly small. This gives a scale that relates to the definition of eddies, but the eddies span in space rather in time. To get a length scale of the largest eddies we use *Taylor's hypothesis* (Taylor, 1938).

The hypothesis states that if the velocity is measured at one fixed point, as is the case in the experiment in this thesis, if the velocity of the stream that carries the eddies is way greater than the turbulent velocity (i.e., $u/\langle U_1 \rangle \ll 1$), one may assume that the changes in U at the fixed point are simply due to the passage of an unchanging pattern of turbulent motion over the point (Taylor, 1938). In other terms, in a frame moving with the eddies, the fixed measurement point would be moving with the velocity $\mathbf{e}_1 V = -\langle \mathbf{U} \rangle = -\mathbf{e}_1 \langle U_1 \rangle$, hence a displacement in space r_1 in the direction of U_1 would be equivalent with $r_1 = -\langle U_1 \rangle s$, (Pope, 2000).

It should be noted, as implied in the previous paragraph, that this hypothesis only holds if $u/\langle U_1 \rangle \ll 1$. From the results in Figure 2.8, we see that $u/\langle U_1 \rangle \approx 0.2$ in the experiments in this thesis.

Using Taylor's hypothesis, the *integral length scale* can be defined by

$$\bar{\ell} \equiv \int_0^\infty \rho(r_1)\, dr_1 = \langle U_1 \rangle \bar{\tau}. \tag{2.30}$$

This gives a length scale of where the process $U(x_1)$ correlates if it is shifted in space. This corresponds with the definition of eddies, which means it can be used as a quantity of the length scale of the largest eddies.

Since it is impossible to get continuous data of the time-dependent fluctuation $u(t)$, due to the random nature of the process, it is impossible to measure the continuous autocorrelation function. This means a numerical approach is needed to calculate the integral timescale $\bar{\tau}$ and the integral length scale $\bar{\ell}$. The integral timescale is approximated by

$$\bar{\tau} \approx \sum_{i=0} \Delta s \rho(i\Delta s). \tag{2.31}$$

Here Δs is the change in time lag for each iteration. From this, the approximation for the integral length scale becomes

$$\bar{\ell} = \langle U_1 \rangle \bar{\tau} \approx \langle U_1 \rangle \sum_{i=0} \Delta s \rho(i\Delta s). \tag{2.32}$$

Trush et al., 2020, have made comparisons of two different cutoff points for the summation when approximating the integral length scale. The first is as the autocorrelation crosses zero (i.e., sum for all $\rho(\Delta s) > 0$), and the second is as the autocorrelation crosses $1/e$ (sum for all $\rho(\Delta s) > 1/e$). They conclude that using $1/e$ as the cutoff point seems to be more stable with smaller deviations, and is therefore recommended concerning repeatability. That is why it has been used as the cutoff value in this thesis. Figure 2.9 shows the autocorrelation $\rho(s)$ for one of the experiments in this thesis, and the dashed lines show the two different cutoff points.

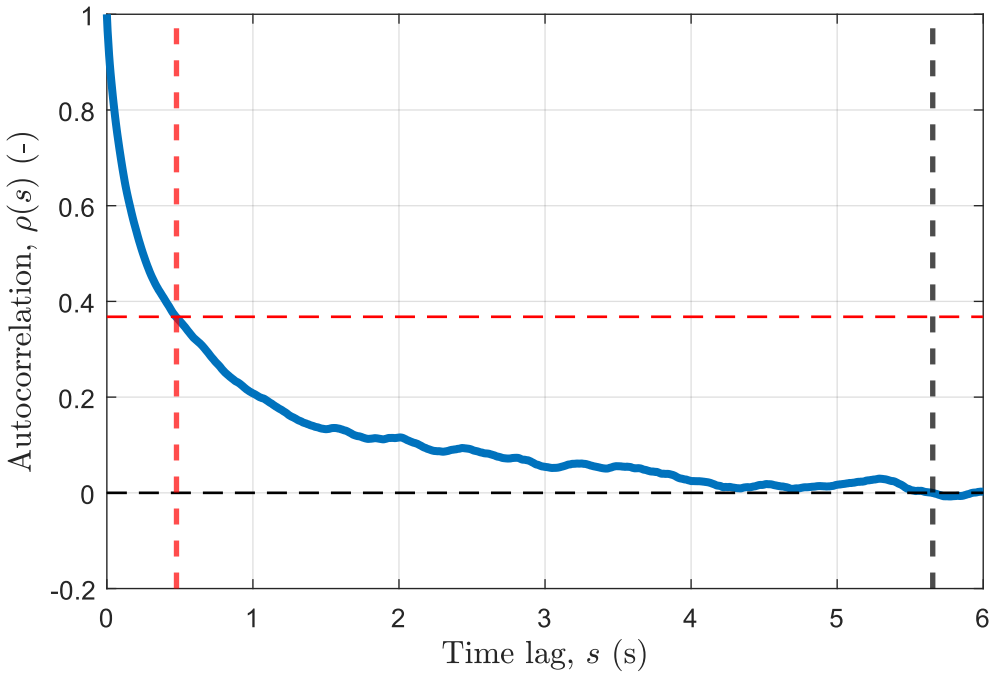

Figure 2.9: This shows the autocorrelation function to one of the time series. This is from the 1st measurement of the spin mode at 40% pump power, upstream, 3cm left of the center of the channel looking from the active grid. The blue solid line is the autocorrelation function $\rho(s)$, the red dashed lines show the cutoff point at $1/e$, and the black dashed lines show the cutoff point at 0.

This approximation requires that the velocity data is equitemporal, which is not the case for LDV data (see section 3.2 for further explanation). This means that the data from the experiments in this thesis would need to be re-sampled, which is a potential source of error (see section 3.2). A workaround this is proposed by Mora and Obligado, 2020. They have estimated the integral length scale on turbulent flows from the zero crossings of the longitudinal velocity fluctuation:

$$\bar{\ell}_{McF} \approx \frac{\pi}{4} \frac{\langle \Delta Z_1^2 \rangle}{\langle \Delta Z_1 \rangle}, \tag{2.33}$$

where ΔZ_1 is the longitudinal interval distance between two successive zero crossings. This approach does not require a re-sampling of the velocity data, as the zero crossings can be found by linearly interpolating between the time steps where the fluctuation $u(t)$ changes sign.

Both ways of calculating the integral length scale are used in section 5.2, but only Equation 2.32 is used in the rest of the results since it gives more stable results. This is also discussed in section 5.2.

2.4.4 Velocity spectra

The autocovariance $R(s)$, which is introduced in subsection 2.4.3, form a Fourier-transform pair with (twice) the *frequency spectrum* $E(\omega)$ (Pope, 2000)

$$E(\omega) \equiv \frac{1}{\pi} \int_{-\infty}^{\infty} R(s) e^{-i\omega s}\, ds = \frac{2}{\pi} \int_{0}^{\infty} R(s) \cos(\omega s)\, ds, \tag{2.34}$$

and

$$R(s) = \frac{1}{2}\int_{-\infty}^{\infty} E(\omega)e^{i\omega s}\,d\omega = \int_{0}^{\infty} E(\omega)\cos(\omega s)\,d\omega. \tag{2.35}$$

This shows that $R(s)$ and $E(\omega)$ contain the same information in different forms. It should be noted here that $R(s)$ is an even function, and $E(\omega)$ is therefore also even (Pope, 2000).

Similar to the frequency spectrum $E(\omega)$ we have that the *longitudinal wavenumber spectrum* $E(\kappa_1)$ forms a Fourier-transform pair with the *spatial longitudinal autocovariance* $R(r_1)$:

$$E(\kappa_1) \equiv \frac{1}{\pi}\int_{-\infty}^{\infty} R(r_1)e^{-i\kappa_1 r_1}\,dr_1 = \frac{2}{\pi}\int_{0}^{\infty} R(r_1)\cos(\kappa_1 r_1)\,dr_1, \tag{2.36}$$

and

$$R(r_1) = \frac{1}{2}\int_{-\infty}^{\infty} E(\kappa_1)e^{i\kappa_1 r_1}\,d\kappa_1 = \int_{0}^{\infty} E(\kappa_1)\cos(\kappa_1 r_1)\,d\kappa_1. \tag{2.37}$$

Given that Taylor's hypothesis is valid for the flow the relation between the frequency ω and the longitudinal wavenumber κ_1 is

$$\omega = \langle U_1 \rangle \kappa_1. \tag{2.38}$$

We can input this into Equation 2.36 together with $r_1 = -\langle U_1 \rangle s$ from subsection 2.4.3 and we get

$$E(\kappa_1) = \frac{1}{\pi}\int_{-\infty}^{\infty} R(r_1)\cos(-\frac{\omega}{\langle U_1 \rangle}\langle U_1 \rangle s)\,dr_1 = \frac{1}{\pi}\int_{-\infty}^{\infty} R(r_1)\cos(\omega s)\,dr_1. \tag{2.39}$$

Since we have $r_1 = -\langle U_1 \rangle s$, a variable change of the integral in Equation 2.39 would give

$$E(\kappa_1) = \langle U_1 \rangle \frac{1}{\pi}\int_{-\infty}^{\infty} R(s)\cos(\omega s)\,ds = \langle U_1 \rangle E(\omega), \tag{2.40}$$

as $dr_1 = -\langle U_1 \rangle ds$ and

$$\lim_{r_1 \to \infty} s(r_1) = \begin{cases} \infty, & \text{if } \langle U_1 \rangle < 0 \\ -\infty, & \text{if } \langle U_1 \rangle > 0 \end{cases} \quad \text{and} \quad \lim_{r_1 \to -\infty} s(r_1) = \begin{cases} \infty, & \text{if } \langle U_1 \rangle > 0 \\ -\infty, & \text{if } \langle U_1 \rangle < 0 \end{cases}.$$

It was shown in subsection 2.2.3 how the energy spectrum function $E(\kappa)$ is used to determine the energy distribution of the different length scales of turbulent motion. If the turbulence in the flow is homogeneous, the longitudinal wavenumber spectrum $E(\kappa_1)$ is equivalent with the energy spectrum function $E(\kappa)$. This means that $E(\kappa_1)$ can be used to determine the energy distribution of the different length scales of turbulent motion, given homogeneous turbulence.

Since the velocity data from the experiments does not give a continuous function for the autocovariance $R(s)$, we need to do a discrete Fourier transform (DFT) of the autocovariance to get the frequency spectrum

$$E(\omega) = 2\mathcal{F}(R(s)). \tag{2.41}$$

Here $\mathcal{F}$ signifies a Fourier transform. The calculated frequency spectrum can then be used to calculate the wavenumber spectrum $E(\kappa)$ using Equation 2.40. An example of a wavenumber spectrum from one of the experiments in this thesis is shown in Figure 2.4 in section 2.2.

Chapter 3

Experimental methods

This chapter explains the methods used to complete the research objectives given in section 1.2, which are set to answer the research question of this thesis. The methods include generation of turbulence, velocity measurements, and signal processing to analyze the turbulence intensity and integral scales of the flows. Wave generation is also an important part of the experiments in this thesis, but it has mainly been the domain of the other master student, Inger S. Løvvig, working with the same experimental setup. I have therefore copied the method for wave making from Løvvig, 2023, and it is therefore not included in this thesis.

As mentioned in chapter 2, the work in this thesis is a continuation of the work done in Djupesland, 2022, and some of the experimental methods are similar to the methods in that report. From here on, Djupesland, 2022 will be referred to as the "project thesis".

3.1 Turbulence generation

Turbulence is a common occurrence in nature and it has great implications in many fields like, for example, meteorology, aerodynamics, and chemical processes. It has therefore been important to study turbulent flows, and numerous experimental studies have been conducted to generate and tailor turbulence so that different parameters can be tested. Some recent ones are Cekli and van de Water, 2010, Rockel et al., 2017, Mulla et al., 2019, and Jooss et al., 2021.

3.1.1 Active grid design

An increasingly popular way to generate and tailor turbulence is by the use of an active grid (Mydlarski, 2017). An active grid means a grid that is moving, as opposed to a static grid. Active grids have been used both in water channels and in wind tunnels, and the designs often vary with which type of turbulent flows are being studied. Hearst, 2019, made an overview of the active grids that presently exist around the globe, with a focus on homogeneous turbulent flows, turbulent boundary layers, and model testing. He concludes that a *Makita*-style active grid is the most commonly used. This consist of a mesh of rods that are individually rotated by stepper motors. Each rod has a series of *wings* mounted to them, and therefore rotated together with the rods. An illustration of a Makita grid is shown in Figure 3.1.

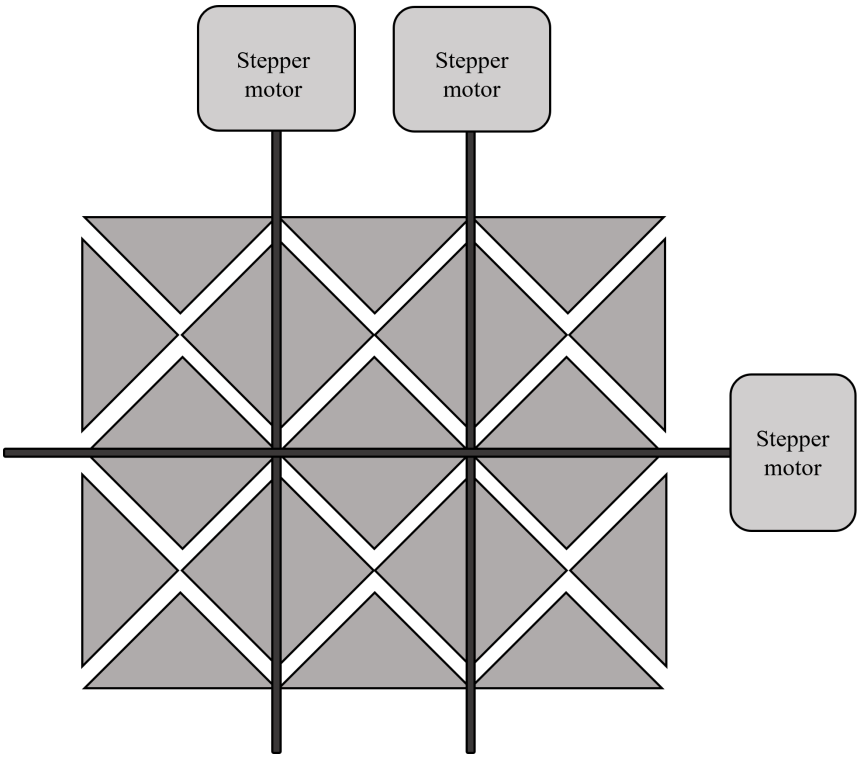

Figure 3.1: An illustration of a 2×1 Makita-style grid. The gray diamonds represent the wings, and the black lines represent the rods. The half-wings on the edges are stationary.

The aim in the experiments in this thesis is to generate turbulence with different intensities and integral length scales to investigate how these properties are affected by surface waves. This is similar to Jooss et al., 2021, where they used an active grid in a water channel to generate different free-stream turbulence intensities. Due to this, the design of the active grid in this thesis has been heavily influenced by the design of the active grid in Jooss et al., 2021. The grid they use is based on Hideharu, 1991, with rods in two directions equipped with square wings, similar to whats illustrated in Figure 3.1. The wings also have to holes to prevent 100% blocking from occurring.

The main difference between the experiments in this thesis and the experiments in Jooss et al., 2021, is that the water channel in this thesis is shallow (10cm depth). This means that a full biplanar grid would not fit in this water channel. The design choice therefore became 12 rods across the width of the channel with a single wing equipped to it, as illustrated in Figure 3.2.

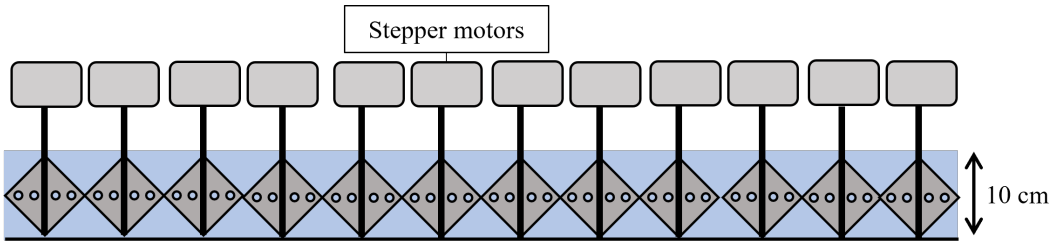

Figure 3.2: An illustration of the active grid used in this thesis. The blue in the figure illustrates the water in the water channel.

The decision of going for four small holes in each wing, rather than two larger ones like in Jooss et al., 2021, was purely down to it being easier to make. It was deemed to be sufficient to stop full blocking, especially considering that the wings do not cover the whole cross section of the channel, and with the tools available it was easier to make smaller holes.

3.1.2 Mode design

Once the grid design was finalized, various modes had to be designed to generate turbulence with different intensities and integral length scales. The initial modes were designed to be qualitatively different in hope that they would generate different turbulent flows. The four modes are: static, spinning, 60°-flapping, and 180°-flapping.

Static

The static mode means that wings are static in the position that least block the channel flow. The position of the wings in the static mode is illustrated in Figure 3.3, as seen from above.

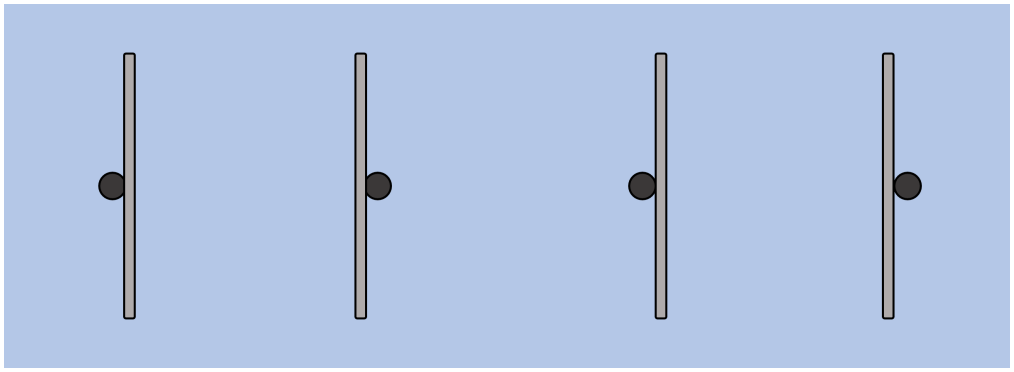

Figure 3.3: Illustration of the static mode. The figure shows the wings and rods as seen from above.

Spinning

The spinning mode means that the rods are spinning, and that they change direction randomly. Figure 3.4 illustrates how the rod spins in both directions, and how the wing is connected to it.

How frequently the spinning changes direction is a parameter of this mode. The duration of spinning in one direction is randomly chosen from a time interval that is decided before the mode starts, and a new time duration is chosen for every direction change. The time intervals used in this thesis are given in Table 3.1. The other two parameters of this mode are angular velocity and angular acceleration. Both of these are randomly selected from pre-decided ranges, and they are selected every direction change. The ranges used in this thesis are given in Table 3.1.

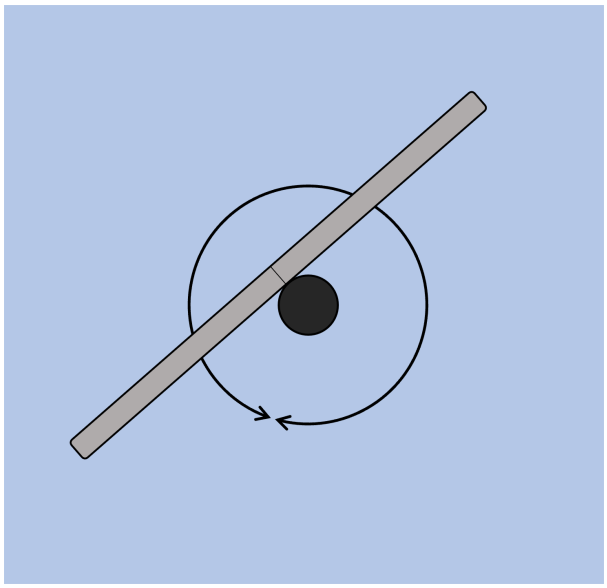

Figure 3.4: Illustration of the spinning mode. The figure shows the wings and rods as seen from above. The arrow illustrates that the rod can rotate both ways.

60°-flapping

The 60°-flapping mode means that the rods are rotating 60° back and forth, with the position of the static mode, as shown in Figure 3.3, as the midpoint in the rotation. This is illustrated in Figure 3.5.

How frequently the wings flap is one of the parameters of this mode. It is chosen similarly to the time duration of spinning in one direction for the spinning mode, where a time interval is pre-decided, and the time duration between each rotation is randomly selected from this interval. The time intervals used in this thesis are given in Table 3.1. The angular velocity and acceleration are the other two parameters of this mode, and they are pre-decided, and remain constant throughout the whole duration of the mode. The angular velocities and accelerations used in this thesis are given in Table 3.1.

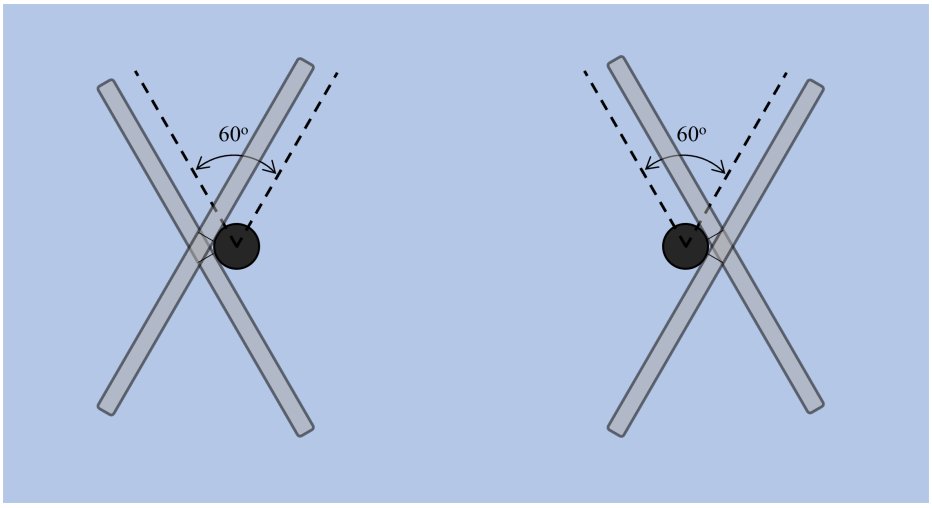

Figure 3.5: Illustration of the 60°-flapping mode. The figure shows the wings and rods as seen from above. The arrows illustrates that the rod rotates 60°, and the wings are shown at the two extreme points in the rotation.

180°-flapping

The 180°-flapping mode is equal to the 60°-flapping mode, except that the rods rotate 180° instead of 60°. It is illustrated in Figure 3.6. The time intervals, and the angular velocity and acceleration, used in this thesis are given in Table 3.1.

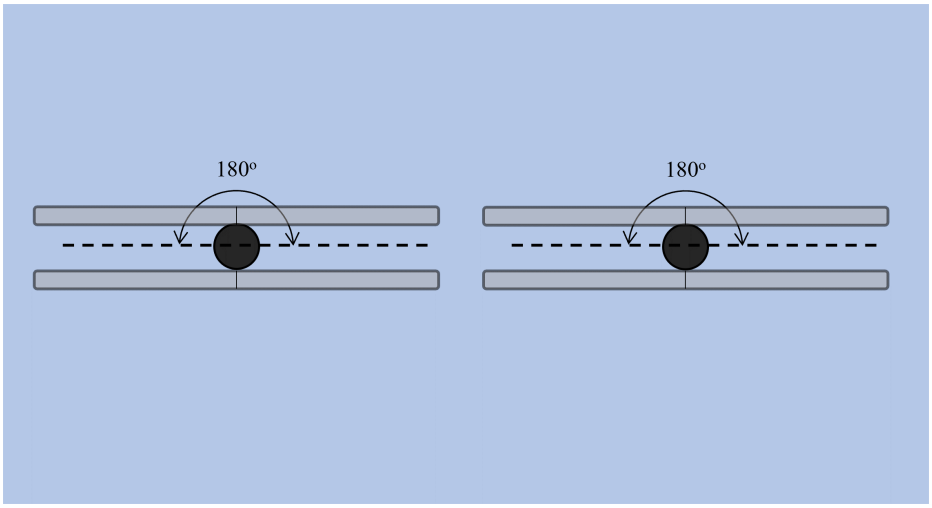

Figure 3.6: Illustration of the 180°-flapping mode. The figure shows the wings and rods as seen from above. The arrows illustrates that the rod rotates 180°, and the wings are shown at the two extreme points in the rotation.

3.1.3 Mode testing

The modes described in subsection 3.1.2 had to be tested with varying parameters to see if there is a set of modes and parameters that gave turbulent flow with varying intensity and integral length scale. The parameters that were tested are shown in Table 3.1. The initial testing was done by doing 10 minute LDV-measurements upstream at the center of the channel on 50% pump power. The results of the experiments in the project thesis showed that the velocity variance $\langle u_1^2 \rangle$ and the integral length scale $\bar{\ell}$ both converge for an 8 minute time series, but to be on the safe side we decided on doing 10 minute time series. The testing was done upstream so that there were little dissipation of the turbulence. The test were run on 50% pump power, as that was what the final experiments were initially planned to be ran on.

Mode	Angular velocity (rev/s)	Angular acceleration (rev/s^2)	Time between direction change (s)
Static	-	-	-
Spinning	$[0.5, 1.0]$	$[1.0, 5.0]$	$[5.0, 20.0]$
Spinning	$[0.05, 0.2]$	$[1.0, 5.0]$	$[5.0, 20.0]$
60°-flapping	6	6	$[0.1, 0.5]$
60°-flapping	1.2	6	$[1.0, 5.0]$
180°-flapping	6	6	$[0.5, 1.5]$
180°-flapping	1.2	6	$[3.0, 8.0]$

Table 3.1: The parameters used when testing the different modes.

The results of the initial testing are shown in Figure 3.7. These results show that the modes do

give clear differences in both turbulence intensity and integral length scale. It was decided from this that the modes that would be used in the final experiments are: spinning (fast), 60°-flapping (fast), and static. The 180°-flapping mode was deemed qualitatively to be blocking the flow too much, giving turbulent flow that is not statistically stationary.

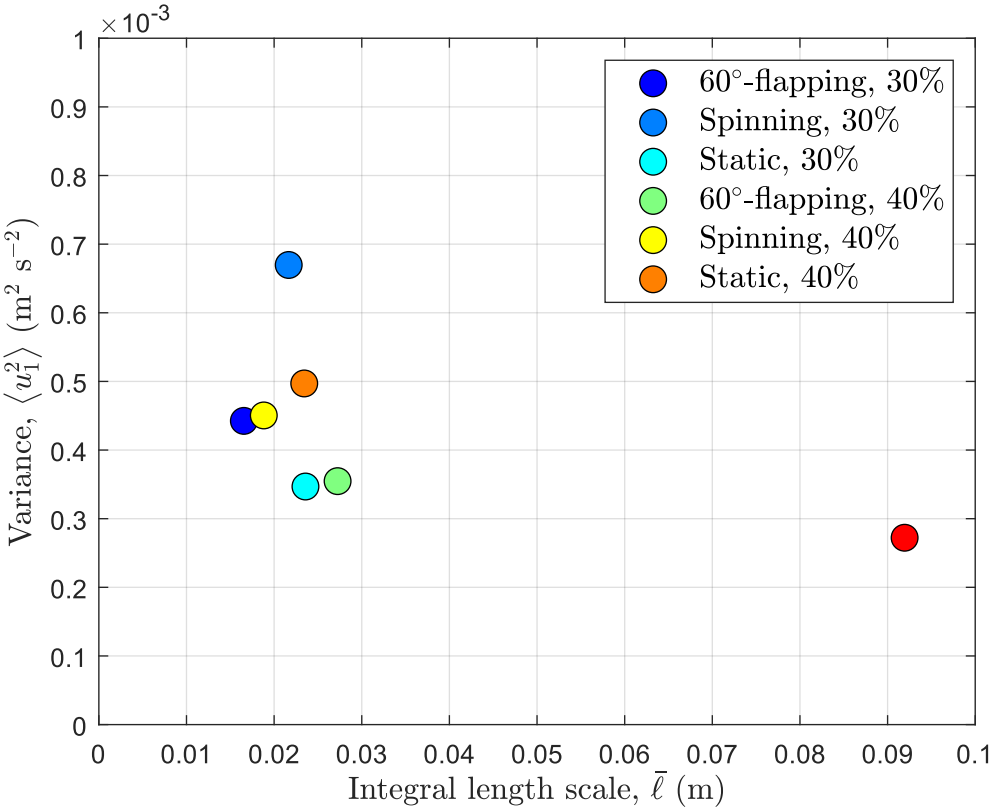

Figure 3.7: This is a ($\langle u_1^2 \rangle$,$\bar{\ell}$)-plot showing the results of the initial test of the set of modes and parameters in Table 3.1.

After the initial tests were conducted it was found out that 50% pump power gave bad Schlieren-measurements, which is used in Løvvig, 2023. The results in Løvvig, 2023 use the results from the experiments in this thesis, which meant that the final experiments had to be conducted at lower pump power. New tests were then conducted at 40% and 30% pump power for the three modes which were selected for the final experiments, to verify that they still gave varying turbulence intensity and integral length scale.

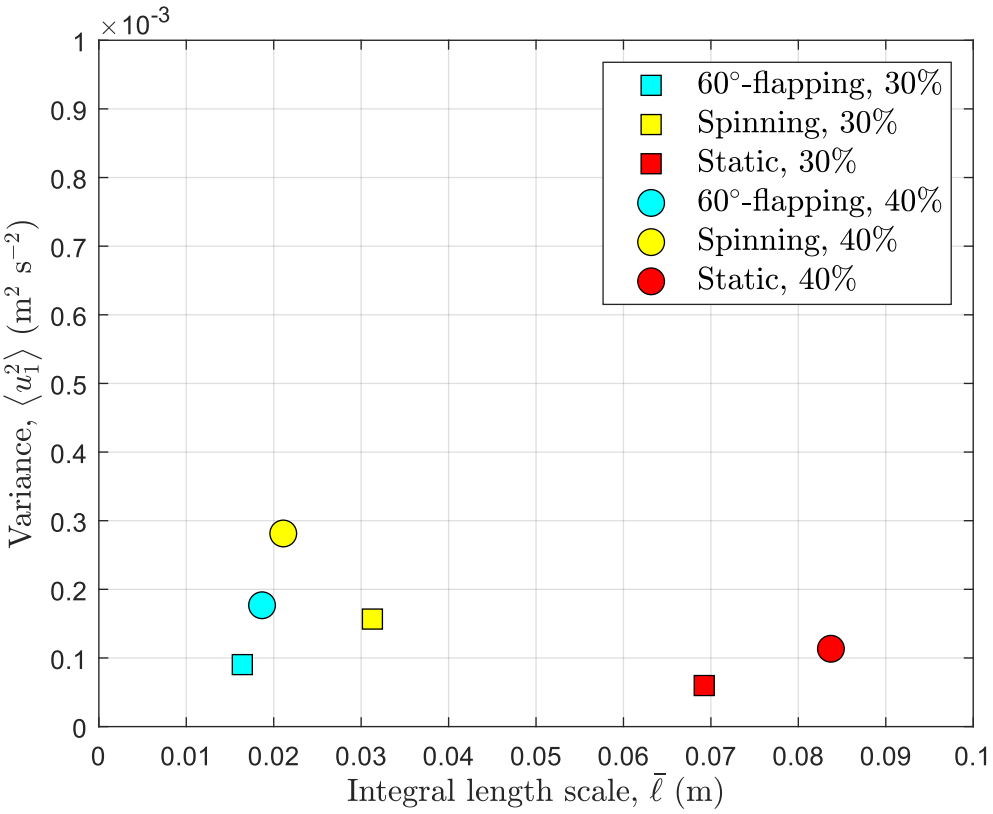

Figure 3.8: This is a ($\langle u_1^2 \rangle$,$\bar{\ell}$)-plot showing the results of the tests for the selected modes for the final experiment, at 40% and 30% pump power.

The results from these tests are shown in Figure 3.8. They show that the different modes still give clearly varying turbulence intensity and integral length scale at lower pump power (i.e., lower mean velocity).

3.2 Laser Doppler Velocimetry

Laser Dopppler Velocimetry (LDV) is a method for measuring instantaneous velocities at a single point without affecting the velocity. The working principle of LDV is that light that scatters from a moving particle will experience a Doppler shift, and how much the light is shifted is decided by the velocity of the particle.

Figure 3.9 is an illustration of a LDV-system. The two blue dotted lines illustrates the lase beams shot out from the LDV-probe. When a particle pass through the cross section of the two beams, shifted laser light will scatter. Some of the scattered light will reflect back to the probe, as illustrated by the red solid arrow. A receiver in the probe measures the frequency of the reflected light, and then the shift in frequency from the sent lasers to the received laser is used to calculate the velocity component U_1 of the particle, illustrated by the gray dot. Exactly how the velocity is calculated is thoroughly explained in Albrecht et al., 2003.

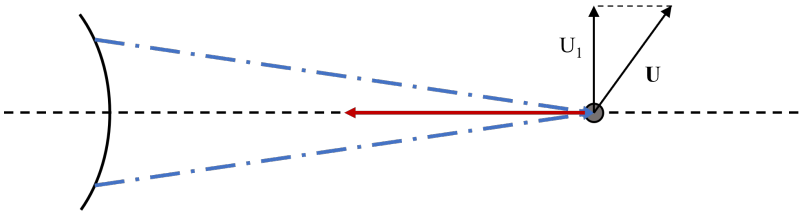

Figure 3.9: Illustration of a LDV-system. The blue dotted lines illustrate the two laser beams shot out from the LDV-probe. The red arrow is the shifted laser light reflected back to the LDV-probe. **U** signifies the velocity of the particle, and U_1 is the velocity component in the direction the LDV-system can measure.

3.2.1 Estimation of moments

An important feature of LDV-data is that the short term rate of random particle arrivals will generally be correlated with the measured flow quantity (Albrecht et al., 2003). This is referred to as the *particle-rate/velocity correlation*.

The particle rate through the measurement volume is determined by the volume flux of fluid through it, and this is, in general, correlated with the measured velocity component (Albrecht et al., 2003). Because of this, higher velocity will give higher sample rate, which means that for a given observation, higher velocities will be sampled more frequently than lower velocities. A simple arithmetic mean of all samples will therefore be positively biased (Albrecht et al., 2003).

This is why the estimates of the mean velocity $\langle U \rangle$ and the velocity variance $\langle u^2 \rangle$, presented in subsection 2.4.2 with Equation 2.23 and Equation 2.26 respectively, both have a weighting factor g_i. Albrecht et al., 2003, propose several possible weighting factors, and the one used in this thesis is the residence time of the particle

$$g_i = \tau_i, \tag{3.1}$$

where τ_i is the residence time of a particle. This can be used since the residence time is inversely proportional to the vector velocity magnitude (Buchhave, 1976).

3.2.2 Reconstruction and re-sampling

As mentioned above, an LDV-system measures the instantaneous velocity of a particle passing through the lasers. This means that velocity measurements are only made when particles are passing through, which happens at random time intervals. The LDV-data does therefore not have a constant sample frequency. This is a requirement for doing some of the statistical calculations described in section 2.4 (e.g., the autocorrelation function $\rho(s)$). This means that the data must be reconstructed and re-sampled to be able to perform these calculations.

The reconstruction method used in this thesis is the zeroth-order sample-and-hold scheme (S+H), as presented by Albrecht et al., 2003. It can be written as

$$U^{(\mathrm{SH})}(t) = U(t_i) \quad \text{for} \quad t_i \leq t < t_{i+1} \quad \text{and} \quad i = 1, ..., N, \tag{3.2}$$

where N is the total number of samples in the time series. The equidistant re-sampling with time steps of Δt_s is performed by

$$U_i^{(\mathrm{SH})} = U^{(\mathrm{SH})}(i\Delta t_s) \quad \text{for} \quad i = 0, ..., N_R - 1, \tag{3.3}$$

and leads to a data set of N_R samples. The re-sampling time step has been set to $\Delta t_s = T/2N$, where T is the length of the time series. This means that the re-sampling is done at twice the average sample rate of the original time series. Figure 3.10 shows the re-sampling of some of the turbulent velocity data from one of the experiments in this thesis. The red dashed line is the reconstructed velocity $U^{(\mathrm{SH})}(t)$, and the black crosses is the re-sampled velocity data $U_i^{(\mathrm{SH})}$.

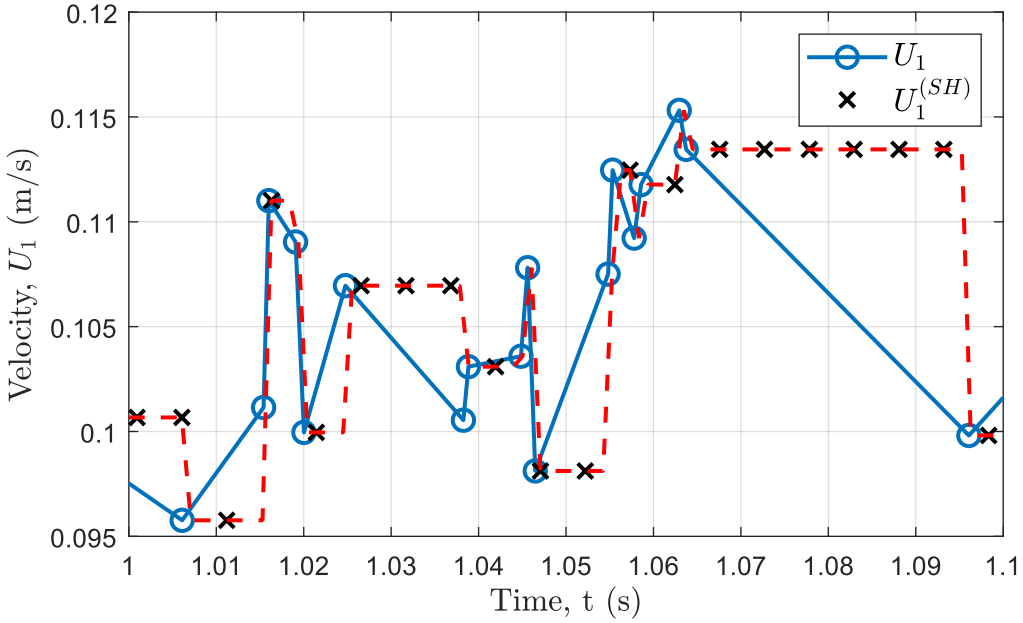

Figure 3.10: S+H for a small part of a time series from this thesis. The blue circles are the velocities measured by the LDV. The red dashed line is the reconstructed velocity, and the black crosses are the re-sampled data. This time series is from the 1st measurement of the spin mode at 40% pump power, upstream, 3cm left of the center looking from the active grid.

The S+H reconstruction brings some issues to the estimators of the frequency spectrum and and the autocorrelation function. Albrecht et al., 2003, mentions the work of Adrian and Yao, 1986, as a major step forward in understanding the fundamental content of a sample-and-hold reconstructed signal. One of the things they bring to focus is the noise from the step-like jumps in the S+H signal. This noise contribution decays with the inverse of the third power of the data rate $\dot{N}^{-3}$. Another factor in S+H reconstruction is a first-order, low-pass filter, acting on both the true spectrum and the step noise. The cut-off frequency of this filter is $\dot{N}/2\pi$.

Adrian and Yao, 1986, simulated laser Doppler data from a white noise process, and submitted it to a S+H reconstruction, re-sampling, and a conventional Fast Fourier Transform (FFT) Power Spectral Density (PSD) estimation. The results showed clear effects of both the step noise and the filter at low particle rates. Their conclusion was that such spectra are only reliable up to a frequency of $\dot{N}/2\pi$.

3.3 Signal processing

3.3.1 Windowing

The velocity measured is in reality a continuous function of time $U(t)$, spanning indefinitely. The measurements are though done over a finite duration T. The sharp cut-offs at the start and end of the measurements are equivalent to multiplying the continuous function $U(t)$ with a *window function* that is 1 for the time interval the measurements are done, and zero outside

$$U_{\text{measured}}(t) = U(t)w(t), \tag{3.4}$$

where

$$w(t) = \begin{cases} 1, & \text{if} \quad t_0 \leq t \leq t_0 + T \\ 0, & \text{else} \end{cases} \quad . \tag{3.5}$$

Here t_0 is the time at the start of the measurement. This leads to *spectral leakage*, meaning that the temporal effects of the sample window becomes visible in the Fourier transform (Lyon, 2009).

A way to reduce these effects is to use other window functions with smoother transitions to outside the measurement interval. The windowing function used in this thesis is the Hann window function, illustrated in Figure 3.11, which is a compromise between suppressing the long-range spectral leakage and blurring the spectrum (Nuttall, 1981). The Hann window is defined as

$$w_{\text{Hann}}(t) = \begin{cases} 0.5 - 0.5\cos(2\pi t/T), & \text{if} \quad t_0 \leq t \leq t_0 + T \\ 0, & \text{else} \end{cases} \quad . \tag{3.6}$$

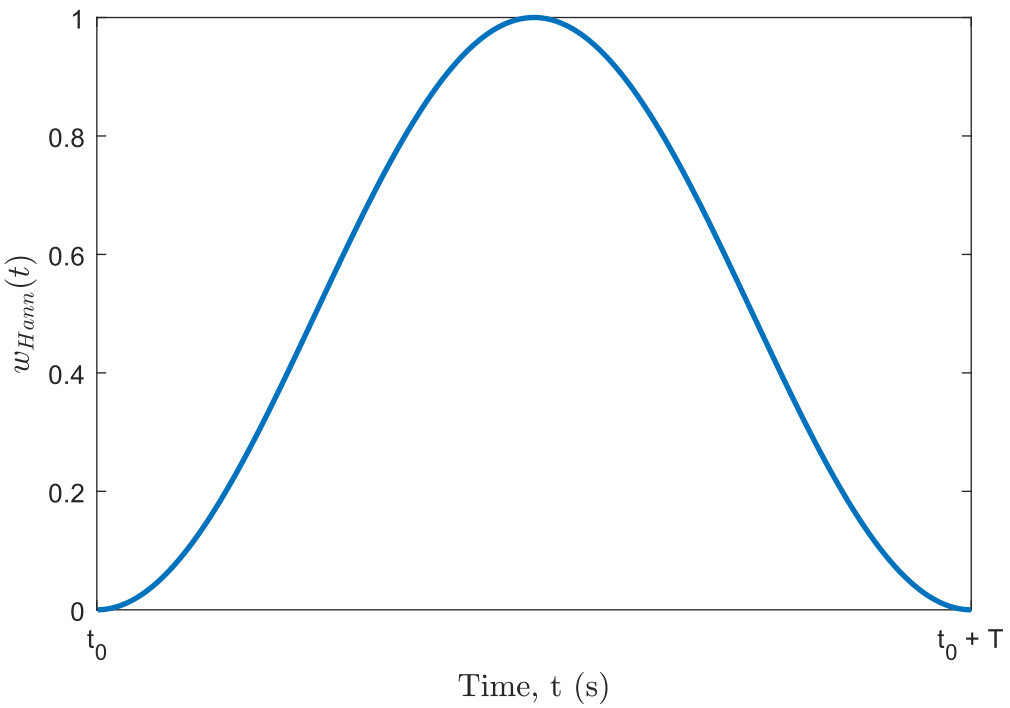

Figure 3.11: The Hann window function plotted from t_0 to $t_0 + T$.

3.3.2 Block averaging

Albrecht et al., 2003, introduce block averaging as a way to reduce the variance in the estimated PSD and autocorrelation function. Block averaging means that the time series is divided into N_B blocks, where the PSD and autocorrelation function is estimated individually for each block, and then they are averaged. The effects of block averaging are shown in Figure 3.12. It reduces the resolution for the smallest wavenumbers, but it also reduces the noise for the larger wavenumbers, making the Energy spectrum easier to read and compare between the various experiments.

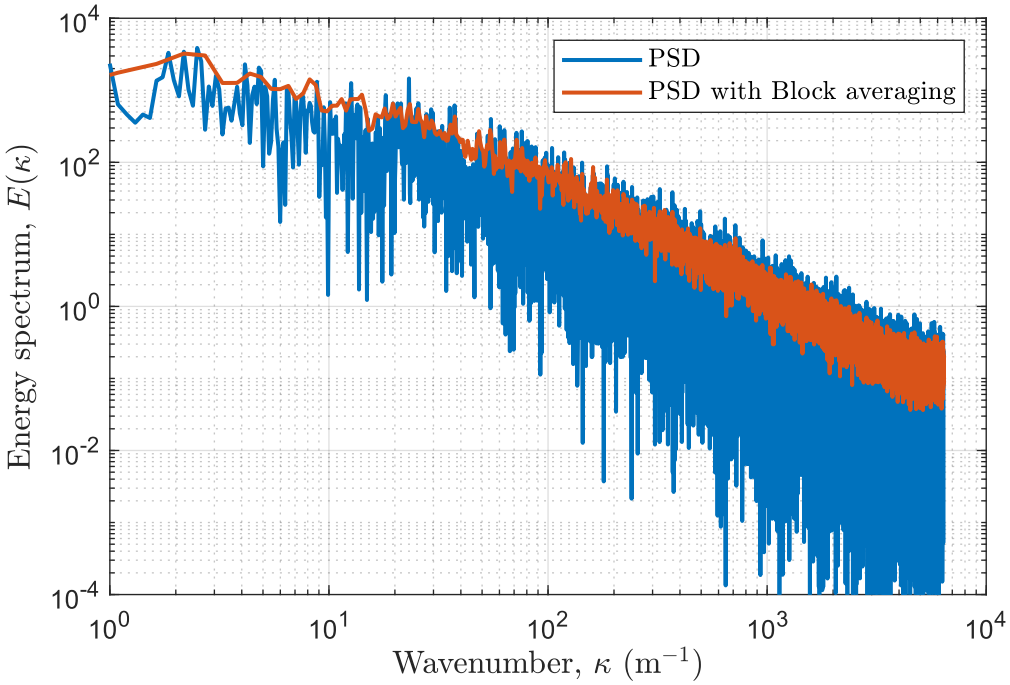

Figure 3.12: This shows the PSD calculated with and without block averaging. This time series is from the 1st measurement of the spin mode at 40% pump power, upstream, 3cm left of the center looking from the active grid.

The block averaging method used in this thesis is illustrated in Figure 3.13. The time series is divided into 9 equally long blocks, where each block overlaps 50% with the block next to it.

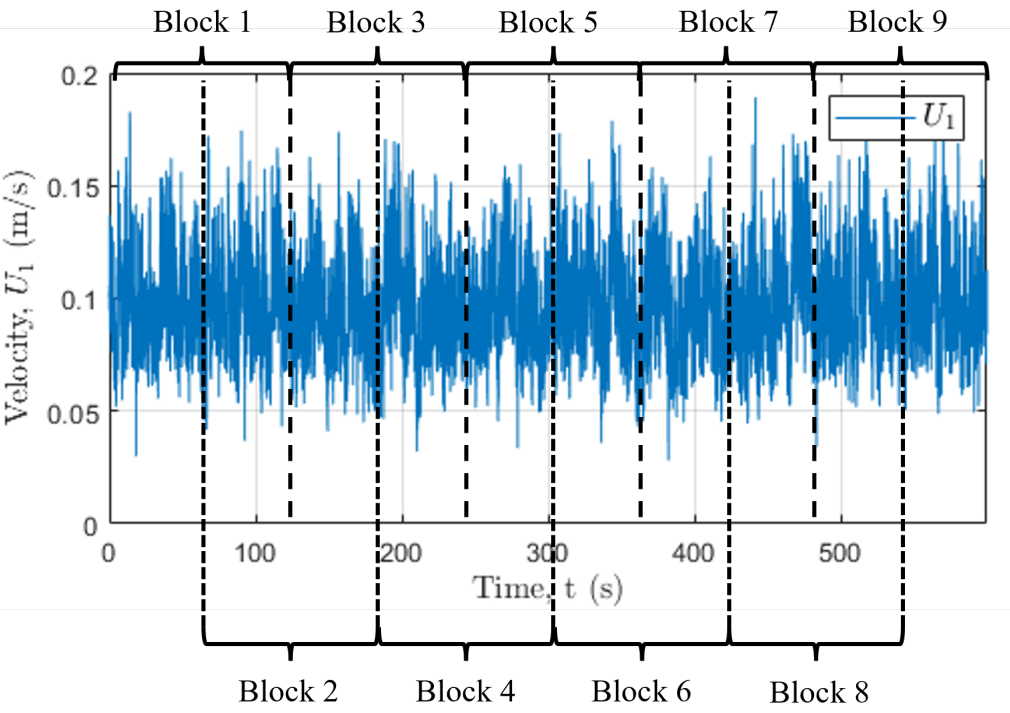

Figure 3.13: Illustration of how the time series in this thesis are divided into 9 blocks when calculating the PSD of the time series. This time series is from the 1st measurement of the flapping mode at 40% pump power, upstream, 3cm left of the center looking from the active grid.

3.4 Signal decomposition

The velocity signal from the experiments with surface waves contain contributions from the mean flow, wave motion, and turbulence

$$U = \langle U \rangle + u + \tilde{u}, \tag{3.7}$$

where $\tilde{u}$ is the wave motion (Hussain and W. C. Reynolds, 1970). It is necessary to remove the wave motion component to be able to compare the experiments with waves to those without. There have been developed methods to decompose such signals, and the one used in this thesis is *empirical mode decomposition* (EMD).

3.4.1 Empirical mode decomposition

EMD has been applied successfully in fluid mechanics by, among some, Qiao et al., 2016, who study wave-turbulence properties at the ocean surface, and Peruzzi et al., 2021 who study the influence of collinear surface waves on turbulence in open-channel flows. It is especially the work in Peruzzi et al., 2021, that motivated the use of EMD in this thesis.

The basic functions of EMD are directly inferred from the data itself, as opposed to most other methods. This means that no signal features are assumed beforehand. A drawback, however, is that it is fully empirical and no rigorous mathematical foundation has yet been derived. Nevertheless, the EMD procedure satisfies the perfect reconstruction property, meaning that the original signal can be completely reconstructed by summing all the functions inferred from it. These functions are reffered to as *intrinsic mode functions* (IMFs), and represent the natural oscillatory modes that are embedded in the signal (Peruzzi et al., 2021).

The IMFs are extracted from the signal by the means of a sifting process (Norden E. Huang, Z. Shen, Long et al., 1998, Norden E. Huang, Z. Shen and Long, 1999, and Norden E Huang et al., 2003). It is an iterative process, and Rato et al., 2008, explains it with the following steps:

1. Find all the local maxima M_i, $i = 1, 2, ...$, and minima, m_k, $k = 1, 2, ...$, in $u(t) = U(t) - \langle U \rangle$.
2. Compute the corresponding interpolating signals $M(t) = f_M(M_i, t)$, and $m(t) = f_m(m_k, t)$. These signals are the upper and lower envelopes of the signal.
3. Let $e(t) = (M(t) + m(t))/2$.
4. Subtract $e(t)$ from the signal: $u(t) = u(t) - e(t)$.
5. Return to step 1. Stop when $u(t)$ remains nearly unchanged.
6. Once we obtain an IMF, $\phi(t)$, remove it from the signal $u(t) = u(t) - \phi(t)$ and return to step 1 if $u(t)$ has more than one extremum.

The *emd* function in MATLAB was used to extract the IMFs in this thesis, which as default uses cubic spline as the interpolating functions f_M and f_m.

The experiments only ran the wavemaker for time intervals of 90 seconds, since there would be too many reflected waves if it ran any longer. The time between each run of the wavemaker was 5 minutes so that the waves would have died out before each new run. Where in the time series the wavemaker is generating waves is illustrated in Figure 3.14.

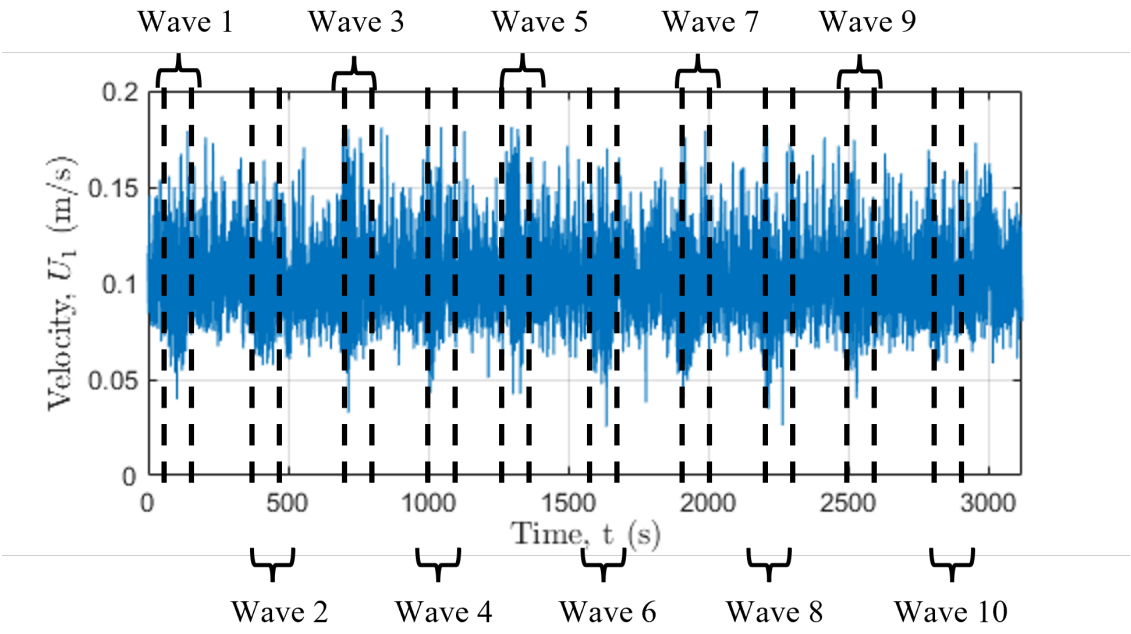

Figure 3.14: An illustration of where in the time series the wavemaker is generating waves.

This means that the time intervals with waves have to be extracted from the data before the EMD could be performed. The data from the first time interval with waves, named as Wave 1 in Figure 3.14, is shown in Figure 3.15. I have been conservative when slicing the time series, only using 40 seconds of the 90 with wave generation, to ensure that the data has as regular and monochromatic waves as possible. This does give a smaller data set, making the statistical quantities more uncertain, but it gives a better decomposition of the signal.

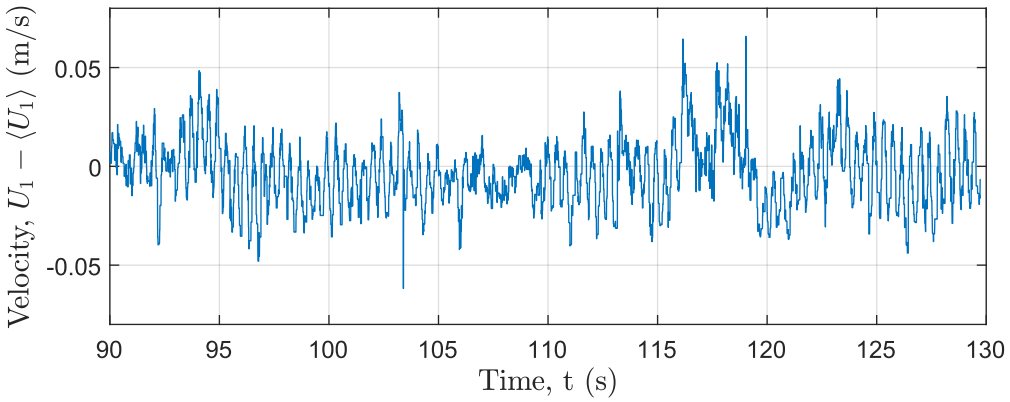

(a) The original signal with the mean flow component $\langle U \rangle$ removed.

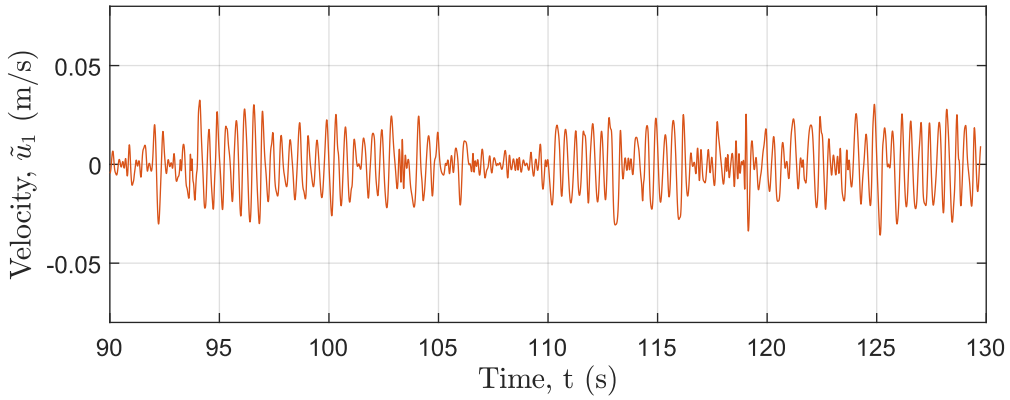

(b) The wave component $\tilde{u}$ of the signal.

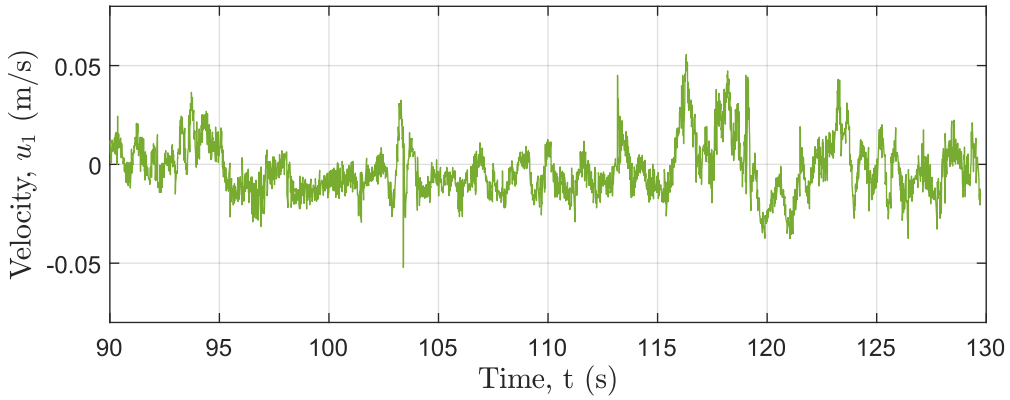

(c) The turbulent component u of the signal.

Figure 3.15: The signal from Wave 1 in Figure 3.14 decomposed into its wave component $\tilde{u}$ and turbulent component u.

As clearly visible in Figure 3.16, the EMD and removal of the wave component creates an artificial valley in the PSD, which is similar to what Peruzzi et al., 2021, experienced with their signal. This happens because turbulent motion with similar frequencies as the wave motion is associated with the wave component instead of the turbulent component. Peruzzi et al., 2021 did an estimation of the loss of total spectral energy this caused, and they estimated that the loss was of 20% - 30% for the longitudinal velocity.

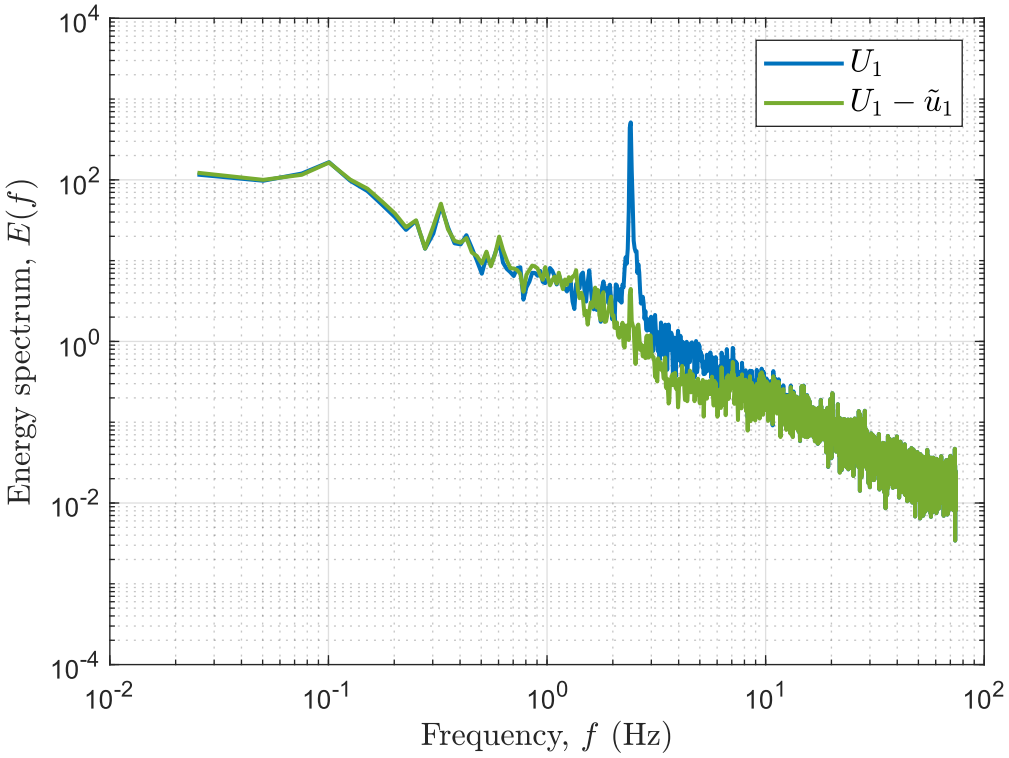

Figure 3.16: The PSD of the signal from Wave 1 in Figure 3.14 and of its turbulent component u, shown in Figure 3.15.

3.5 Noise removal

3.5.1 Zero-noise

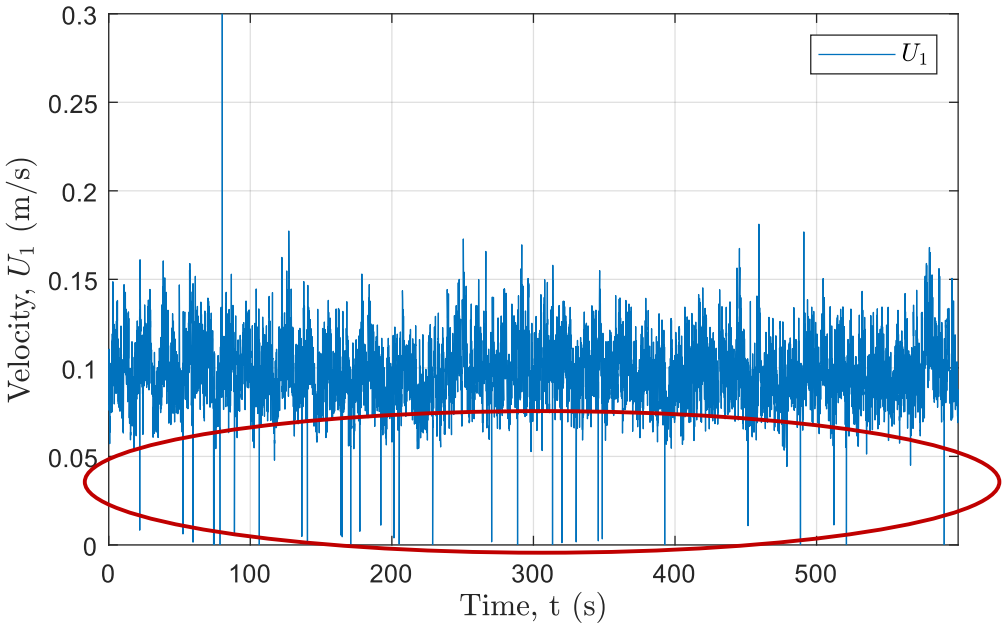

Figure 3.17: This highlights LDV-data which is centered around zero, deviating significantly from the mean flow. It is highlighted by the red circle. This time series is from the 1st measurement of the flapping mode at 40% pump power, upstream, 3cm left of the center looking from the active grid.

The LDV-data in the experiments in this thesis and in the project thesis all contain samples with velocity around zero, as highlighted by the red circle in Figure 3.17. In Figure 3.18 we see the time series zoomed in at two of these samples, and it clearly shows that these samples are not coherent with those around them. Given the description of turbulent flows in subsection 2.1.1, this seems unphysical, and these samples have therefore been filtered when calculating the results.

The filtering of these results have been done by removing all samples under 0.02m/s.

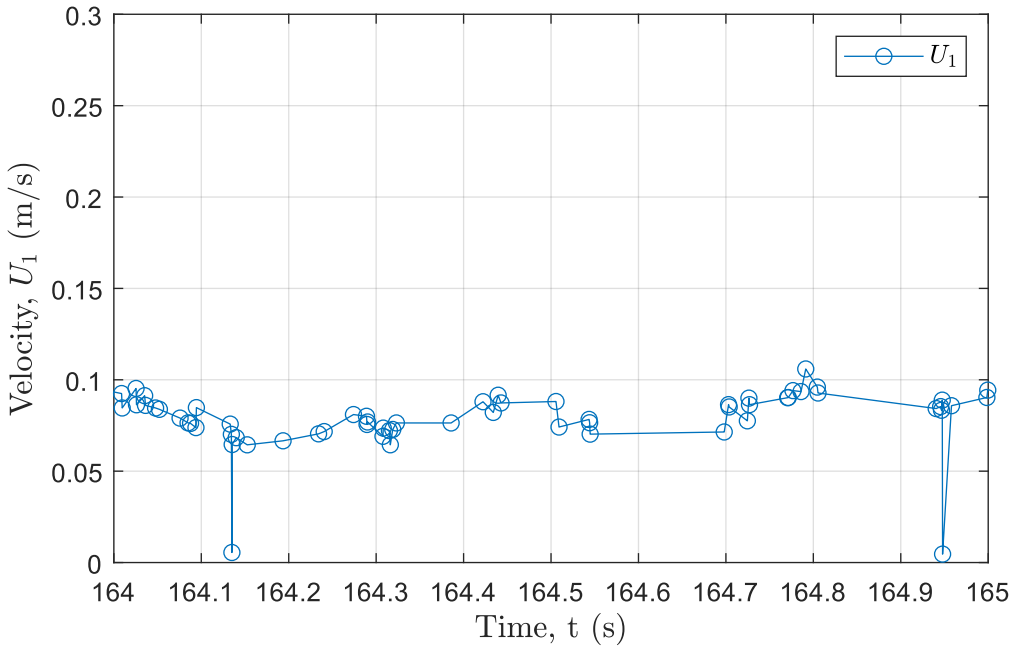

Figure 3.18: This shows the same time series as in Figure 3.17, but zoomed in on two of the highlighted samples to get a closer look on what they look like compared to the neighbouring samples. This time series is from the 1st measurement of the flapping mode at 40% pump power, upstream, 3cm left of the center looking from the active grid.

3.5.2 Removing outliers

There are also samples, other than the zero-noise ones, that seem unphysical, like the one highlighted by a red circle in Figure 3.19. In Figure 3.20 we see how this sample also looks not coherent with those around it. Such extreme values influence higher order moments heavily, which means longer time series would be needed for them to converge. These samples are therefore also filtered out when calculating results.

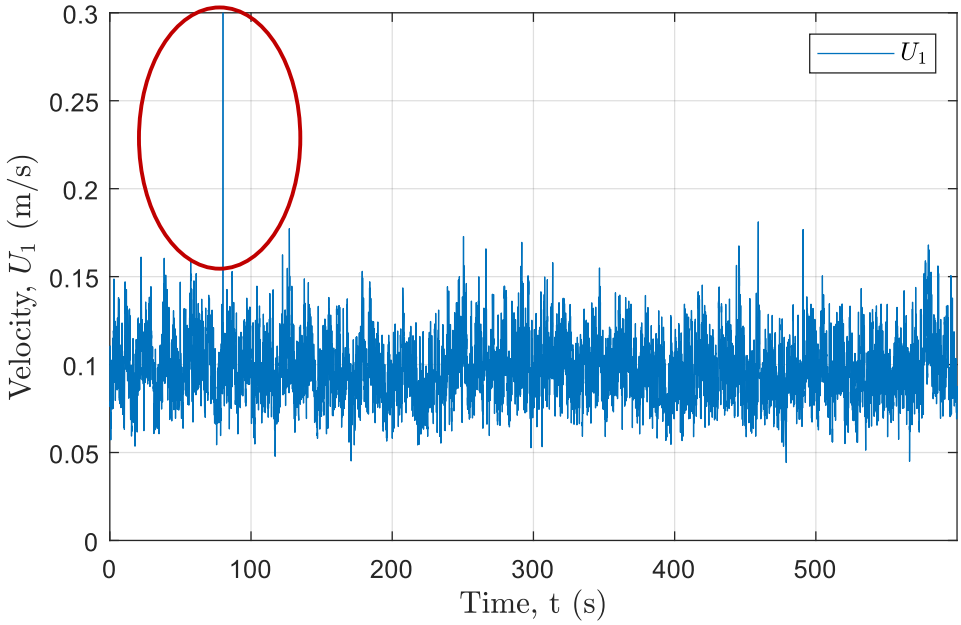

Figure 3.19: This highlights a sample deviating significantly from the mean flow. It is highlighted by the red circle. This time series is from the 1st measurement of the flapping mode at 40% pump power, upstream, 3cm left of the center looking from the active grid.

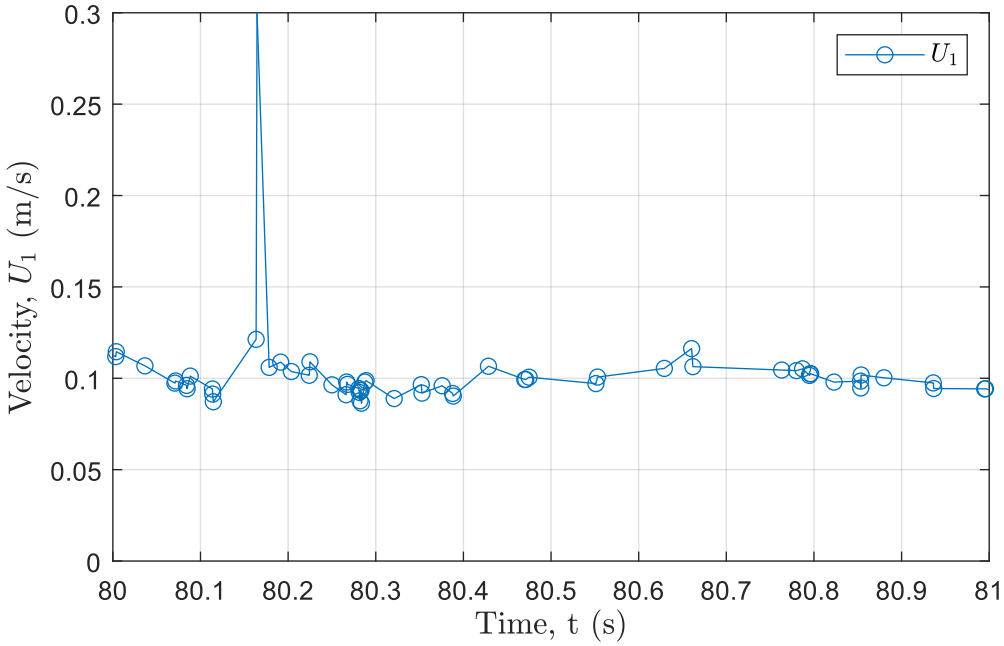

Figure 3.20: This shows data from the same time series as Figure 3.19, but zoomed in at the highlighted sample to get a closer look on what it looks like compared to neighbouring samples. This time series is from the 1st measurement of the flapping mode at 40% pump power, upstream, 3cm left of the center looking from the active grid.

One way to remove these samples is by removing samples outside a multiple N_{STD} of the standard deviation $\langle u \rangle$. Figure 3.21 show these filters on one of the time series in this thesis. We can clearly see that most of these filters also remove other samples than the one highlighted in Figure 3.19. This is also illustrated in Figure 3.22, which shows number of samples removed for each filter.

There seems to be a substantial number of samples removed up until $N_{\mathrm{STD}} = 3$, which means all up until that will clearly falsify the data. To be on the safer side, I have used $\langle U \rangle \pm 5 \langle u \rangle$ as the upper and lower bound for the samples in the experiments in this thesis.

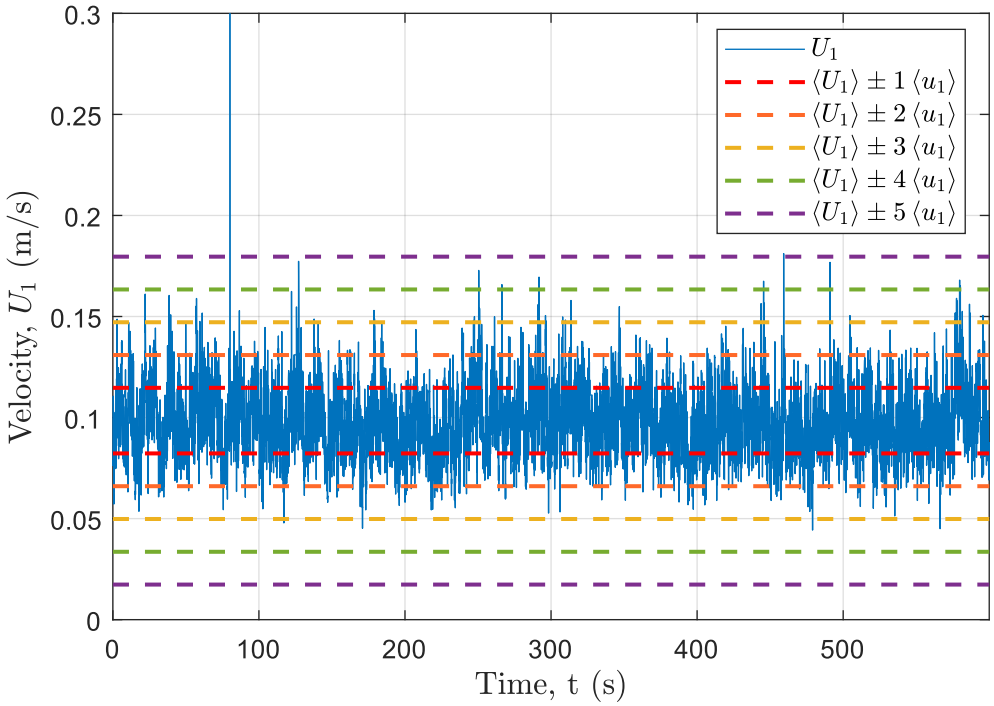

Figure 3.21: This shows $\langle U \rangle \pm N_{\mathrm{STD}} \langle u \rangle$ which is proposed as upper and lower bounds to filter out samples like the one highlighted in Figure 3.19. This time series is from the 1st measurement of the flapping mode at 40% pump power, upstream, 3cm left of the center looking from the active grid.

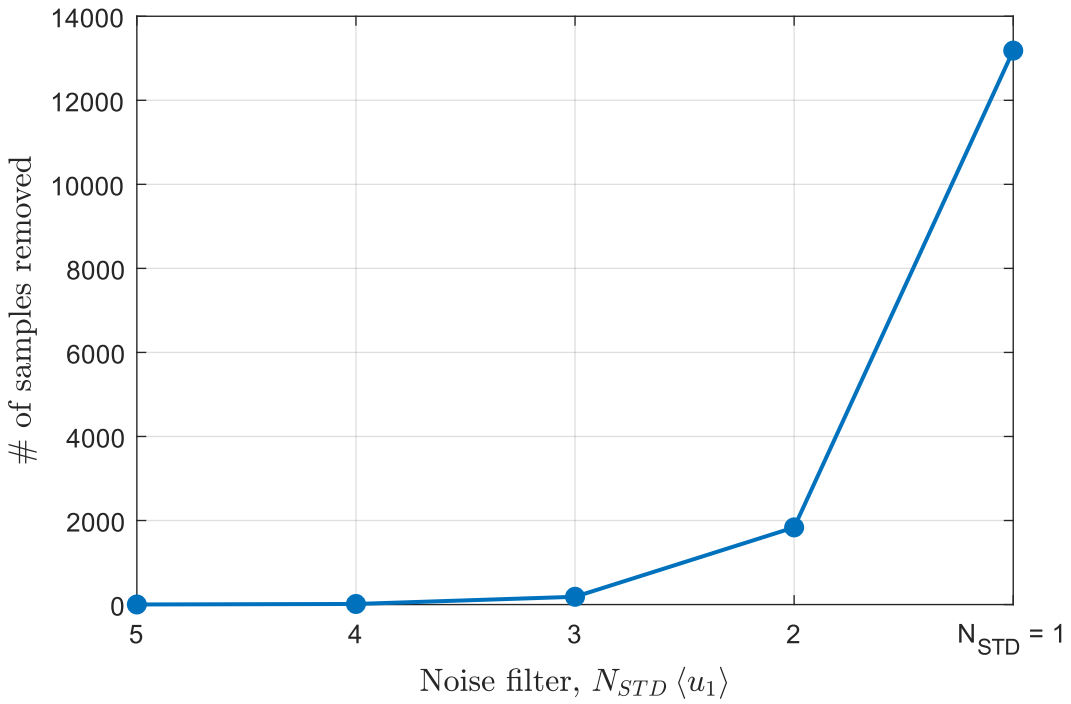

Figure 3.22: This shows the number of samples removed when applying the filters in Figure 3.21 to this time series. The total number of samples in this is 41998. This time series is from the 1st measurement of the flapping mode at 40% pump power, upstream, 3cm left of the center looking from the active grid.

3.6 Convergence testing

The turbulent flows in the experiments in this thesis are designed to be statistically stationary, meaning that you can use autocorrelation function and energy spectrum to characterize the flow, as discussed in subsection 2.4.3. To ensure that the flow is statistically stationary, it needs to be checked that the moments and the integral length scale converge towards single values.

Figure 3.23 shows convergence plots for mean velocity $\langle U \rangle$, velocity variance $\langle u^2 \rangle$, and integral length scales $\bar{\ell}$ and $\bar{\ell}_{McF}$, calculated using Equation 2.32 and Equation 2.33 respectively. The values in the plots are calculated by calculating the values using all the LDV-data up until the time at the x-axis.

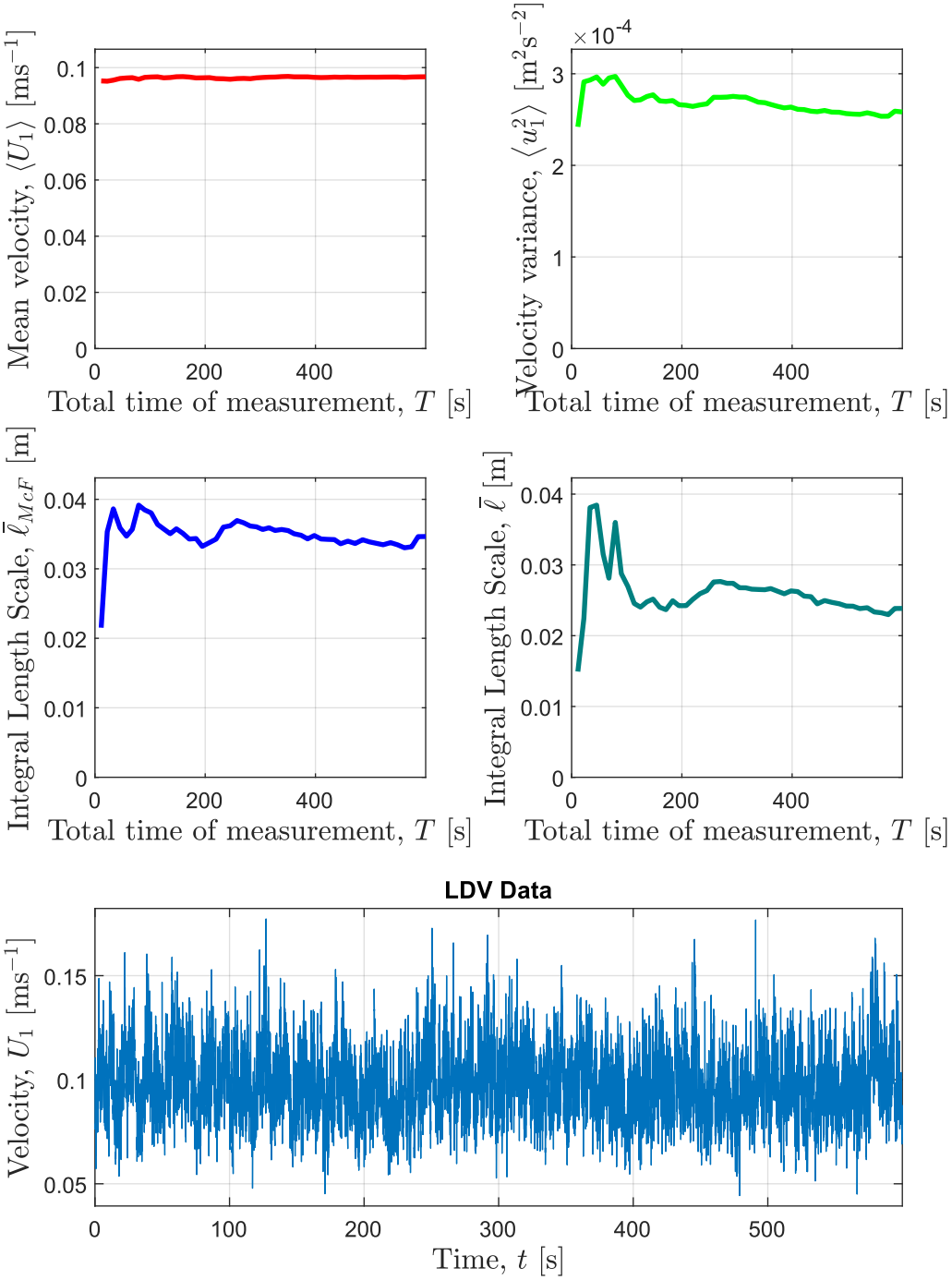

Figure 3.23: This is the display used to check convergence of the important parameters in the experiments in this thesis. The LDV-data is also shown to be able to what causes eventual jumps in any of the parameters. This time series is from the 1st measurement of the flapping mode at 40% pump power, upstream, 3cm left of the center looking from the active grid.

Chapter 4

Experimental setup

This chapter gives a description of the experimental setup used in this thesis, and of the various components involved. Figure 4.1 is an illustration of the complete setup, and Figure 4.2 is a photograph of the setup without the LDV-system.

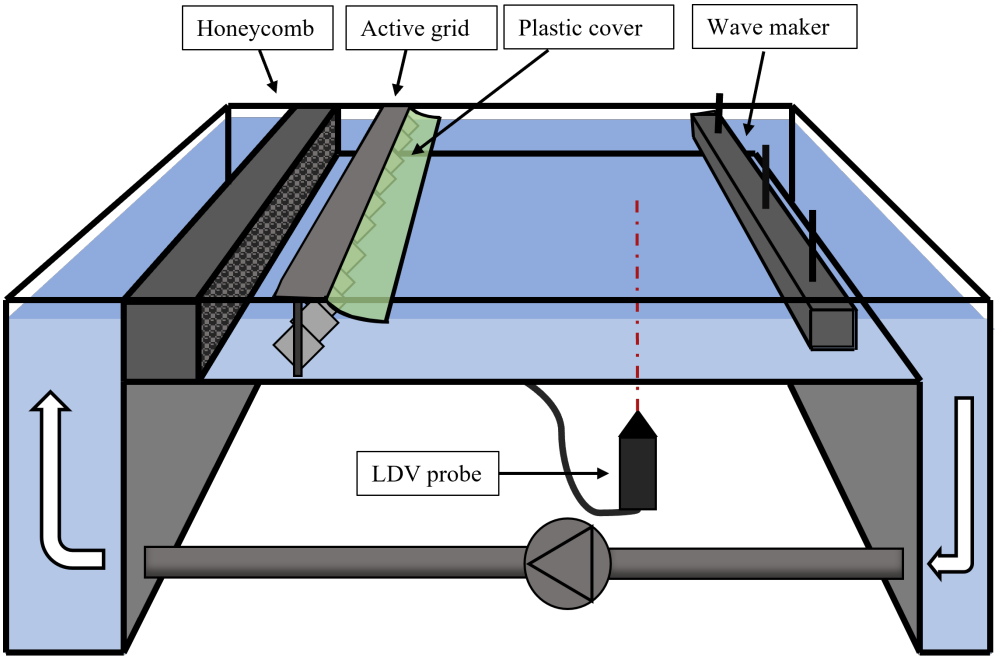

Figure 4.1: The experimental setup for this project. The water flows through the channel from left to right, and the water gets pumped back to the left side with a pump going under the channel, as shown by the white arrows.

The water channel contains the passive components, the honeycomb grid and the plastic cover, whose functions are to make the experiments repeatable by removing unwanted turbulence and waves. The channel also contains the active parts, the active grid and the wavemaker, whose functions are to generate controllable turbulence and waves to study the wave-turbulence interaction. The method for measuring the velocities of the channel flow is LDV.

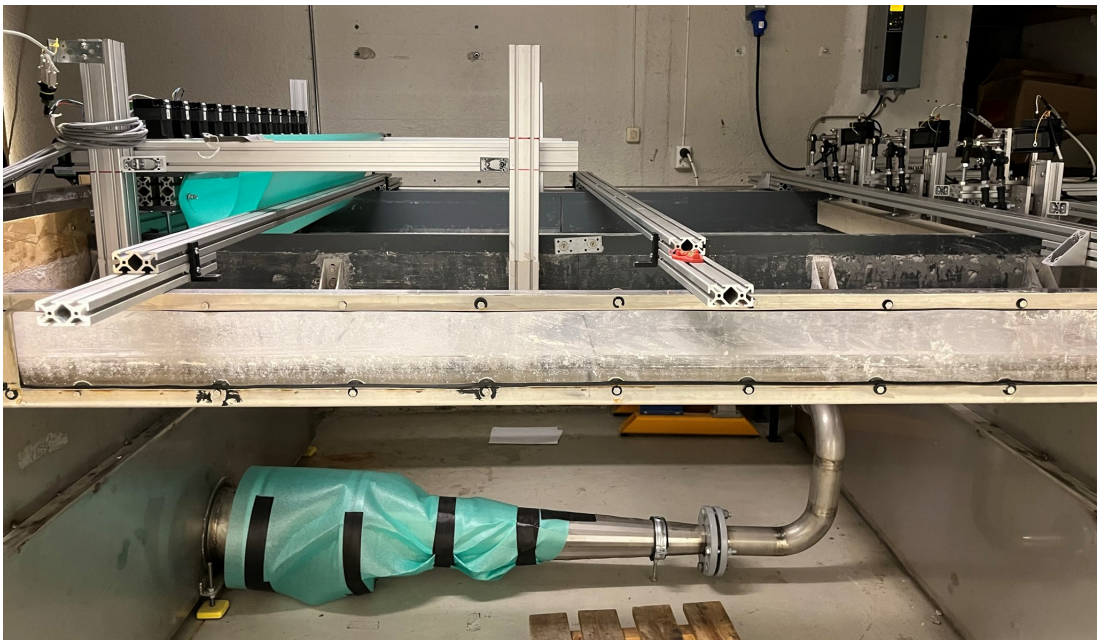

Figure 4.2: A photograph of the water channel from the perspective of Figure 4.1. The setup for the LDV-system was removed when this was taken

4.1 Water channel

4.1.1 Dimensions

The dimensions of the water channel is given in Figure 4.3. It shows the location of the different elements in the flow, like the honeycomb, the active grid, and the wavemaker. It also shows the 20 different points where LDV-measurements have been made.

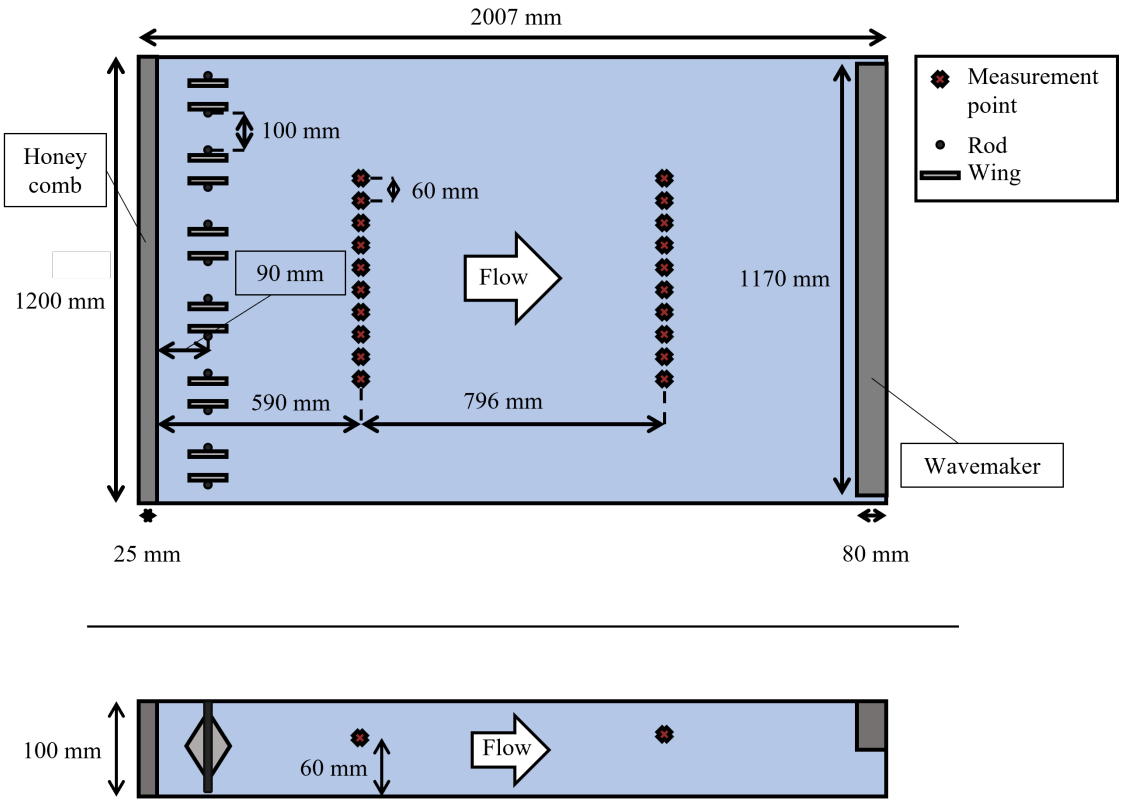

Figure 4.3: The dimensions of the water channel. The top part is the channel as seen from above, and the bottom part is as seen from the side. The flow is going from left to right, as shown by the white arrows. The symbol description is in the top right corner.

4.1.2 Side walls

Two side walls were mounted in the water tank, as highlighted in Figure 4.4. These serve several purposes for the experiments in this thesis. One is that they are smoother than the walls of the water tank, and therefore interfere less with the flow. Another is that there were a limited amount of stepper motors available for the active grid, and since the grid is designed to have no significant gaps, and the chosen wing design is square, the water channel had to be narrower than the width of the water tank.

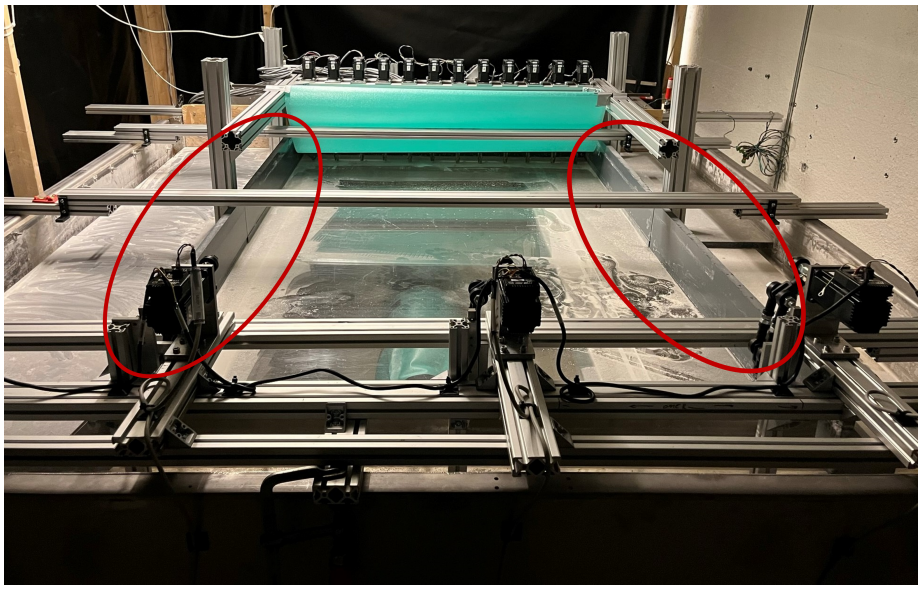

Figure 4.4: A picture of the water channel as seen from behind the wave maker. The side walls are highlighted by the two red circles.

4.1.3 Honeycomb

At the start of the water channel there is a honeycomb grid, as shown in Figure 4.5. The purpose of the honeycomb is to straighten out the flow so that it flows in only one direction before it hits the active grid. It covers the whole cross-sectional area of the water channel, and it is 2.5cm wide, as shown in Figure 4.3.

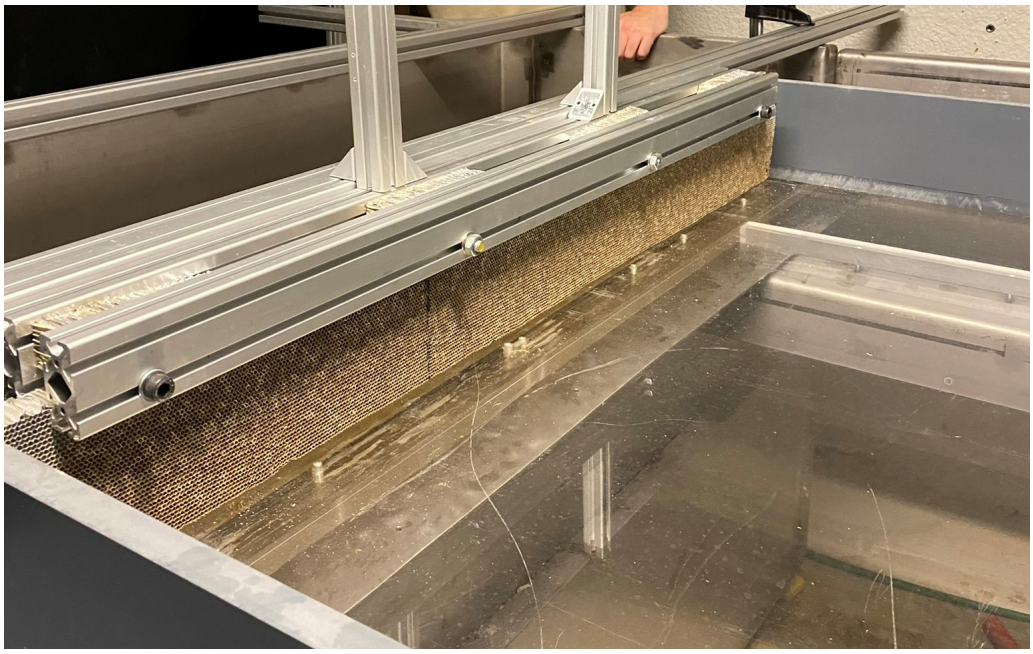

Figure 4.5: A picture of the honeycomb grid.

4.1.4 Plastic cover

A plastic cover is put on top of the water surface downstream of the active grid, as shown in Figure 4.1. It is highlighted by the red circle in Figure 4.6. The purpose of it is to dampen the surface waves generated by the motion of the wings in the active grid. Figure 4.7 shows a picture of these waves. Such waves would interact with the waves generated by the wavemaker, and that is not the interaction that is studied in this thesis.

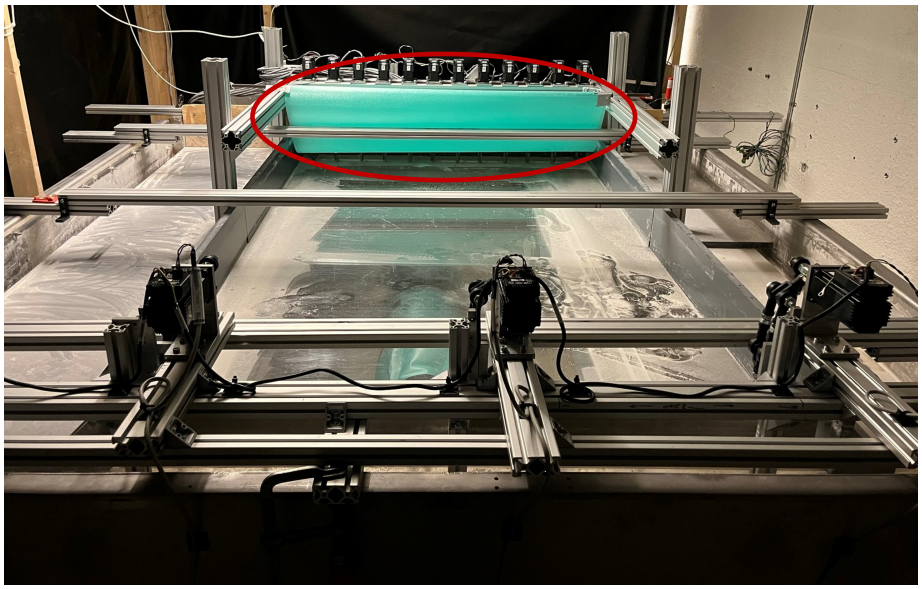

Figure 4.6: A picture of the water channel as seen from behind the wave maker. The plastic cover is highlighted by the red circle.

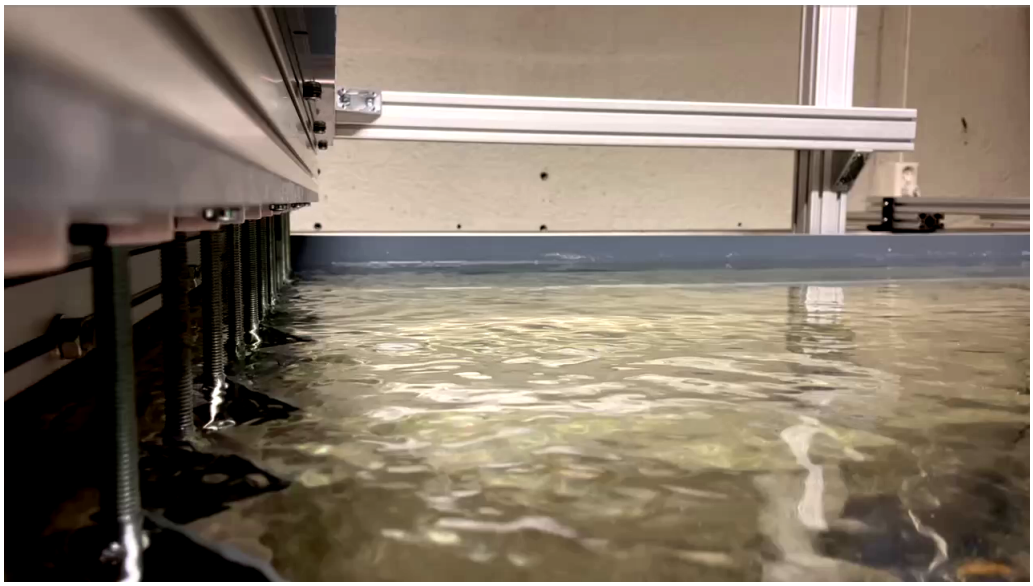

Figure 4.7: A picture of waves caused by the motion of the active grid.

An illustration of how the plastic cover is implemented in the experimental setup is shown in Figure 4.8. It is connected to the active grid, and it lays passively on top of the channel surface. It covers the whole width and 8.5cm of the length of the channel.

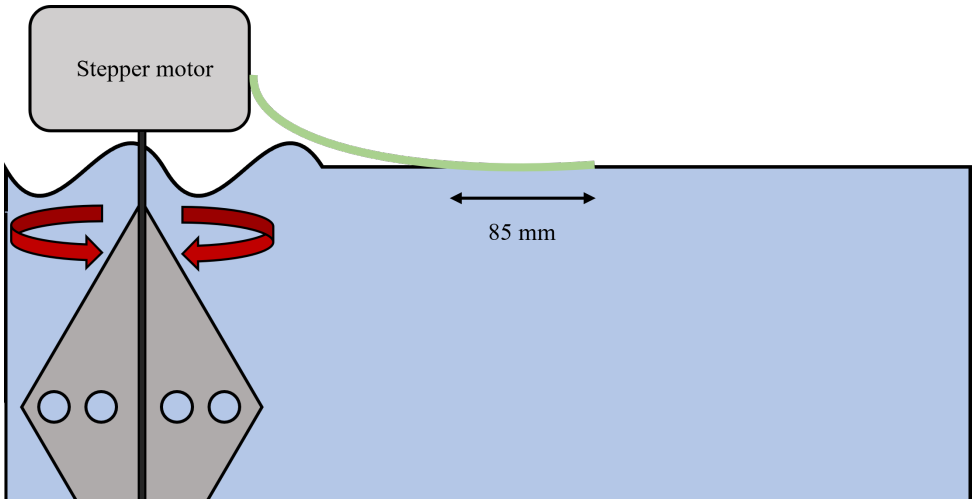

Figure 4.8: Plastic cover.

4.2 Active grid

An important part of the experimental setup in this thesis is the active grid. Figure 4.9 is a photograph of the active grid used in this these experiments. An illustration of it is also shown in Figure 3.2. It consist of twelve stepper motors that rotate rods which are connected to wings. It is the rotation of these wings that generate the turbulence.

Figure 4.9: A photograph of the active grid.

4.2.1 Wing dimensions

The dimensions of the wings in the active grid are shown in Figure 4.10. In subsection 3.1.1 an explanation of the design of them are made. The wings are made of hard plastic which is more pliable than most metals. They therefore had to be thicker than wings in active grids often are, so they would not bend while moving. A close up photograph of one of the wings are shown in Figure 4.11.

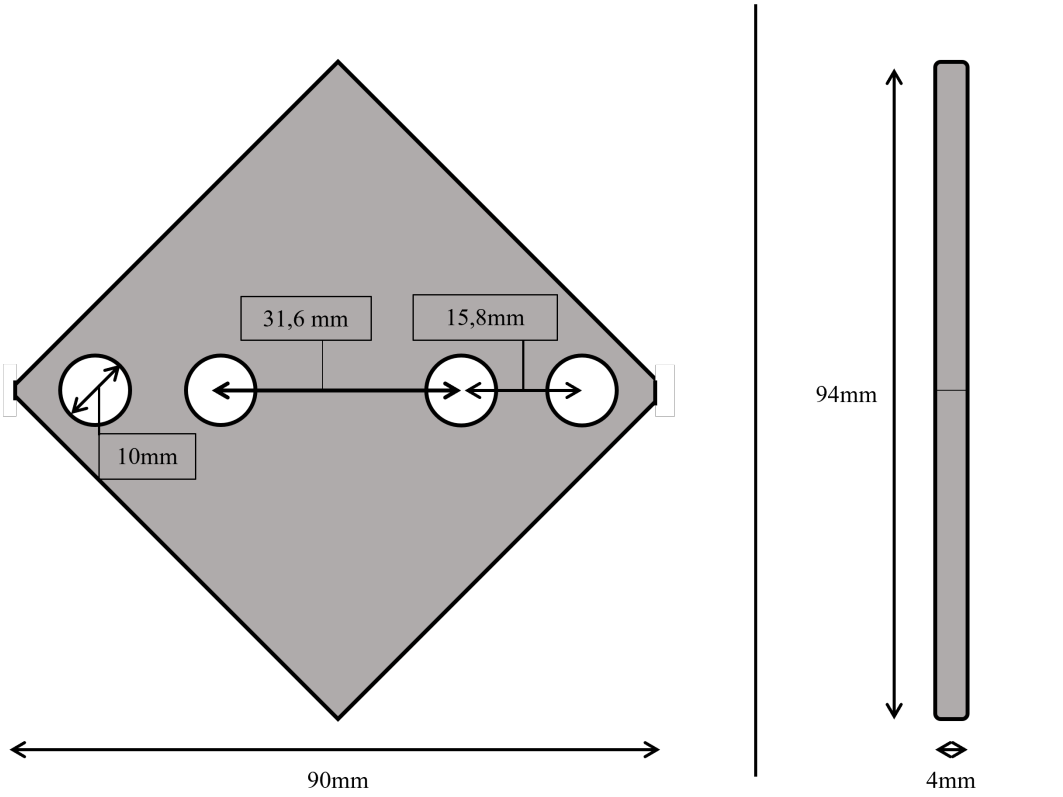

Figure 4.10: Design and dimensions of the wings. The left part is a front view of the wing, and the right part is the side view.

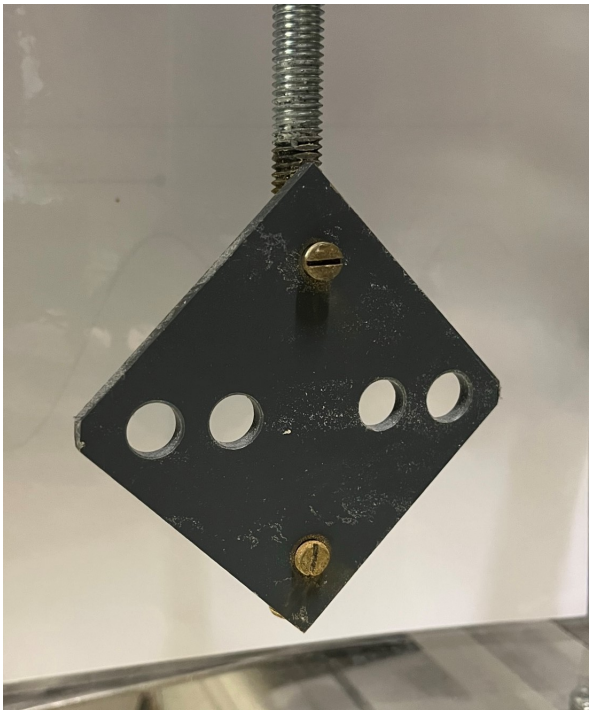

Figure 4.11: A photograph of one of the wings in the active grid.

4.2.2 Modes

The modes of the active grid is what generates the various turbulent flows studied in this thesis. A description of the different modes is given in subsection 3.1.1, and the reasoning for why we went for static, spinning, and 60°-flapping as the modes used in the final experiments is given in subsection 3.1.3. The parameters used in the final experiments are given in Table 4.1.

Mode	Angular velocity (rev/s)	Angular acceleration (rev/s^2)	Time between direction change (s)
Static	-	-	-
Spinning	$[0.5, 1.0]$	$[1.0, 5.0]$	$[5.0, 20.0]$
60°-flapping	6	6	$[0.1, 0.5]$

Table 4.1: The parameters used in the final experiments.

4.3 Wavemaker

When studying the interaction between turbulent flows and surface waves it is necessary to generate reproducible waves. In this thesis it is done with the wavemaker pictured in Figure 4.12.

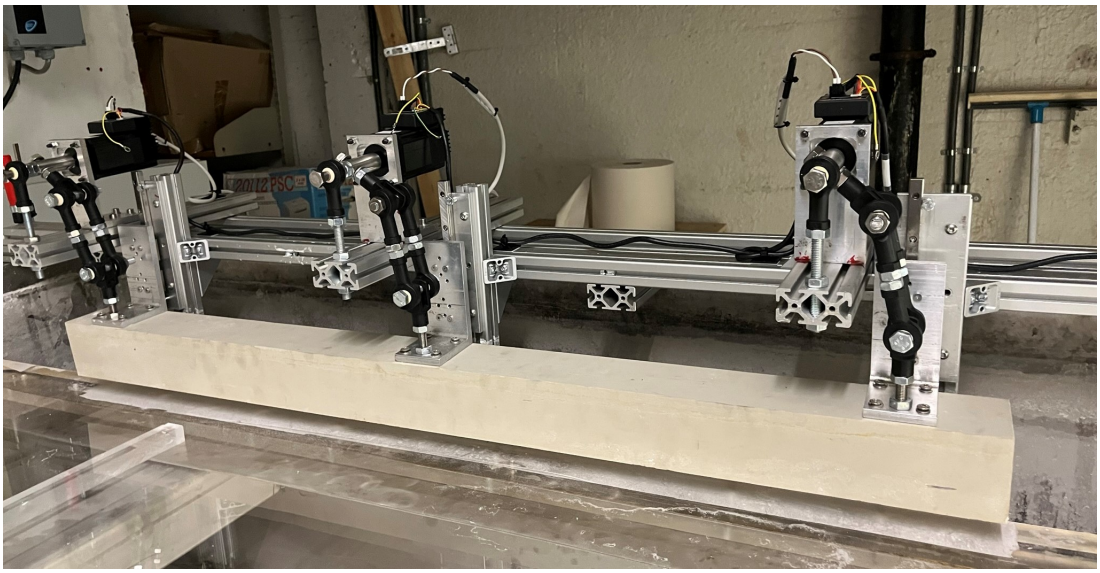

Figure 4.12: A photograph of the wavemaker.

The wavemaker consist of three stepper motors that simultaneously move a plank up and down at the end of the channel.

4.3.1 Stepper motors

The stepper motors are the active part of the wavemaker. They rotate back and forth simultaneously at a certain frequency. The angle they rotate decides the amplitude of the waves, and the frequency they rotate at decides the frequency of the waves. This means that frequency and amplitude are the parameters we can control. The parameters used for the stepper motors in the experiments are given in Table 4.2

Stepper motor parameters	
Frequency	2.4Hz
Amplitude	6°

Table 4.2: Specifications for the particles used in the water channel.

4.3.2 Plank

Plane waves are generated by moving a long plank up and down at the water surface. A square-section bar is a strange shape to choose for a wave maker, but the waves used in this thesis are not sensitive to the shape. This is because the main difference manifests in the higher-frequency part of the generated wave spectrum, and those high-frequency waves are not fast enough to propagate upstream against the current in the channel.

The dimensions of the plank used in this thesis are given in Figure 4.13. It is a little narrower than the channel so that it does not hit the side walls when moving.

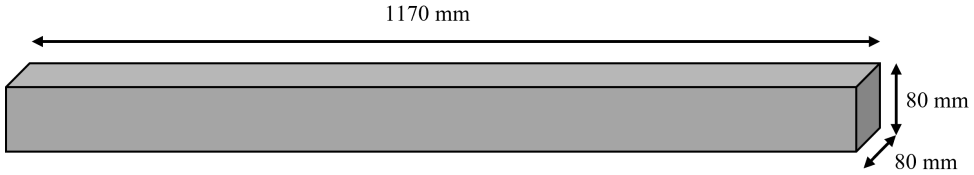

Figure 4.13: The dimensions of the plank used in the wavemaker.

4.4 Implementation of LDV

As mentioned in section 3.2, LDV is the chosen method for measuring the velocities in the water channel in this thesis. This section will give insight in how the LDV system was implemented in the experimental setup, and it gives specifications for the beams and the particles used.

4.4.1 Specifications

The two working parts of an LDV-system, illustrated in Figure 3.9, are the laser beams an the passing particles. The specifications for the laser beams used in this thesis are given in Table 4.3.

Beam system	
Wavelength	514.500nm
Focal length	500.000mm
Beam diameter	2.670mm
Expander ratio	1.000
Beam spacing	75.240mm

Table 4.3: Specifications for the laser beams used in the LDV-system in this thesis.

The particles used in the water channel are polymer spheres (Dynoseeds® TS 40 by Microbeads). It is important that they are similar to water particles so that their motion is similar to the turbulent flow. The size and density of the particles are given in Table 4.4.

Particles	
Diameter	40μm
Density	1050kgm^{-3}

Table 4.4: Specifications for the particles used in the water channel.

4.4.2 Physical setup

The laser beams in the LDV-system are sent from a laser probe. The probe used in this thesis is pictured in Figure 4.14. The probe is placed under the water channel, as illustrated in Figure 4.1, since the channel has a transparent floor, which means the laser lights go through.

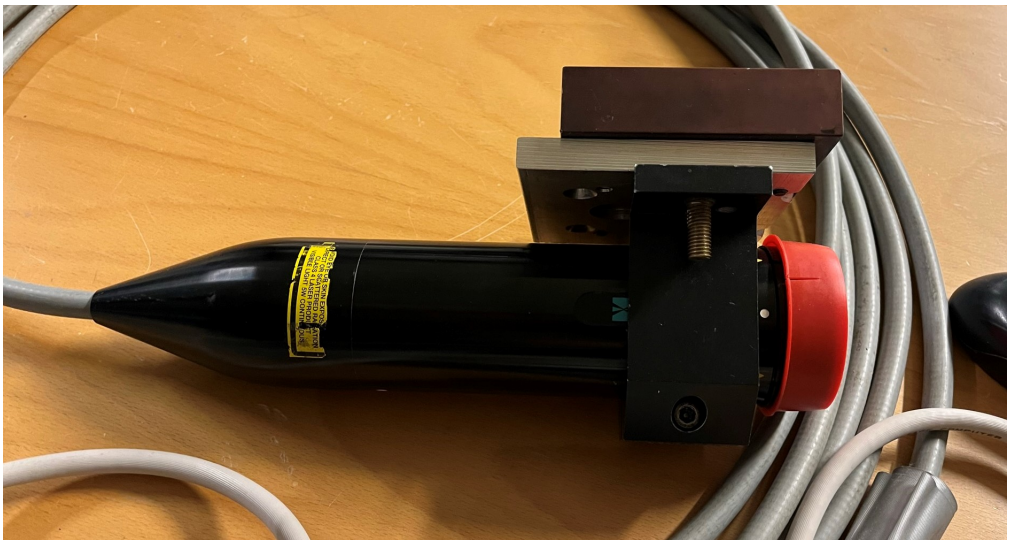

Figure 4.14: A photograph of the laser probe used in this thesis.

The laser probe was mounted to a traverse so that it could be moved easily and accurately. The traverse used is pictured in Figure 4.15. The wagon on the traverse, highlighted by the red circle, was moved remotely.

Figure 4.15: A photograph of the traverse used to move the laser probe. The wagon the probe was mounted to is highlighted by the red circle.

Chapter 5

Results and Discussion

This chapter shows results from the experiments conducted, and discuss them in terms of the research objectives and research question stated in chapter 1. Firstly, the flow profiles of the three active grid modes, both upstream and downstream, are discussed in terms of how appropriate they are for this study. Secondly, the modes are compared to each other in terms of turbulence intensity and integral length scale to see if, and if so, how they differ from each other. Lastly, the experiments with surface waves are compared to the ones without waves to answer the research question.

5.1 Flow profile

One of the objectives in this thesis, as stated in subsection 1.2.1, was to do experiments on turbulent flows without surface waves, partly to check that the flow is *uniform*, and *reproducible*. Measurements were made at 10 points across the span of the channel, both upstream and downstream, as shown in Figure 4.3, to get profiles of the flow, and to see how the flow develops downstream. The experiments were also run twice to see how reproducible the flows are.

5.1.1 Upstream

In Figure 5.1 we see the mean velocity profiles upstream of the flows with the three active grid modes given in Table 4.1. The results show that the velocity profiles are similar for both experiments of the same mode, especially for the two moving modes. The profiles for the static mode differs some, but the shapes seem to correlate well.

The profile of the spinning mode is fairly uniform, except for a little dip in velocity on the right side of the channel. This dip in velocity is also present in the two other grid modes, and it could be due to a blockage in the honeycomb grid. It could be checked by flipping the honeycomb to see if the flow then would get a dip in velocity on the left side, but these velocity profiles are adequate for the purpose of this thesis. The velocity profiles of the flows with the static and the 60°-flapping modes are less uniform, although fairly symmetrical. This could be due to some wake effects from the wings, as described in subsection 2.1.3. The wings are alternating which side of the rod they are mounted, as shown in Figure 3.3, and the measurement points between the wings that are facing each other (see Figure 4.3) seem to have lower mean velocity. Hence, there are some weaknesses with the set-up which causes nonuniform current, but it is considered to be sufficiently uniform for the purpose of this study.

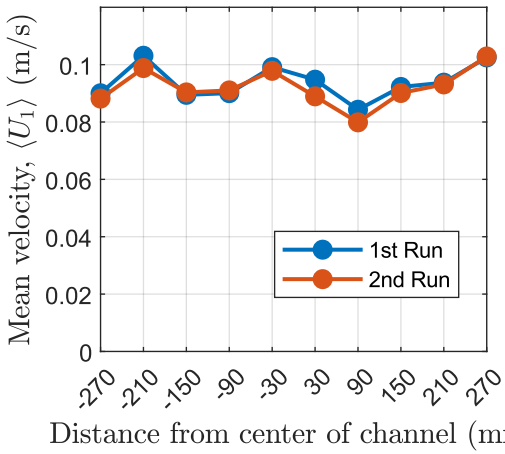

(a) Static mode.

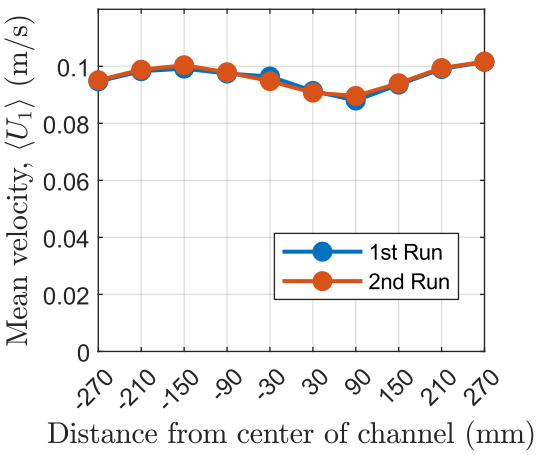

(b) Spin mode.

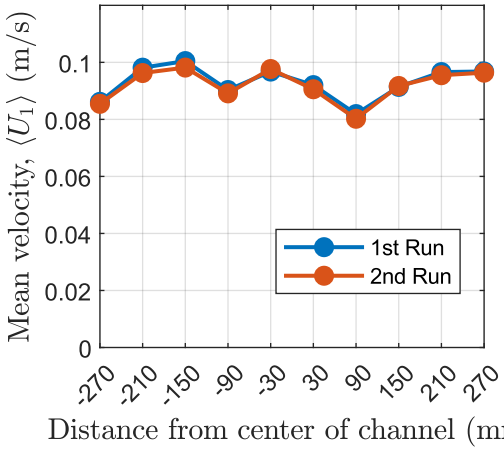

(c) 60° flap mode.

Figure 5.1: The mean velocity profiles of the channel flows upstream with the three different AG modes.

In Figure 5.2 we see the velocity variance profiles of the three different active grid modes. This is an indication of the turbulent kinetic energy of the flow, but not an actual measurement for it. To actual measure it, I would have needed all three velocity components. The three modes give clearly different values of velocity variance, signifying that there is a significant difference in turbulence intensity between them. The profiles seem fairly uniform, except for a sharp increase in variance on the rightmost side of the channel. There also seems to be a dip at 90mm right of the center, the same point where the mean velocity was lower.

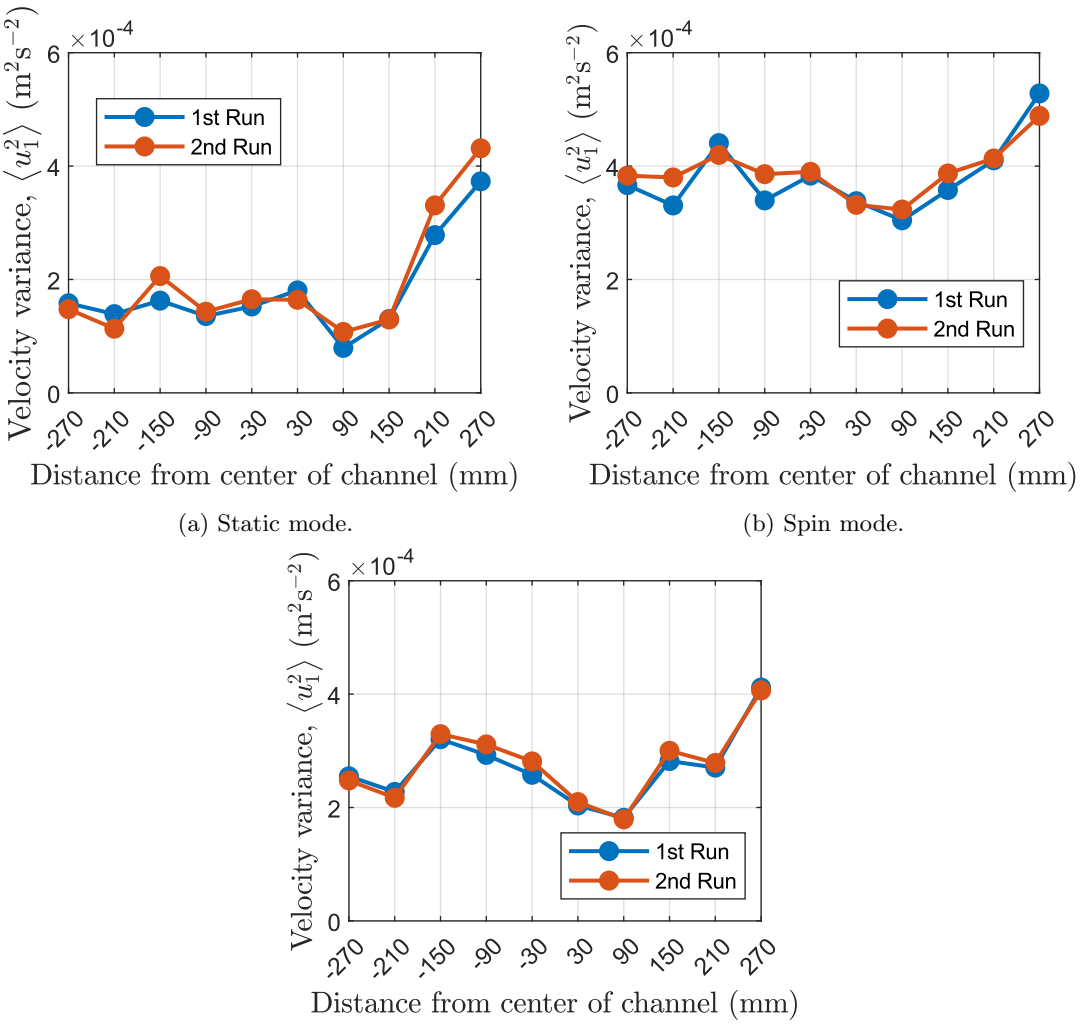

(a) Static mode.

(b) Spin mode.

(c) 60° flap mode.

Figure 5.2: The velocity variance profiles of the channel flows upstream with the three different AG modes.

The integral length scale profiles of the three different active grid modes are shown in Figure 5.3. The profiles show relatively regular behaviour for the two moving modes, except for some deviations on the far right side. The different experiments with the same modes give similar results, and the profiles seem to correlate with each other. The profile of the static mode however shows irregular behaviour, meaning that the values differ significantly between the two experiments and across the profile. The large integral scales in streamwise direction for the static mode could be caused by wakes behind the wings that have not broken up into turbulence yet, or wakes that have not connected to each other. Non-turbulent flow would correlate longer than turbulent flows, given that the mean flow is statistically stationary, which would yield longer integral scales. I do not currently have an explanation for the huge increase, especially for the static mode, in integral scale towards the right.

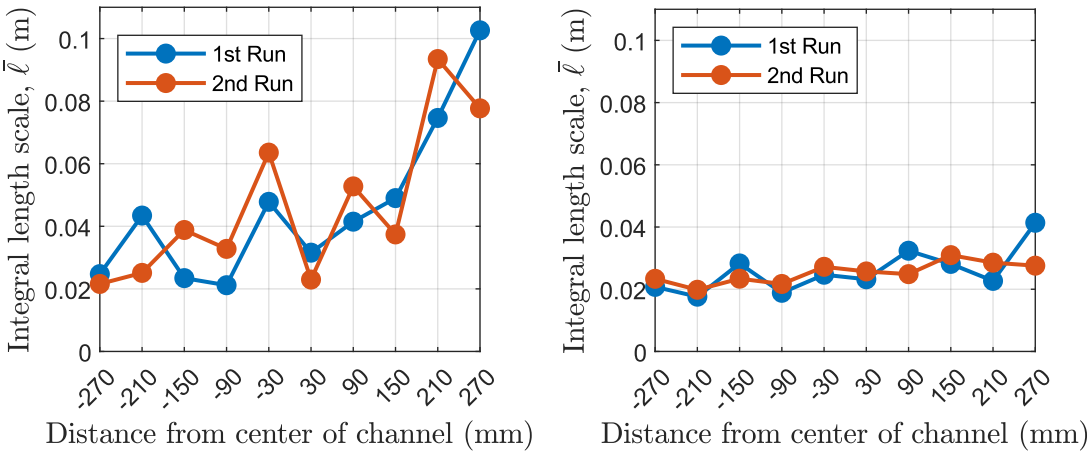

(a) Static mode.

(b) Spin mode.

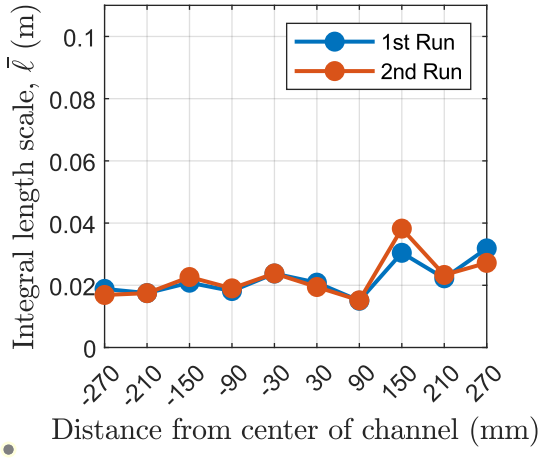

(c) 60° flap mode.

Figure 5.3: The integral length scale profiles of the channel flows upstream with the three different AG modes.

The flow profiles upstream seem fairly uniform for the spin mode of the active grid, with a slightly lower velocity just right of the center of the channel and a sharp increase in velocity variance at the far right of the channel. The spinning mode giving the most uniform flow profile is probably due to it doing the most vigorous mixing of the flow, and that the motion of the wings cover the whole span of the channel, meaning that there are no streaks of unmixed flow.

The mean velocity profile of the flapping mode is not completely uniform, but it is fairly symmetrical around the center of the channel. The non-uniformity could be caused by a non-uniformity in the active grid, meaning that the grid is not mixing equally across the span of the channel. In Figure 3.5 we see that the wings are mounted on one side of the rods, meaning that the grid is alternating between having the wings on opposite sides of the rod, and having them facing each other. If we compare the profile in Figure 5.1 with the location of the measurement points in Figure 4.3, there seem to be lower velocities for the flapping mode for the points located between to wings facing each other.

The velocity variance also seems to be varying some across the span of the channel, but the two separate experiments give similar profiles. The variance profile for the flapping mode is not symmetrical like the velocity profile. The integral length scale profile is however fairly uniform, with some varying values on the far right of the channel. This indicates that the whole span of the channel is turbulent, but that the non-uniformity of the grid causes the turbulence intensity to vary.

The mean velocity profile of the static mode is, similar to the flapping mode, not uniform. This could also be, partly, due to the non-uniformity of the active grid. The velocity profile of the static mode and the flapping mode look fairly similar in the sense that the velocity is low and high at the same locations. Another effect that is probably affecting the profiles of the static mode is the development of turbulent wakes behind the wings. It is shown in subsection 2.1.3 that the Reynolds number is large enough to generate turbulent wake behind a cylinder of the same diameter as the wing and rod. This probably means that turbulent wakes are generated behind the wings as well. The characteristics of a wake behind a wing in the active grid is difficult to predict due to the non-symmetrical shape they have facing the flow, as shown in Figure 3.3, and it is outside the scope of this thesis to describe such wakes.

The velocity variance profile seems to be fairly uniform and regular, except for the sharp increase at the far right side. The integral length scale profile, however, is highly irregular compared to the other modes, and the values vary a lot both between the two different experiments and across the span of the channel. This could indicate that the turbulence is not fully developed, meaning that turbulence characteristics are dependent on both spanwise and streamwise position.

The sharp increase in velocity variance on the far right side of the channel are difficult to explain, but there is a trend of there being less samples in the time series on the right side of the channel, as shown in Figure 5.4. This means that the results on the right side of the channel are more uncertain as there are less data to calculate statistics with, which could be a reason for the more irregular results on that side.

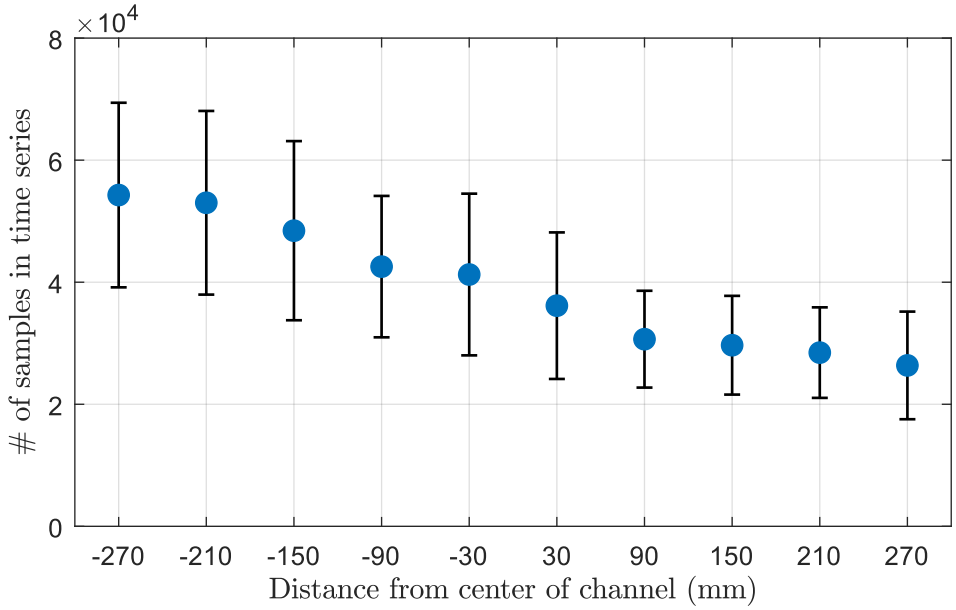

Figure 5.4: This is a graph showing the average number of samples in the time series at the different spanwise locations in the channel. The mean is calculated using both the upstream and downstream measurements. The errorbars are the standard deviations in number of samples at each point.

The reason for the decline in the number of samples in the time series on the right side of the channel is that I only refilled particles in the water channel before I started the experiments, and I always conducted the experiments from left to right in the channel. This means that particles would have settled in the stationary parts of the water tank when the measurements on the right side were done.

5.1.2 Downstream

The mean velocity profiles downstream, shown in Figure 5.5, are more uniform than the profiles upstream, with a little dip at the same location as upstream. The velocity also seems to be marginally higher than upstream. The two different runs are similar for the moving modes, whereas there are some differences on the sides for the static mode.

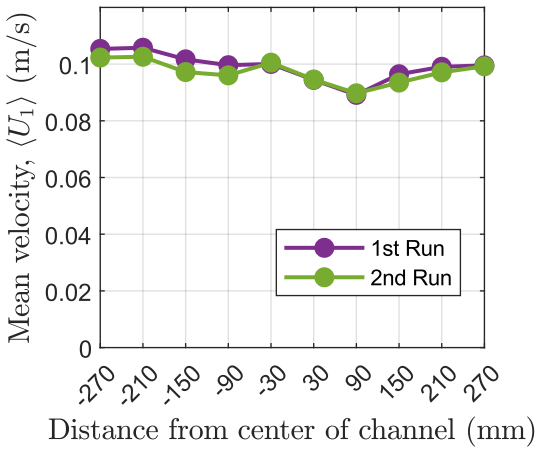

(a) Static mode.

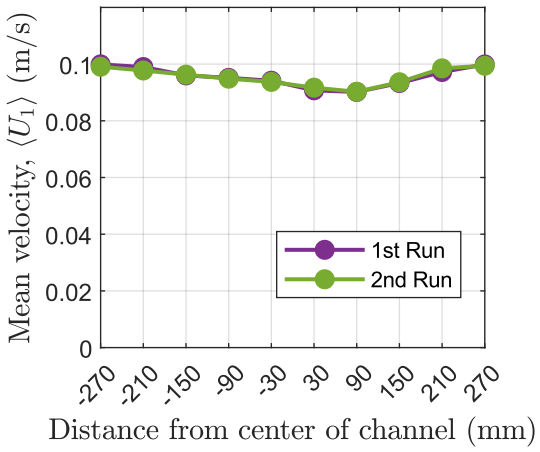

(b) Spin mode.

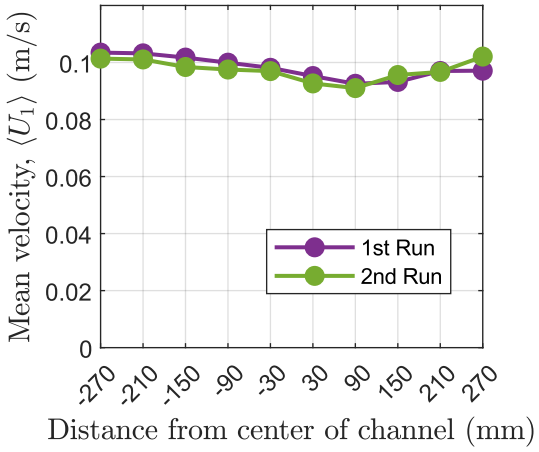

(c) 60° flap mode.

Figure 5.5: The mean velocity profiles of the channel flows downstream with the three different AG modes.

The variance profiles downstream are shown in Figure 5.6. They are indistinguishable between the different modes and much lower than upstream, meaning that the turbulence intensity generated by the active grid has mostly dissipated between the upstream and downstream measuring points.

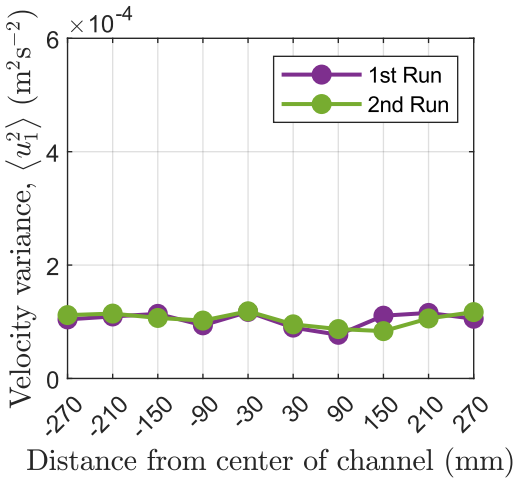

(a) Static mode.

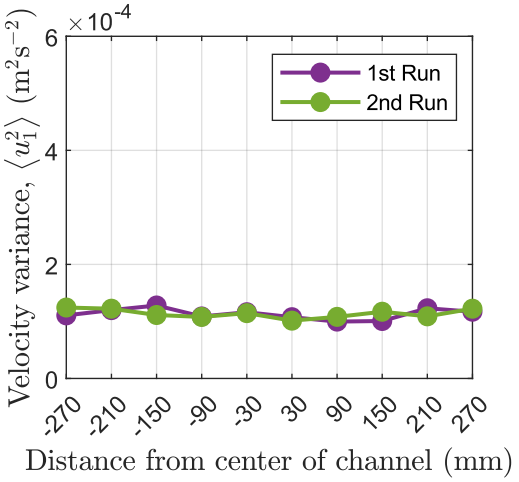

(b) Spin mode.

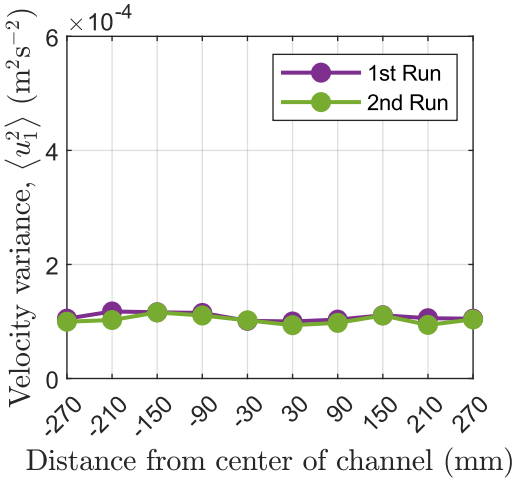

(c) 60° flap mode.

Figure 5.6: The velocity variance profiles of the channel flows downstream with the three different AG modes.

The integral length scale profiles, shown in Figure 5.7, are fairly similar in shape to the profiles upstream, but the scales are a little longer. The peak on the right side on the profile upstream for the flapping mode is also present downstream. The static mode varies significantly across the span of the the channel, but the two different runs give more similar results than the two runs upstream, having the peaks and dips at the same points.

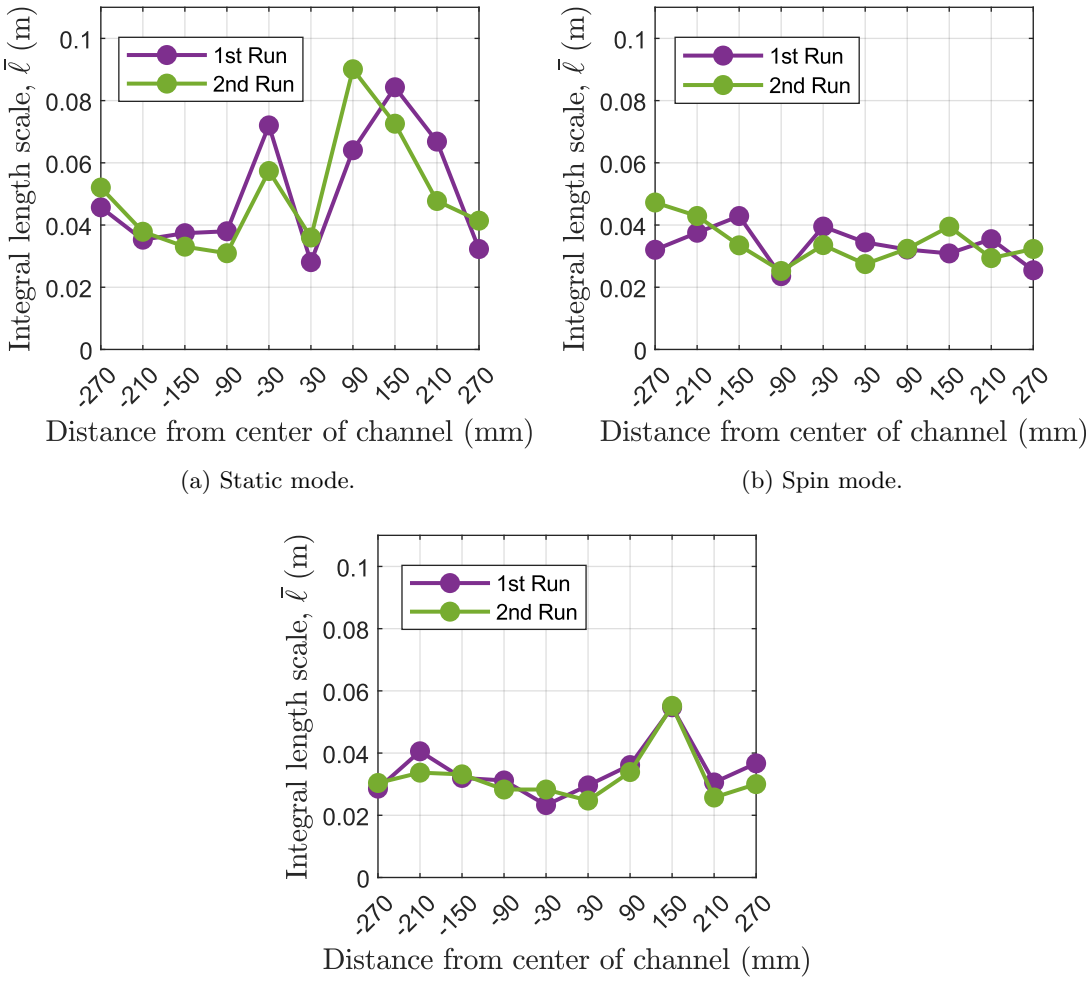

(a) Static mode.

(b) Spin mode.

(c) 60° flap mode.

Figure 5.7: The integral length scale profiles of the channel flows downstream with the three different AG modes.

The mean flow profiles are more uniform downstream than upstream, indicating that there has been mixing of momentum between those two locations.

The velocity variance profiles are almost identical for the three different modes, and much lower than upstream. This indicates that the turbulence intensity generated by the active grid has almost completely dissipated at this point in the channel. One theory to why the turbulence intensity has dissipated so quickly is that the turbulence boundary layer, described in subsection 2.1.2, is thick enough for the measurement point to be fully submerged in it. The rough calculations done in subsection 2.1.2 indicate that the boundary layer is in the transitional area at the downstream measurement points, but there are factors that are not accounted for when doing these estimations, such as surface roughness and shear in the flow.

The integral length scale profiles are however fairly different between the three modes. The shape of the profiles also resembles the profiles upstream, to a certain degree, which indicate that even though the turbulence has dissipated from upstream to downstream, the large eddies still remain. The integral length scale has actually increased slightly from upstream to downstream for all three modes. This could be due to longer correlation of the velocity data when there is less turbulence.

5.2 Mode comparison

The three different active grid modes used in this experiment (see subsection 3.1.2, subsection 3.1.3, and subsection 4.2.2 for descriptions) are discussed in terms of velocity variance, indicating the turbulence intensity of the flow, and integral length scale in section 5.1. This section aims at giving a more direct comparison in terms of these parameters, since it is specified in subsection 1.2.1 that the modes should clearly differ from one another in both parameters.

5.2.1 Upstream

In Figure 5.8 we see plots comparing the integral length scale and velocity variance of the three different active grid modes used in these experiments. These are similar to the plots in Figure 3.7 and Figure 3.8. There are two plots, one where the integral length scale is calculated using Equation 2.32, and one where it is calculated using Equation 2.33. This is to get better confidence in the results concerning the integral length scale.

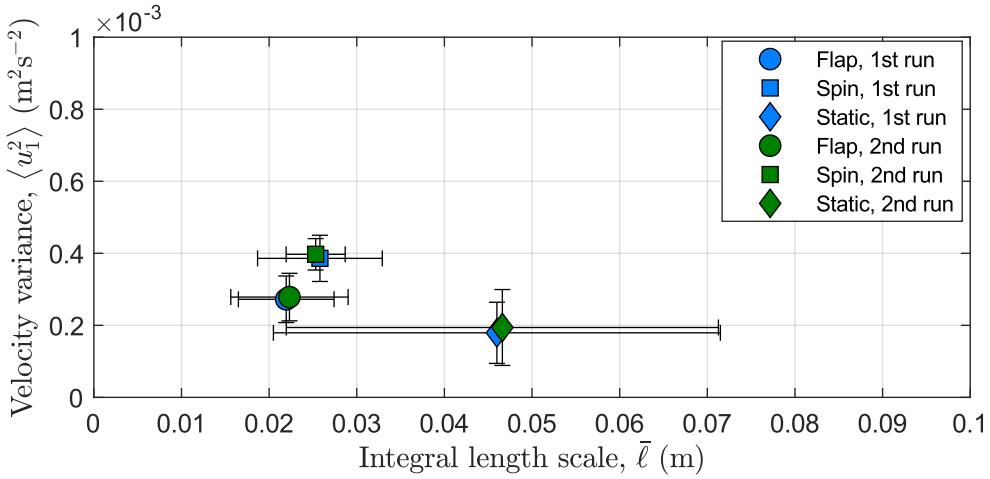

(a) Integral length scale calculated using Equation 2.32

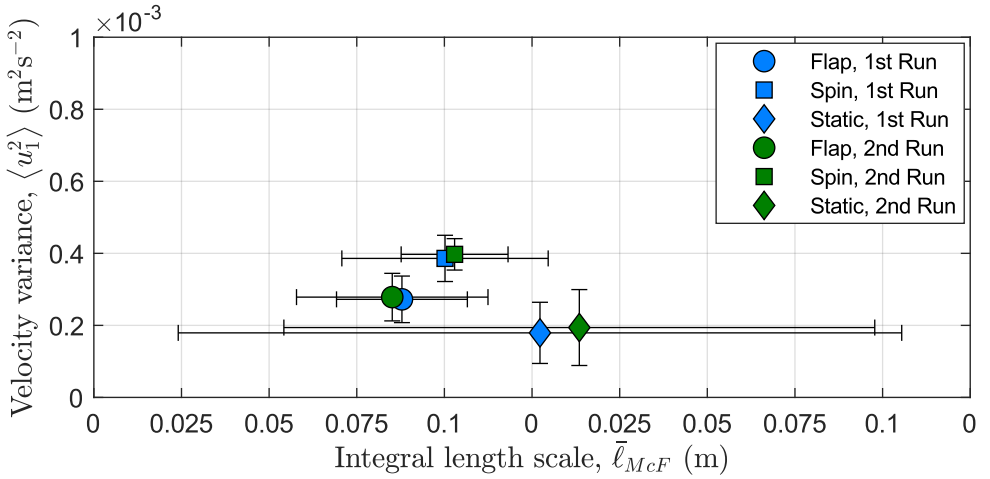

(b) Integral length scale calculated using Equation 2.33

Figure 5.8: The integral length scale of the three modes specified in subsection 4.2.2, plotted against their velocity variance. The values are calculated by taking the mean of the measurements at the ten points upstream, and the errorbars are the standard deviation of the those ten values.

The results show that there is a difference in velocity variance between the three modes, hence, meaning that there is a difference in turbulence intensity. The errorbars do overlap some, but the

profiles in Figure 5.2 show that there is some correlation in where the variance is high and low, e.g. that the variance is relatively high on the far right for all three modes.

The integral length scales do also seem to differ between the three modes, although the errorbars do encapsulate more than one mode. The errorbars for the static mode are especially large. They show the standard deviation of the 10 measurements across the channel, and we can see in Figure 5.3 how the profile for the static mode varies significantly. This was discussed in subsection 5.1.1, and it was proposed that it could be due to the wakes behind the wings not being connected with each other at this point in the flow.

There is also not as much correlation between the modes in how the integral length scale varies across the profile, shown in Figure 5.3, as for the variance. The two separate runs for each mode do seem to give very similar results though, indicating that these results are reproducible. There does also seem to be a correlation between the two integral length scales, giving further confidence that there are differences between the three modes in terms of length scale of the larger eddies.

The integral length scale calculated using Equation 2.32 give smaller errorbars and more similar results in the two separate runs, which is why that is used in the other results.

5.2.2 Downstream

In Figure 5.9 we see the downstream comparisons of the three modes in terms of integral length scale and velocity variance. Similar to in subsection 5.2.1, there is one plot with integral length scale calculated using Equation 2.32, and one using Equation 2.33.

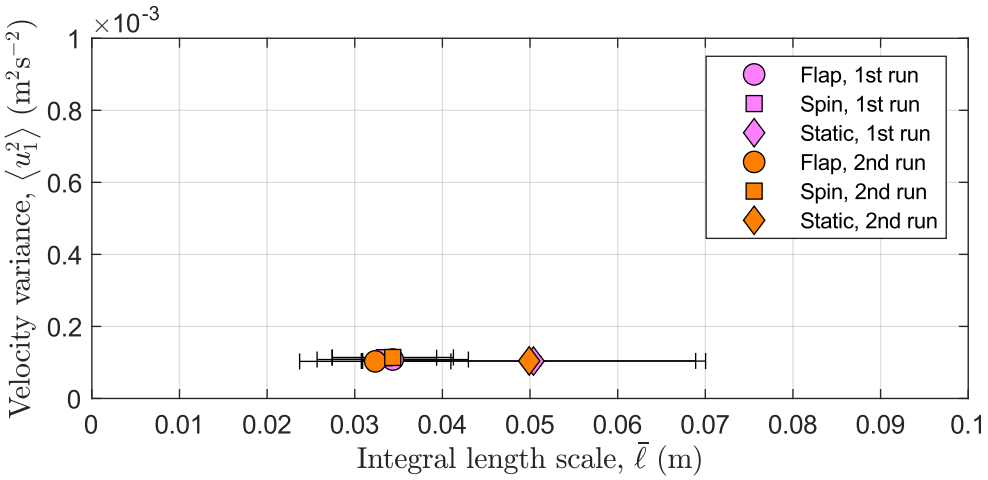

(a) Integral length scale calculated using Equation 2.32

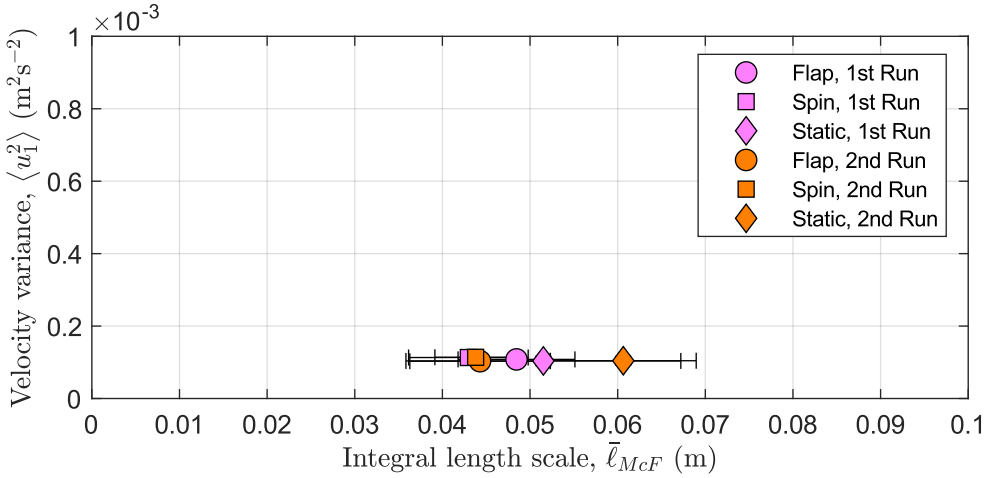

(b) Integral length scale calculated using Equation 2.33

Figure 5.9: The integral length scale of the three modes specified in subsection 4.2.2, plotted against their velocity variance. The values are calculated by taking the mean of the measurements at the ten points downstream, and the errorbars are the standard deviation of the those ten values.

As discussed in subsection 5.1.2, we can clearly see here that the turbulence intensity generated by the active grid has mostly dissipated at this point in the channel. It is therefore impossible to differentiate the three modes in terms of turbulence intensity here using the same methods that are used in this thesis. Theories to why this has happened are discussed in subsection 5.1.2.

It was also discussed in subsection 5.1.2 that there seemed to be a difference in integral length scale between the modes, even though the turbulence intensity has completely dissipated. This is apparent also in Figure 5.9, at least between the static mode and the moving modes. It is also easier to see here that the integral length scale seems to have increased slightly downstream.

5.3 Comparison with and without surface waves

The research question of this thesis is: How do surface waves impact the turbulence intensity and integral length scale of a shallow, turbulent, open-channel flow? Since we are investigating these two parameters, and the three active grid modes are inseparable in terms of turbulence intensity downstream, it was decided that the measurements with surface waves would only be done upstream. Also, due to time constraints, there were only done two experiments with surface waves, both 3cm to the right of the center of the channel, one with the spinning mode and one

with the static. Those two modes were chosen since they were the least similar of the three modes.

The measurements of the flows with surface waves were decomposed into a wave component and a turbulent component, as shown in section 3.4, and it is the turbulent component that is analyzed in this section. This is because it is turbulent properties that are being investigated.

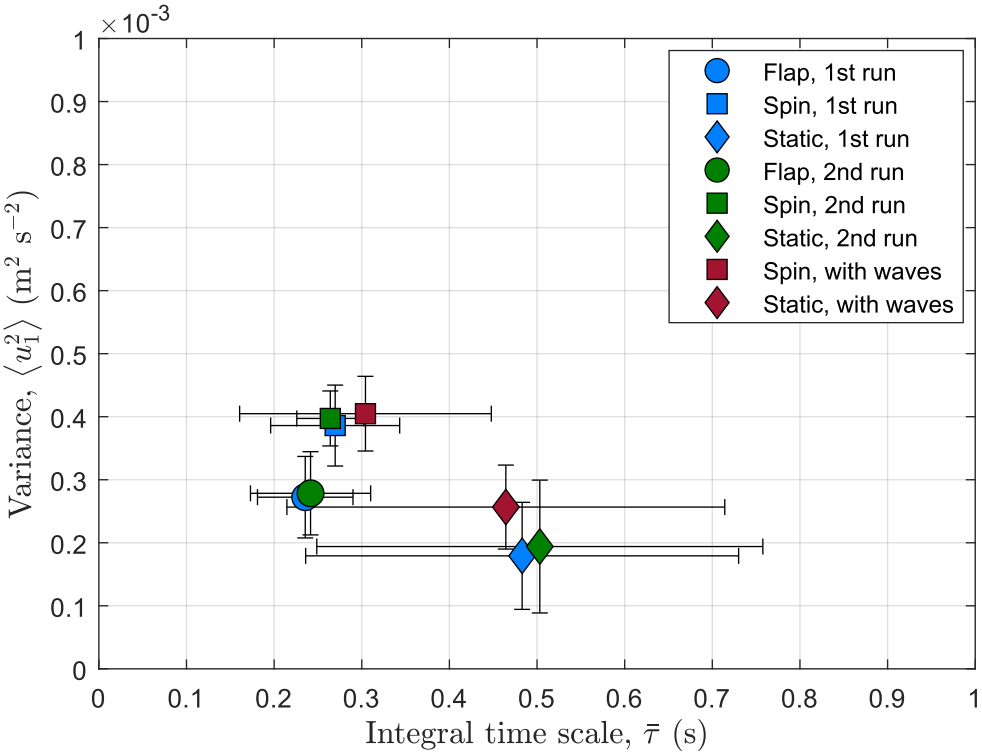

Figure 5.10: An integral time scale/velocity variance-plot for the result from the experiments without waves upstream, similar to Figure 5.8, and for the results of the experiments with surface waves. The red markers are the results with waves

In Figure 5.10 we see plots comparing the integral time scale (from Equation 2.31) and velocity variance of flows with the three active grid without waves, and the turbulence components of the two experiments with waves. Integral time scale is used instead of integral length scale, like in Figure 5.8, because the Taylor hypothesis is questionable when the mean flow is periodic, as it is in the experiments with surface waves. On the whole it is quite dodgy to calculate integral scales from a one point measurement (Eulerian) when there is wave motion, as the concept of integral scales are based on a Lagrangian idea of the "size of an eddy being transported". Nevertheless, the results here give an idea of integral scales in the flows with waves.

The results show that the turbulence component of the flows with waves give similar results as the flows without waves in terms of integral time scale and velocity variance. The experiment with waves on the spin mode give slightly larger integral time scale, but the uncertainty in the results is too large to conclude anything from that. The results do also show that the variance is slightly higher with waves for the static mode, and the uncertainty of that result is much smaller, as shown by the errorbars.

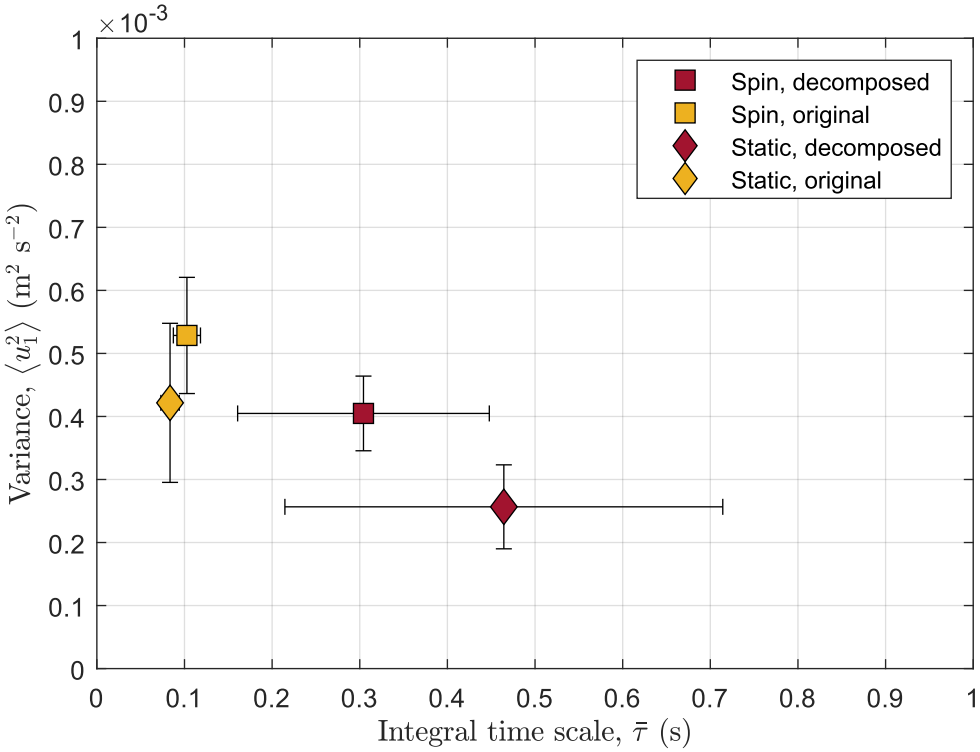

Figure 5.11: An integral time scale/velocity variance-plot for the turbulence component of the experiments with surface waves, and for the original signal for the same experiments. The results from the original signals are the yellow markers, and the turbulence components are the red ones.

In Figure 5.11 we see the velocity variance and integral time scale for the original signal from the experiments with waves, and the turbulence component from the same signal. It shows that both variance and integral time scale have changed significantly when removing the wave component from the signal, and the fact that turbulence components give such similar results to experiments without surface waves indicate that the decomposition method used to remove the wave component has worked fairly well.

The velocity spectra of the turbulence component of the experiments with surface waves are plotted in Figure 5.12 together with the velocity spectra of the measurements done at the same point without waves. We can clearly see the valleys around the wave frequency (2.4Hz, given in Table 4.2), which is discussed in subsection 3.4.1. We can also see that there still are small peaks at the wave frequency, signifying that there is still some wave motion in the turbulence component extracted from the original signal.

As mentioned above, it is impossible to conclude anything about the impact of waves on integral length scales in a turbulent flow, but there could be signs of waves increasing the turbulence intensity. This is in agreement with the results from Savelyev et al., 2012, who found in both numerical and laboratory simulations that turbulent kinetic energy grew in time due to the wave-turbulence interaction. The numerical simulations in Tsai et al., 2015 of gravity surface waves propagating over a turbulence field also showed a significant growth of the initially weak turbulence.

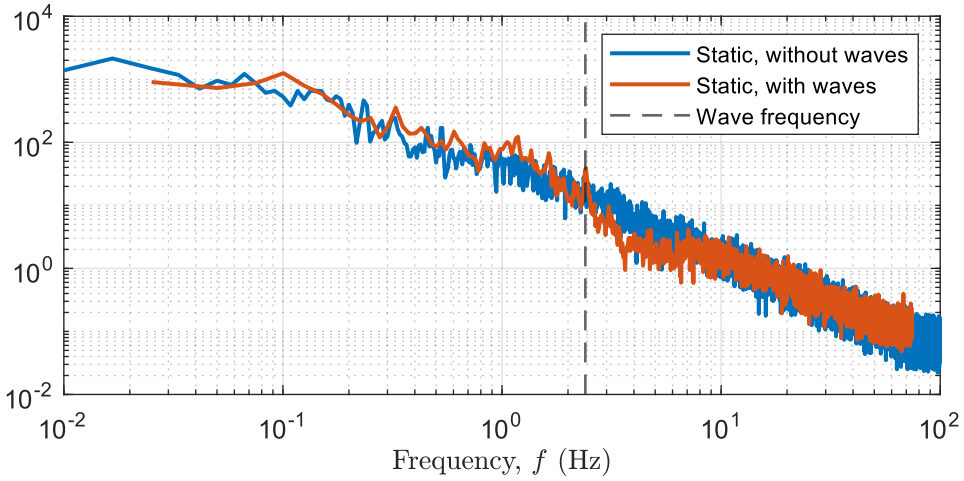

(a) Static mode

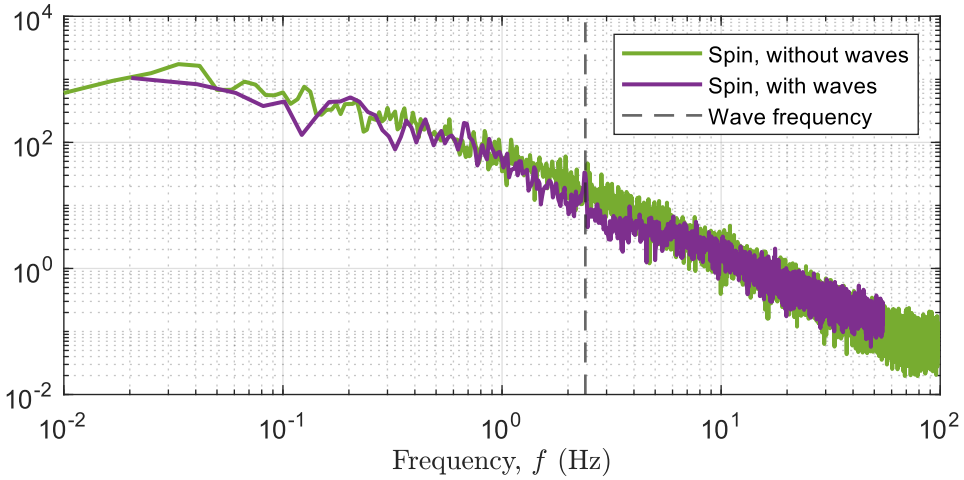

(b) Spin mode

Figure 5.12: PSD's of the turbulence component of the experiments with surface waves compared with the experiments without surface waves at the same location with the same active grid mode. The PSD's are normalized using the mean of the values between $10 - 20$Hz in frequency.

The results in Figure 5.10 are influenced by the imperfect separation of waves and turbulence from the decomposition of the signal. Some turbulent motion appears to have been removed along with the waves, judging from the decrease in the velocity spectra in vicinity of the wave frequency, shown in Figure 5.12 (also shown in Figure 3.16). Some wave orbital velocity also seem to remain in the turbulent signal, judging from the small peak in the velocity spectra at the wave frequency. The loss of turbulent motion would be assumed to lead to some loss of turbulent kinetic energy in the results, while the inclusion of some wave motion would be assumed to lead to the opposite. It is therefore difficult to give a concluding answer to the turbulence intensity part of the research question without doing an analysis of how large the loss and gain in turbulent kinetic energy is due to this. This has unfortunately not been done in this thesis.

Separation of wave motion and turbulent motion is a well-known problem, because generated waves always have a finite bandwidth, especially those generated on top of currents. This experimental setup is even used to study the broadening of the wave spectrum as it propagates (Løvvig, 2023), so the wave motion itself has become more disordered by the time it reaches the upstream measurement points. Qiao et al., 2016, conducted field experiments on wave-turbulence interaction where they had to separate turbulent and wave motion for a very broad wave spectrum. Their solution to this problem was by using the, at the time, recently developed Holo-Hilbert spectral analysis

(Norden E. Huang, Hu et al., 2016), for each IMF component.

As opposed to Qiao et al., 2016, the experiments in this thesis are conducted in a lab with generated waves, and there are therefore ways to work around the issues of separating wave motion when there is a broad wave spectrum. An obvious way to get a narrower wave spectrum would be to do the measurements downstream instead of upstream, as the waves would have interacted with the current for shorter time. This would also have been beneficial in the sense that the turbulence would have interacted with the waves for a longer period, meaning that the impact of the waves on the turbulence would presumably be greater. Another idea would be to use repeated wave groups, like in Smeltzer et al., 2023, where I could compare the turbulence before and after with very little waves present at the same time.

Chapter 6

Conclusion and Further work

6.1 Conclusion

As mentioned in chapter 1, this thesis is a proof-of-concept study to test the possibilities of experimental studies on wave-turbulence interactions in the lab used here. The research question that was set to be answered was: "How do surface waves impact the turbulence intensity and integral length scale of a shallow, turbulent, open-channel flow?" Three research objectives were set to answer this question:

1. Conduct experiments with turbulent flows without surface waves.
2. Conduct experiments with turbulent flows with surface waves.
3. Process data from experiments to analyze the impact of surface waves on turbulence.

The results shown in section 5.1, which is from the experiments, gave indications to how appropriate the turbulent flows generated by the the three active grid modes, static, spinning, and 60°-flapping, were. The spinning mode gave a fairly uniform flow profile both upstream and downstream, meaning that it would be suitable for experiments on wave-turbulence interactions. The flapping mode gave a symmetrical, but non-uniform velocity profile upstream. The non-uniformity could be due to the grid being non-uniform, and it could possibly be solved by having the grid do larger strokes than 60°. Other than this, the flapping mode seemed to give fairly uniform profiles in terms of turbulence intensity and integral length scale both upstream and downstream. The profiles of the static mode seemed to indicate that the turbulence was not fully developed, meaning that the wakes generated behind the wings had not fully connected to each other. It was especially the large integral scale at certain points in the profile which indicated this. This is not ideal for the type of parameter study done in this thesis.

The results in section 5.2 showed that the three grid modes yielded different turbulent flows upstream, in terms of both intensity and integral length scale. They also showed that the turbulence intensity had mostly dissipated downstream, to the point where the three grid modes were indistinguishable in that term. The integral length scale seemed to remain somewhat different however. This means that this active grid can be used to generate different turbulent flows with varying intensity and integral scale, but that the quick dissipation might need to be looked further into if there are to be conducted parameter studies downstream.

As for the research question, the results in section 5.3 provide some insight to how surface waves impact the turbulence intensity and integral length scale of the flows. The results in terms of integral length scale were inconclusive, as there were far to much uncertainty in the results, and too few experiments to show any real trends. There were a slight indication in the result with the static grid mode that the turbulence intensity was enhanced by the surface waves, which is in agreement with the literature, but there is too much uncertainty related to the separation of

turbulent and wave motion that this result can be used to conclude anything. If this research question is to be investigated in this lab in the future, then some other approaches should be considered, such as doing the experiments with waves downstream, since the spectrum of waves would presumably be narrower than upstream, making the velocity signal easier to decompose. Another approach would be to use repeated wave groups and compare the turbulence before and after, with very little waves present at the same time.

6.2 Further work

As this thesis is a proof-of-concept study, it is a platform for further studies on the wave-turbulence interaction in this lab. Some suggestions on how to improve the experiments in this thesis were given in both section 5.3 and section 6.1. It should also be possible to do PIV measurements of the flow to get a better understanding of the flow field and the structures in the flow. Ideally, it should be possible to do simultaneous measurements of the turbulence, like the ones done in this thesis, and of the waves, like in Løvvig, 2023. Then you could directly correlate changes in turbulence with scattering of waves.

Bibliography

Adrian, R. J. and C. S. Yao (Jan. 1986). 'Power spectra of fluid velocities measured by laser Doppler velocimetry'. In: *Experiments in Fluids* 5.1, pp. 17–28. ISSN: 1432-1114. DOI: 10.1007/BF00272419. URL: https://doi.org/10.1007/BF00272419.

Albrecht, H.-E et al. (Jan. 2003). 'Laser Doppler and Phase Doppler Measurement Techniques'. In: pp. 545–572, 628–635. ISBN: 978-3-642-08739-4. DOI: 10.1007/978-3-662-05165-8_4.

Borue, Vadim, Steven A. Orszag and Ilya Staroselsky (1995). 'Interaction of surface waves with turbulence: direct numerical simulations of turbulent open-channel flow'. In: *Journal of Fluid Mechanics* 286, pp. 1–23. DOI: 10.1017/S0022112095000620.

Brocchini, M. and D. H. Peregrine (2001). 'The dynamics of strong turbulence at free surfaces. Part 1. Description'. In: *Journal of Fluid Mechanics* 449, pp. 225–254. DOI: 10.1017/S0022112001006012.

Buchhave, P. (Jan. 1976). 'Biasing errors in individual particle measurements with the LDA-counter signal processor'. In: *The Accuracy of Flow Measurements by Laser Doppler Methods*, pp. 258–278.

Cekli, Hakki Ergun and Willem van de Water (Aug. 2010). 'Tailoring turbulence with an active grid'. In: *Experiments in Fluids* 49.2, pp. 409–416. ISSN: 1432-1114. DOI: 10.1007/s00348-009-0812-5. URL: https://doi.org/10.1007/s00348-009-0812-5.

Cengel, Yunus A and John M Cimbala (2017). *Fluid mechanics: Fundamentals and applications*. 4th ed. Columbus, OH: McGraw-Hill Education.

D'Asaro, Eric A. (2014). 'Turbulence in the Upper-Ocean Mixed Layer'. In: *Annual Review of Marine Science* 6.1. PMID: 23909456, pp. 101–115. DOI: 10.1146/annurev-marine-010213-135138. eprint: https://doi.org/10.1146/annurev-marine-010213-135138. URL: https://doi.org/10.1146/annurev-marine-010213-135138.

Djupesland, Johannes (Dec. 2022). *Tailoring turbulence in an open-channel flow*. Project report. Available from author upon request.

Gibson, M. M. and W. Rodi (1989). 'Simulation of free surface effects on turbulence with a Reynolds stress model'. In: *Journal of Hydraulic Research* 27.2, pp. 233–244. DOI: 10.1080/00221688909499183. eprint: https://doi.org/10.1080/00221688909499183. URL: https://doi.org/10.1080/00221688909499183.

Guo, Xin and Lian Shen (2013). 'Numerical study of the effect of surface waves on turbulence underneath. Part 1. Mean flow and turbulence vorticity'. In: *Journal of Fluid Mechanics* 733, pp. 558–587. DOI: 10.1017/jfm.2013.451.

Handler, R. A. et al. (1993). 'Length scales and the energy balance for turbulence near a free surface'. In: *AIAA Journal* 31.11, pp. 1998–2007. DOI: 10.2514/3.11883. eprint: https://doi.org/10.2514/3.11883. URL: https://doi.org/10.2514/3.11883.

Hearst, R. Jason (2019). 'The Use of Active Grids in Experimental Facilities'. In: *Progress in Turbulence VIII*. Ed. by Ramis Örlü et al. Cham: Springer International Publishing, pp. 173–178. ISBN: 978-3-030-22196-6.

Hideharu, Makita (Oct. 1991). 'Realization of a large-scale turbulence field in a small wind tunnel'. In: *Fluid Dynamics Research* 8.1-4, p. 53. DOI: 10.1016/0169-5983(91)90030-M. URL: https://dx.doi.org/10.1016/0169-5983(91)90030-M.

Huang, Norden E et al. (2003). 'A confidence limit for the empirical mode decomposition and Hilbert spectral analysis'. In: *Proceedings of the Royal Society of London. Series A: Mathematical, Physical and Engineering Sciences* 459.2037, pp. 2317–2345. DOI: 10.1098/rspa.2003.1123. eprint: https://royalsocietypublishing.org/doi/pdf/10.1098/rspa.2003.1123. URL: https://royalsocietypublishing.org/doi/abs/10.1098/rspa.2003.1123.

Huang, Norden E., Kun Hu et al. (2016). 'On Holo-Hilbert spectral analysis: a full informational spectral representation for nonlinear and non-stationary data'. In: *Philosophical Transactions of the Royal Society A: Mathematical, Physical and Engineering Sciences* 374.2065, p. 20150206. DOI: 10.1098/rsta.2015.0206. eprint: https://royalsocietypublishing.org/doi/pdf/10.1098/rsta.2015.0206. URL: https://royalsocietypublishing.org/doi/abs/10.1098/rsta.2015.0206.

Huang, Norden E., Zheng Shen and Steven R. Long (1999). 'A NEW VIEW OF NONLINEAR WATER WAVES: The Hilbert Spectrum'. In: *Annual Review of Fluid Mechanics* 31.1, pp. 417–457. DOI: 10.1146/annurev.fluid.31.1.417. eprint: https://doi.org/10.1146/annurev.fluid.31.1.417. URL: https://doi.org/10.1146/annurev.fluid.31.1.417.

Huang, Norden E., Zheng Shen, Steven R. Long et al. (1998). 'The empirical mode decomposition and the Hilbert spectrum for nonlinear and non-stationary time series analysis'. In: *Proceedings of the Royal Society of London. Series A: Mathematical, Physical and Engineering Sciences* 454.1971, pp. 903–995. DOI: 10.1098/rspa.1998.0193. eprint: https://royalsocietypublishing.org/doi/pdf/10.1098/rspa.1998.0193. URL: https://royalsocietypublishing.org/doi/abs/10.1098/rspa.1998.0193.

Hussain, A. K. M. F. and W. C. Reynolds (1970). 'The mechanics of an organized wave in turbulent shear flow'. In: *Journal of Fluid Mechanics* 41.2, pp. 241–258. DOI: 10.1017/S0022112070000605.

Jooss, Yannick et al. (2021). 'Spatial development of a turbulent boundary layer subjected to freestream turbulence'. In: *Journal of Fluid Mechanics* 911, A4. DOI: 10.1017/jfm.2020.967.

Kolmogorov, A. N. (1941). 'The local structure of turbulence in incompressible viscous fluid for very large Reynolds number'. In: *Dokl. Akad. Nauk. SSSR* 30, pp. 301–303. URL: https://cir.nii.ac.jp/crid/1572824499981613312.

Lorenz, Edward N. (1963). 'Deterministic Nonperiodic Flow'. In: *Journal of Atmospheric Sciences* 20.2, pp. 130–141. DOI: https://doi.org/10.1175/1520-0469(1963)020⟨0130:DNF⟩2.0.CO;2. URL: https://journals.ametsoc.org/view/journals/atsc/20/2/1520-0469_1963_020_0130_dnf_2_0_co_2.xml.

Løvvig, Inger Skundberg (June 2023). *Experimental study of the effect of turbulence on surface waves*. Master's thesis.

Lyon, Douglas (2009). 'The discrete Fourier transform, part 4: Spectral leakage'. en. In: *J. Object Technol.* 8.7, p. 23.

Mora, D.O. and M. Obligado (2020). 'Estimating the integral length scale on turbulent flows from the zero crossings of the longitudinal velocity fluctuation'. In: *Experiments in Fluids* 61, p. 199. DOI: 10.1007/s00348-020-03033-2.

Mulla, I A, R Sampath and S R Chakravarthy (July 2019). 'Interaction of lean premixed flame with active grid generated turbulence'. In: *Heat and Mass Transfer* 55.7, pp. 1887–1899.

Mydlarski, Laurent (Nov. 2017). 'A turbulent quarter century of active grids: from Makita (1991) to the present'. In: *Fluid Dynamics Research* 49.6, p. 061401. DOI: 10.1088/1873-7005/aa7786. URL: https://dx.doi.org/10.1088/1873-7005/aa7786.

Nuttall, A. (1981). 'Some windows with very good sidelobe behavior'. In: *IEEE Transactions on Acoustics, Speech, and Signal Processing* 29.1, pp. 84–91. DOI: 10.1109/TASSP.1981.1163506.

Peruzzi, C. et al. (2021). 'On the influence of collinear surface waves on turbulence in smooth-bed open-channel flows'. In: *Journal of Fluid Mechanics* 924, A6. DOI: 10.1017/jfm.2021.605.

Pope, S.B. (2000). *Turbulent Flows*. Cambridge University Press, pp. 3–9, 34–83, 96–178, 182–264. ISBN: 9780521598866. URL: https://books.google.no/books?id=HZsTw9SMx-0C.

Qiao, Fangli et al. (2016). 'Wave–turbulence interaction-induced vertical mixing and its effects in ocean and climate models'. In: *Philosophical Transactions of the Royal Society A: Mathematical, Physical and Engineering Sciences* 374.2065, p. 20150201. DOI: 10.1098/rsta.2015.0201. eprint: https://royalsocietypublishing.org/doi/pdf/10.1098/rsta.2015.0201. URL: https://royalsocietypublishing.org/doi/abs/10.1098/rsta.2015.0201.

Rashidi, M., G. Hetsroni and Sanjoy Banerjee (Dec. 1992). 'Wave–turbulence interaction in free-surface channel flows'. In: *Physics of Fluids A: Fluid Dynamics* 4.12, pp. 2727–2738. ISSN: 0899-8213. DOI: 10.1063/1.858331. eprint: https://pubs.aip.org/aip/pof/article-pdf/4/12/2727/12442769/2727_1_online.pdf. URL: https://doi.org/10.1063/1.858331.

Rato, R.T., M.D. Ortigueira and A.G. Batista (2008). 'On the HHT, its problems, and some solutions'. In: *Mechanical Systems and Signal Processing* 22.6. Special Issue: Mechatronics, pp. 1374–1394. ISSN: 0888-3270. DOI: https://doi.org/10.1016/j.ymssp.2007.11.028. URL: https://www.sciencedirect.com/science/article/pii/S0888327007002701.

Reynolds, O (1883). 'XXIX. An experimental investigation of the circumstances which determine whether the motion of water shall be direct or sinuous, and of the law of resistance in parallel channels'. In: *Philosophical Transactions of the Royal Society of London* 174, pp. 935–982. DOI: 10.1098/rstl.1883.0029. eprint: https://royalsocietypublishing.org/doi/pdf/10.1098/rstl.1883.0029. URL: https://royalsocietypublishing.org/doi/abs/10.1098/rstl.1883.0029.

— (1894). 'On the dynamical theory of in-compressible viscous fluids and the determination of the criterion. Phil. Trans. Roy. Soc.' In: *(A), 186, 123-164.*

Richardson, Lewis Fry (1922). *Weather prediction by numerical process.* University Press.

Rockel, Stanislav et al. (2017). 'Dynamic wake development of a floating wind turbine in free pitch motion subjected to turbulent inflow generated with an active grid'. In: *Renewable Energy* 112, pp. 1–16. ISSN: 0960-1481. DOI: https://doi.org/10.1016/j.renene.2017.05.016. URL: https://www.sciencedirect.com/science/article/pii/S0960148117304019.

Rumble, John R, David R Lide and Thomas J Bruno (2018). *CRC handbook of chemistry and physics : a ready-reference book of chemical and physical data.* 99th edition. Boca Raton: CRC Press.

Savelsberg, Ralph and Willem van de Water (2009). 'Experiments on free-surface turbulence'. In: *Journal of Fluid Mechanics* 619, pp. 95–125. DOI: 10.1017/S0022112008004369.

Savelyev, Ivan B., Eric Maxeiner and Dmitry Chalikov (2012). 'Turbulence production by nonbreaking waves: Laboratory and numerical simulations'. In: *Journal of Geophysical Research: Oceans* 117.C11. DOI: https://doi.org/10.1029/2012JC007928. eprint: https://agupubs.onlinelibrary.wiley.com/doi/pdf/10.1029/2012JC007928. URL: https://agupubs.onlinelibrary.wiley.com/doi/abs/10.1029/2012JC007928.

Schlichting, Hermann and Klaus Gersten (2017). *Boundary-Layer Theory, Ninth Edition.* Berlin/Heidelberg, Germany: Springer-Verlag.

Shen, Lian et al. (1999). 'The surface layer for free-surface turbulent flows'. In: *Journal of Fluid Mechanics* 386, pp. 167–212. DOI: 10.1017/S0022112099004590.

Smeltzer, Benjamin K. et al. (2023). 'Experimental study of the mutual interactions between waves and tailored turbulence'. In: *Journal of Fluid Mechanics* 962, R1. DOI: 10.1017/jfm.2023.280.

Taylor, G. I. (1938). 'The Spectrum of Turbulence'. In: *Proceedings of the Royal Society of London. Series A - Mathematical and Physical Sciences* 164.919, pp. 476–490. DOI: 10.1098/rspa.1938.0032. eprint: https://royalsocietypublishing.org/doi/pdf/10.1098/rspa.1938.0032. URL: https://royalsocietypublishing.org/doi/abs/10.1098/rspa.1938.0032.

Thais, L. and J. Magnaudet (1996). 'Turbulent structure beneath surface gravity waves sheared by the wind'. In: *Journal of Fluid Mechanics* 328, pp. 313–344. DOI: 10.1017/S0022112096008749.

Trush, A., S. Pospísil and H. Kozmar (2020). 'Comparison of turbulence integral length scale determination methods'. In: *WIT Transactions on Engineering Sciences* 128, p. 11. DOI: 10.2495/AFM200111.

Tsai, Wu-ting, Shi-ming Chen and Guan-hung Lu (2015). 'Numerical Evidence of Turbulence Generated by Nonbreaking Surface Waves'. In: *Journal of Physical Oceanography* 45.1, pp. 174–180. DOI: https://doi.org/10.1175/JPO-D-14-0121.1. URL: https://journals.ametsoc.org/view/journals/phoc/45/1/jpo-d-14-0121.1.xml.

Walker, D. T., C.-Y. Chen and W. W. Willmarth (1995). 'Turbulent structure in free-surface jet flows'. In: *Journal of Fluid Mechanics* 291, pp. 223–261. DOI: 10.1017/S0022112095002680.

Walker, D. T., R. I. Leighton and L. O. Garza-Rios (1996). 'Shear-free turbulence near a flat free surface'. In: *Journal of Fluid Mechanics* 320, pp. 19–51. DOI: 10.1017/S0022112096007446.

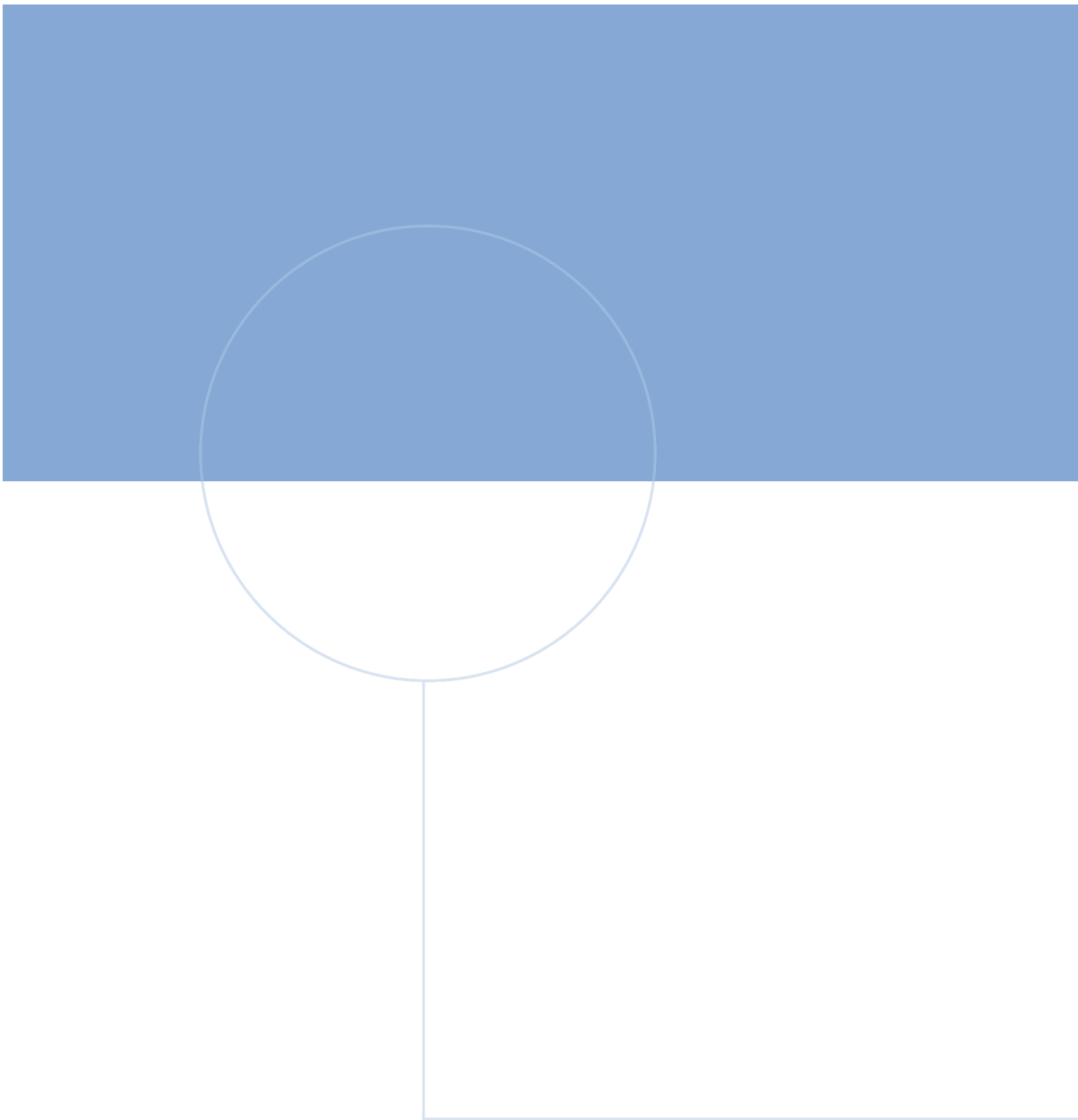

NTNU

Norwegian University of
Science and Technology